UNIVERSITÀ DEGLI STUDI DI PADOVA

UNIVERSITÀ DI PADOVA FACOLTÀ DI INGEGNERIA

DIPARTIMENTO DI INGEGNERIA DELL'INFORMAZIONE

SCUOLA DI DOTTORATO IN INGEGNERIA DELL'INFORMAZIONE

CURRICULUM IN SCIENZA E TECNOLOGIA DELL'INFORMAZIONE

XXIX Ciclo

Novel Network Paradigms: Microfluidic and M2M Communications

Dottorando

ANDREA BIRAL

Supervisore:

Ch.mo Prof. Andrea Zanella

Direttore della Scuola:

Ch.mo Prof. Matteo Bertocco

Anno Accademico 2016/2017

Abstract

The present thesis focuses on two appealing paradigms that are expected to characterize the next generation of communication systems: microfluidic networking and Machine to Machine (M2M) Communications.

Concerning the former topic, we show how it is possible to introduce switching and routing mechanism in microfluidic systems. We define some simple mathematical models that capture the macroscopic behavior of droplets in microfluidic networks. Then, we use them to implement a simulator that is able to reproduce the motion and predict the path of droplets in a generic microfluidic system. We validate the simulator and apply it to design a network with bus topology. Finally, we prove the feasibility of attaining molecular communication in this domain by describing a simple protocol that exploits droplets length/interdistance modulation to send information.

The research activity on M2M, instead, is aimed at the investigation of two critical issues that are expected to affect Machine-Type Communication (MTC), i.e. energy efficiency and massive access.

Regarding energy efficiency, we address the problem of delivering a fixed data payload over a Rayleigh fading wireless channel with the purpose of minimizing the average total energy cost, given by the sum of the transmit energy and an overhead circuit energy, to complete it. This scenario is well suited for uplink cellular MTC in future 5G Internet of Things (IoT) use cases, where the focus is more on device energy efficiency than on throughput. We describe the optimal transmission policies to be used under various coordinated access scenarios with different levels of channel state information and transmitter/receiver capabilities, and show the corresponding theoretical bounds.

In the last part of the work, we study the asymptotic performance of uncoordinated access schemes with Multi Packet Reception (MPR) and Successive Interference Cancellation (SIC) techniques for contention resolution at the receiver. The corresponding results in terms of throughput in a massive access M2M scenario are finally evaluated and discussed.

Contents

Figure list

Table list

Preface

The three years research activity of my Ph.D. has mainly developed over the following two topics: microfluidic networking and Machine to Machine (M2M) Communications. Although these two fields of research are very different and, thus, have been studied separately, a common thread that binds them is in the novelty that they bring in the world of telecommunications. Indeed, these innovative concepts attracted the attention of many ICT researchers and became hot topics in the last few years. A brief description of the original contribution of this work, along with the reference to the articles where it has appeared, is presented below.

Microfluidic networking is a branch of molecular communication that studies the flow of droplets inside channels of sub-millimeter dimension. Its purpose is to investigate the feasibility of introducing information theory and telecommunication concepts in this domain. This objective requires a thorough revision of the traditional networking concepts both at the physical and MAC layer. Moreover, a deep knowledge of microfluidic flow dynamics and its propagation characteristics is needed. Aware of this prerequisite, we conduct a preliminary study on the state of the art and, building upon that, we derive easy-to-handle mathematical models that describe, at a macroscopic level, droplet formation and routing [1–3]. Then, we apply such concepts to develop a simulator that is capable of reproducing and predicting the flow of droplets inside a generic microfluidic chip [4, 5]. As a proof of concept, we apply it to design and analyze a microfluidic network with bus topology. Finally, we also propose a practical scheme to send information by means of droplets in a microfluidic system [6]. This works have been partially

funded by the University of Padova through the PRAT2012 project "Microfluidic Networking (MiNET): introducing networking technologies in microfluidic systems." Moreover, the fabrication of the microfluidic circuits and realization of the experiments were made possible thanks to the precious collaboration with the Physics department of the University of Padova, which kindly made its labs, human resources and instruments available for the cause. In this regard, our most sincere thanks go to Prof. Giampaolo Mistura and Ph.D. Students Enrico Chiarello and Paolo Sartori.

Concerning M2M Communications, we focused on two critical issues that are expected to affect Machine Type Communication (MTC): energy efficiency and massive access support [7].

The research activity on energy efficient M2M Communications consisted in the study of the optimal allocation strategies to be used by Machine Type Devices (MTDs) with latency constraints in order to minimize the average total energy cost for packet upload. Such problem is solved for various scenarios that differ both for the accuracy on the Channel Information State (CSI) available and the capabilities at the transmitter/receiver [8, 9]. This work is the result of the collaboration with Alcatel-Lucent Bell Labs, Murray Hill (NJ), USA, where I spent my study period abroad under the supervision of Howard Huang, Head of the Wireless Technologies for the Internet of Things group, who I sincerely thank for making this experience possible and for the helpful discussions and support.

Finally, the problem of massive access in M2M Communications is addressed by studying the limiting performance of uncoordinated access scheme with Multi Packet Reception (MPR) and Successive Interference Cancellation (SIC) capabilities at the receiver [10]. In particular, we find an approximate model to estimate the maximum throughput of such a wireless system and derived the corresponding asymptotic performance.

MICROFLUIDIC NETWORKING

1 Introduction

Microfluidics is the science that studies the flow of fluids inside channels of sub-millimeter dimension [11]. Specifically, this work focuses on droplet-based microfluidic systems, where droplets of a specific bio-chemical reagent (called *dispersed phase*) are dispersed in another immiscible fluid (named *continuous phase*) that acts as droplet carrier.

This area of research has emerged strongly in the past few years thanks to its peculiar features and multidisciplinary nature. Indeed, when constrained in micro-scale channels, fluids exhibit specific behaviors that are unobserved at standard-scale. For instance, fluids that are normally mixable may flow in parallel streams, without mixing [12]. These properties are at the basis of a number of applications, ranging from inkjet printer-heads to optics [13, 14]. However, the most promising utilization of microfluidic technology is in the field of chemical and biological analysis [15, 16], for which it offers considerable advantages compared to traditional standard-scale procedures. Given the reduced dimensions in play, in fact, it is possible to process very small quantities of samples with higher sensitivity and less waste of energy and material.

Nevertheless, nowadays devices designed for the analysis in the microfluidic domain, which we will name microfluidic machines (MMs), are mainly stand-alone, special purpose devices. In order to overcome this limitation, there has been a great effort by the scientific community to introduce networking capabilities in this context. Accordingly, it would be possible to interconnect different MMs and create a sort of miniaturized fully-equipped laboratory where droplets can undergo specific transformations and reactions in cascade [17–20]. Such a

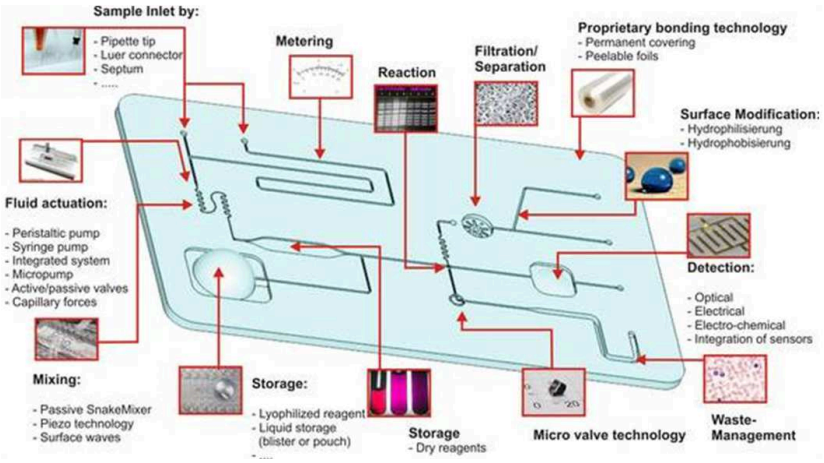

Figure 1.1: Lab-on-a-Chip.

system (cf Fig. 1.1)[1] can be found in literature under the name of Lab-on-a-Chip (LoC).

Two different approaches have been proposed for the routing and control of droplets inside LoCs. The surface-based approaches allows to arbitrarily move droplets on a planar surface by electrowetting-on-dielectric [22, 23] or by acoustic waves [24]. This offers high flexibility because the path of the droplets is freely programmable. However, surface-based approaches suffer from the evaporation of liquids, the fast degradation of the surface coatings, the lack of biocompatibility, and the complex and costly fabrication process [25]. In channel-based approaches, instead, droplets flow in closed microchannels, triggered by some external force (e.g., syringe pump) at the chip boundary, and are passively routed through the network by purely hydrodynamic forces that are mainly controlled by the channel geometry. This solves the issues of surface-based approaches as it allows for the incubation and storage of liquid samples over a long period of time and avoids evaporation and unwanted reactions [25].

Motivated by these considerations, we studied possible solutions to introduce networking principles and enable molecular communication into purely hydrodynamic microfluidic systems. The specificities of microfluidics, however, require a deep knowledge of the physical governing rules of such systems and a thorough revision of the traditional networking approaches, opening the way to a plethora of novel research challenges. To this end, we start in the remainder of

[1]The picture was taken from [21].

this chapter by introducing the fundamentals of droplet-based microfluidics such that the reader can familiarize with the concepts that will be recalled and exploited throughout the entire work. Then, in Ch. 2 we illustrate how to route droplets inside microfluidic systems. Ch. 3 will be dedicated to the description of a simulator that we implemented and is capable of reproducing the macroscopic dynamics of generic microfluidic networks and predict the path followed by droplets inside them. This tool will be exploited in Ch. 4 to analyze a use-case of a microfluidic network with bus topology. In Ch. 5 we will show a proper way to transmit information in a mirofluidic device and, finally, in Ch. 6 we will draw our concluding remarks.

1.1 Fundamentals of microfluidics

For self consistency, in this section we recall the mathematical relations that model the basic microfluidic features and components.

1.1.1 Droplet generation

In the study of a droplet-based microfluidic network, the first aspect to be analyzed is the method of generating and introducing droplets in the system. Not only should these devices produce a regular and stable monodisperse droplet stream, they also need to be flexible enough to easily provide droplets of prescribed volume at prescribed rates. To this end, three main approaches have emerged so far in literature [26], based on different physical mechanisms:

- breakup in co-flowing streams;
- breakup in elongational strained flows (flow focusing devices);
- breakup in cross-flowing streams (T-junction).

We focus only on the last one, which is the most appropriate solution in our case since it is well suited for planar geometries and has clear-cut scaling laws for its physical behavior.

Fig. 1.2 illustrates the geometry of such a T-junction droplet generator. Very simply, it consists of two channels merged at right angle. The main channel carries the continuous (or carrier) fluid and the orthogonal channel supplies the fluid

that will be dispersed in droplets. The channels have rectangular cross sections and the following three geometrical parameters define completely the size and shape of the T-junction: the width w_c of the main channel, the width w_d of the channel supplying the dispersed fluid, and the height h of the channels. In this regard, if not otherwise specified, we focus on planar geometries, with identical rectangular cross-section for every channel, in which the width is slightly greater than the height, i.e. $w_d = w_c = w > h$. Liquid flows are commonly controlled via independent syringe pumps imposing the inlet volumetric flow rates Q_c and Q_d for the continuous and dispersed phase respectively.

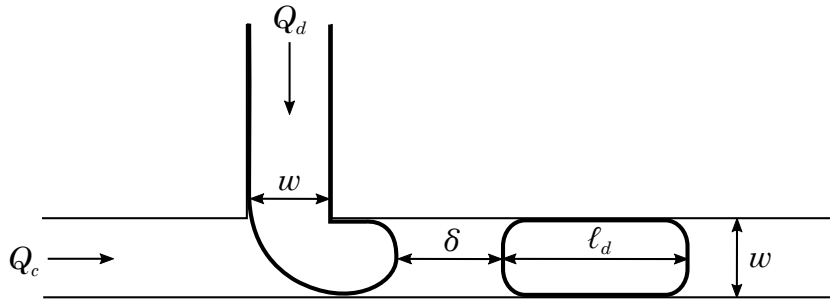

Figure 1.2: Example of droplet generation in a T-junction (top view).

The process of droplet formation begins as soon as the dispersed phase starts penetrating into the main channel. Here, three main forces act on the emerging interface and influence droplet breakup: the surface (or interfacial) tension force (F_σ), which has a stabilizing effect, and the viscous shear-stress force (F_τ) and squeezing force (F_S),[2] both of which have a destabilizing effect and, eventually, lead to the breakup of droplets from the dispersed liquid.

As stated by several studies [27–29], the balance of these forces causes two principal regimes of breakup:

- *squeezing regime*, characterized by the stable formation of uniform and evenly spaced droplets;
- *dripping regime*, where the balance of the forces is much more unstable and short droplets of different size are generated before they can block the main channel.

[2]This force arises from the increased resistance to flow of the continuous fluid around the tip of droplet that is being formed.

Importantly, the transition between them is governed by the Capillary number (Ca), which is a dimensionless parameter that describes the relative magnitude of the viscous shear stress compared to the interfacial tension. A simple definition for Ca in microfluidics is given in terms of the average velocity u_c of the continuous phase, the dynamic viscosity μ_c of the continuous phase and the interfacial tension coefficient σ [30]

$$Ca = \frac{\mu_c u_c}{\sigma} = \frac{\mu_c Q_c}{\sigma w h}. \tag{1.1}$$

In particular, for low values of the Capillary number($Ca \leq Ca^*$), the breakup dynamics in the T-junction are dominated by the squeezing force across the forming droplet and, thus, the system operates under the squeezing regime. In the opposite case ($Ca > Ca^*$), the shear stress starts playing an important role and the droplet generation behaves according to the dripping regime. As reported in [28] and confirmed in our numerical simulations, the threshold that discriminates between the two regimes is given by $Ca^* \approx 10^{-2}$.

Since the squeezing regime shows the best flexibility and control over the shape of generated droplets, it is desirable to work under the condition $Ca \leq Ca^*$. This limit, in turn, sets the following upper bound to the continuous phase speed

$$u_c \leq \frac{\sigma}{\mu_c} Ca^* \,. \tag{1.2}$$

In the reminder we always assume that (1.2) is satisfied. The corresponding droplet's generation dynamics are thoroughly analyzed below.

Squeezing regime

The typical process of droplets formation via squeezing regime is visually depicted in the simulation of Fig. 1.3, obtained with OpenFOAM software. The main geometric and physical parameters used are: $h = 50\,\mu m, w = 150\,\mu m, Q_c = 3.75\,nL/s, Q_d = 1.875\,nL/s$. Keeping in mind the previous analysis and observations, the droplet generation mechanism can be briefly described as follows: the two immiscible fluids form an interface at the junction between the dispersed inlet channel and the main channel. The stream of the discontinuous phase starts flowing into the main channel and a droplet begins to grow under the effect of the viscous shear-stress force (Fig. 1.3(a)). The latter, however, is not sufficient to distort the interface significantly because in this regime $Ca < Ca^*$ and the interfacial tension dominates the shear stress. Consequently, the emerging droplet

manages to fill the junction and restricts the available area through which continuous fluid can flow, leading to an increased pressure directly upstream of the junction (Fig. 1.3(b)). When the corresponding squeezing force overcomes the interfacial tension force, the neck of the emerging droplet squeezes (Fig. 1.3(c)), favoring its breakup. Finally, the disconnected liquid plug flows downstream of the main channel, while the tip of the dispersed phase retracts to the end of the inlet and the process repeats itself anew (Fig. 1.3(d)). The intrinsic high reproducibility shown by this mechanism is fundamental for the stable production of uniform droplets with identical length and shape (Fig. 1.3(e)) over a wide range of flow rates.

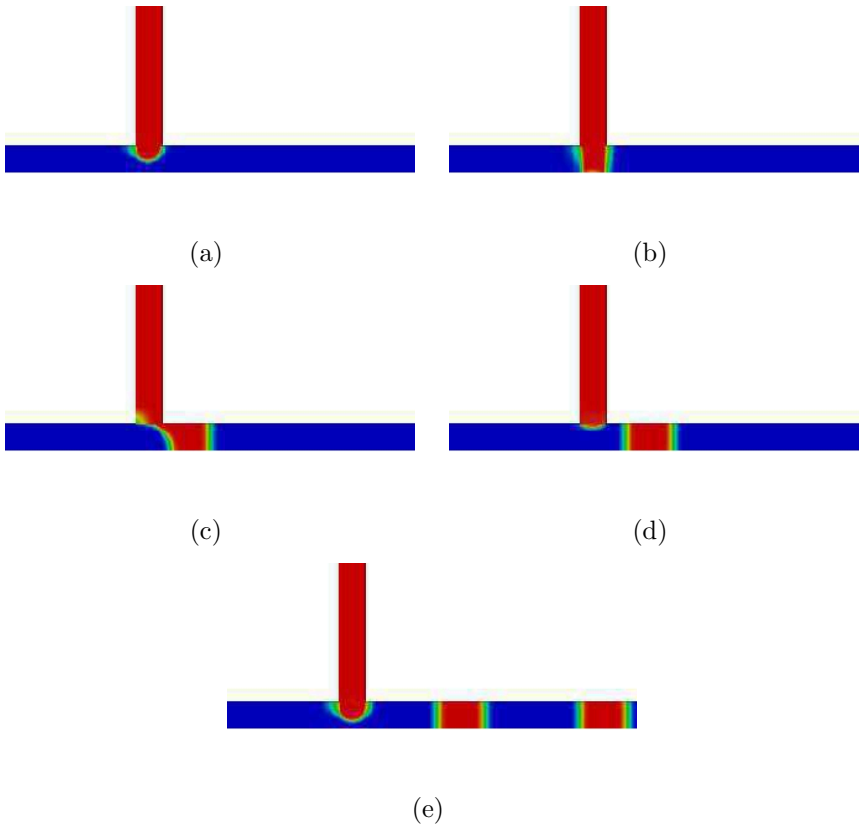

Figure 1.3: Typical process of droplet formation under squeezing regime.

Droplets length

Garstecki *et al.* [28] obtained a simple formula for the length ℓ_d of the droplets resulting from breakup at the T-junction in the squeezing regime, i.e.,

$$\ell_d = w(1 + \xi \frac{Q_d}{Qc}) \; ; \tag{1.3}$$

where w is the width of the main channel, Q_d is the flow of the dispersed phase, Q_c is the flow of the carrier fluid and ξ is a dimensionless parameter that depends on the geometric and physical parameters of the system. (1.3) can be intuitively explained by considering that the detachment begins when the emerging discontinuous thread fills completely the main channel, i.e., when the squeezing force is stronger. At this moment, the length of the droplet is approximately equal to the width of the channel w, and the thickness of the neck in the junction starts decreasing at a rate that depends on the speed of the continuous flow u_c. The flow of the carrier fluid ($Q_c = u_c hw$), hence, determines the squeezing time necessary for the neck of the droplets to break. In fact, for a given dispersed phase flow, the greater the continuous flow the lower the squeezing time and thus the length of the resulting droplets. On the other hand, there is a direct proportionality between droplet length and dispersed phase flow ($\ell_d \propto Q_d$) because Q_d determines how much dispersed fluid forms a droplet before breakup.

Interdistance between droplets

Another physical parameter to be considered, is the spacing $\delta\,[m]$ between droplets generated under the squeezing regime. Its formula can be deduced from the application of the mass conservation law.

Let us consider a sufficiently long time τ and the related distance $x = u'_d\tau$ covered by droplets along the main channel, being u'_d the speed of the dispersed fluid in the main channel. The number of droplets generated in the time interval τ is given by:

$$n_d(\tau) = \frac{x}{\ell_d + \delta} = \frac{u'_d\tau}{\ell_d + \delta}, \tag{1.4}$$

where ℓ_d is the length of each single droplet, and δ is the interdistance between droplets.

According to the mass conservation law, the volume of dispersed liquid injected by the discontinuous phase inlet throughout the time interval τ must correspond to the volume of dispersed fluid along x in the main channel, i.e.,

$$u_d wh\tau = \frac{V_d u'_d\tau}{\ell_d + \delta}\ ; \tag{1.5}$$

where V_d is the volume of the droplets. Accordingly:

$$\delta = \frac{V_d u'_d\tau}{u_d wh\tau} - \ell_d; \tag{1.6}$$

This general expression can be further specialized under some simplifying assumptions. First of all, we can make the hypothesis, confirmed by our simulations, that dispersed and continuous phase flow at the same velocity, i.e., $u'_d = u'_c = u$, though it is not always true [31]. Accordingly, by applying flows conservation and considering channels with identical cross section, we get:

$$Q = Q_d + Q_c \Rightarrow u = u_d + u_c. \tag{1.7}$$

Substituting (1.7) in (1.5), it results:

$$u_d(\ell_d + \delta) = V_d(u_d + u_c). \tag{1.8}$$

Now, concerning the volume of the droplets, we notice that they are not exact parallelograms but are curved at the edges. Therefore, if we approximate the tips as hemispheres with radius $w/2$ we obtain:

$$V_d = wh(\ell_d - w) + \frac{1}{6}\pi w^3. \tag{1.9}$$

Putting all the pieces together, we obtain the following expression of the interdistance between droplets generated in a T-junction in the squeezing regime:

$$\begin{aligned} \delta &= \frac{V_d}{Q_d wh}(Q_d + Qc) - \ell_d \\ &= \ell_d \frac{Q_c}{Q_d} + \frac{(1/6\pi w^3 - w^2 h)}{Q_d wh}(Q_d + Q_c). \end{aligned} \tag{1.10}$$

Lingering on (1.10), it can be noted that droplets length and interdistance are correlated since δ depends on ℓ_d. Consequently, once fixed the geometry of the system and the physical parameters of the liquids, droplets with a specific length will have a corresponding precise interdistance between them.

1.1.2 Fluidic resistance

According to Hagen-Poiseuille law, the average flow rate Q_c in a microfluidic channel of length L is proportional to the pressure gradient ΔP across it according to the equation

$$\Delta P = R(\mu_c, L)\, Q_c\,, \tag{1.11}$$

where the parameter $R(\mu_c, L)$ is called fluidic resistance. In general, $R(\mu, L)$ can be expressed as [32]

$$R(\mu, L) = \frac{a\mu L}{wh^3}\,, \tag{1.12}$$

where a is a dimensionless parameter that depends on the channel geometry and, for rectangular sections, is equal to

$$a = 12\left[1 - \frac{192h}{\pi^5 w}\tanh\left(\frac{\pi w}{2h}\right)\right]^{-1}. \tag{1.13}$$

Furthermore, when a droplet with dynamic viscosity μ_d is injected into a duct, the friction generated with the carrier fluid and the forces produced by the inhomogeneity between the dynamic viscosities of the continuous and dispersed phases change the hydraulic resistance of the channel [33–35]. Mathematically, the variation of resistance produced by a droplet of length ℓ_d in a channel of length L can be approximated as [2]

$$\begin{aligned}\rho(\ell_d) &= R(\mu_c, L-\ell_d) + R(\mu_d, \ell_d) - R(\mu_c, L)\\ &= (\mu_d - \mu_c)\frac{\ell_d a}{wh^3},\end{aligned} \tag{1.14}$$

such that the overall fluidic resistance of the channel crossed by the droplet is $R(\mu_c, L) + \rho(\ell_d)$.[3] Note that, these relations are (approximately) verified in practice only when the droplet is large enough to entirely fill the channel section, with an extremely thin stream of continuous phase between the droplet and the channel surfaces. In this case, the speed of the droplet when crossing a channel is basically the same as that of the continuous phase in that channel, i.e.,

$$u_d = u_c = \frac{Q_c}{wh} = \frac{\Delta P}{wh(R(\mu_c, L) + \rho(\ell_d))}. \tag{1.15}$$

Therefore, the resistance in the different parts of a microfluidic network may change over time, depending on the path followed by the droplets, and on their size. Moreover, the speed of droplets depends on the volumetric flow rate of the continuous phase in the branches that, in turn, is affected the hydraulic resistance of the channels and on the droplet positions. These principles are at the basis of the design of purely hydrodynamic switching elements, as described in Ch. 2.

[3] According to (1.14), a droplet increases the hydraulic resistance of a channel only if $\lambda = \frac{\mu_d}{\mu_c} > 1$. However, some experiments have revealed an increment in resistance also for $\lambda < 1$. The reason for this discrepancy is that (1.14) does not account for a number of secondary forces that act on the narrow region between the droplet boundaries and the channel walls, which are generally negligible for $\lambda > 1$. Further comments on this regard can be found in [2].

1.1.3 Microfluidic-electric duality

In [36,37] the authors have advanced an interesting parallelism between continuous-flows (layered) microfluidic systems and electric systems. In their work they showed how the molecules of fluid in a hydraulic circuit behave similar to the electrons in an electric circuit. This section shows the main analogies between these two domains as they will be useful later. First of all, the pressure difference ΔP, volumetric flow rate Q, and hydraulic resistance R of a microfluidic channel can be associated to the voltage drop ΔV, current intensity I, and Ohmic resistance R of an electric line, respectively. Therefore, Ohm's and Kirchhoff's current and voltage laws

$$\Delta V = RI\,, \quad \sum_{m=1}^{M} I_m = 0\,, \quad \sum_{k=1}^{K} V_k = 0\,, \tag{1.16}$$

correspond to the Hagen-Poiseuille law, and the flow and energy conservation laws in microfluidic circuits

$$\Delta P = RQ\,, \quad \sum_{m=1}^{M} Q_m = 0\,, \quad \sum_{k=1}^{K} \Delta P_k = 0\,, \tag{1.17}$$

where M is the number of branches departing from a junction, K is the number of contiguous channel segments in any closed loop of the circuit, and R is given by (1.12) for rectangular microfluidic channels. Consequently, the equivalent hydraulic resistance of a series of microfluidic channels is the sum of their resistance, while the conductance of the parallel of microfluidic channels is the sum of their conductance.

We can also extended the duality between microfluidic and electric domains to the sources of the corresponding fields. In particular, an ideal current generator which provides constant electric current through a line, irrespective of its resistance, is equivalent to an ideal syringe pump that maintains a constant volumetric flow rate through a channel. On the other hand, an ideal voltage generator, which maintains a certain voltage across a line, is similar to a peristaltic pump that maintains a constant pressure difference across a channel.

Finally, although the microfluidic-electric analogy was originally proposed for layered microfluidic systems, with some shrewdness it can as well be applied to droplet-based microfluidic systems. Indeed, each droplet can be represented as an additional resistor, with resistance given by (1.14), connected in series to

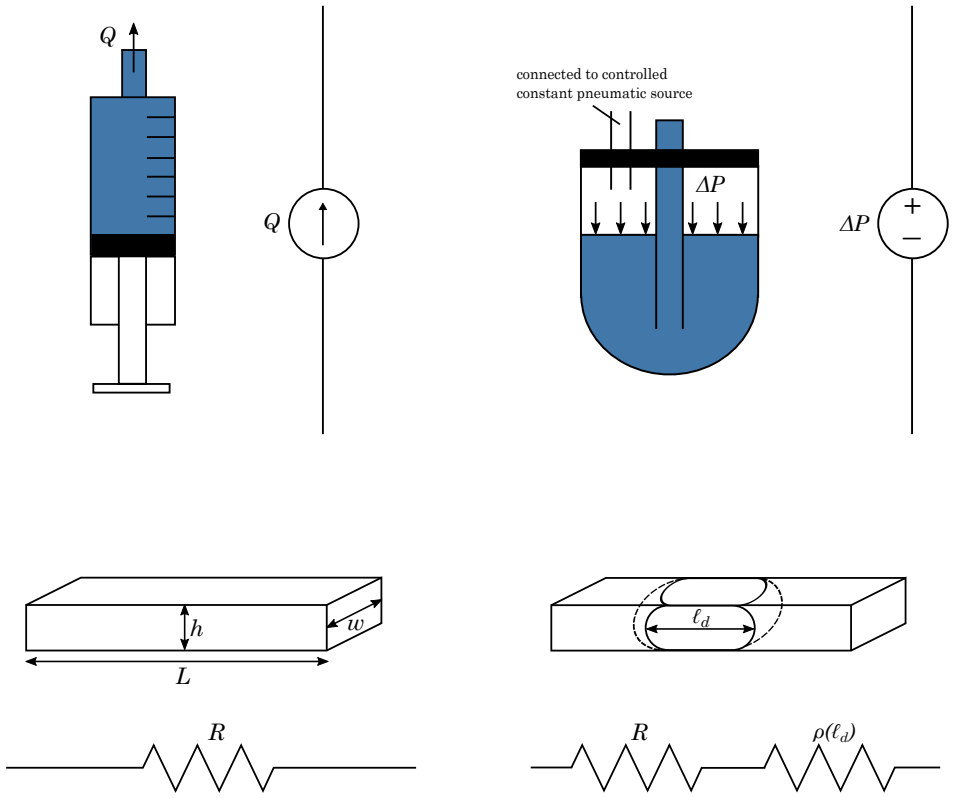

Figure 1.4: Microfluidic-electrical duality: constant flow rate & current generator (top/left), constant pressure drop & voltage generator (top/right); microfluidic channel without droplets & electrical resistor (bottom/left); microfluidic channel with droplet & series of resistors (bottom/right).

the original resistance associated to the channel that contains the droplet. A pictorial representation of the basic components of a microfluidic system and their electrical counterpart is shown in Fig. 1.4.

This map can be used to derive the flow dynamics in complex microfluidic networks based on conventional electric circuit theory.

2

Microfluidic switching mechanism

Switching elements are part and parcel of any network. In the microfluidic domain, they can be realized by means of junctions, which simply consist of channels that fork into two (or more) branches, usually with T or Y shape.

The pattern followed by droplets across a junction may either be regular or chaotic, depending on a number of factors. Furthermore, droplets may collide, coalesce or split when crossing a junction, as observed in several studies [33–35,38]. Focusing on T-junctions, a droplet can either split into the two outgoing branches (*breakup regime*) or stay compact and flow along the branch with minimum instantaneous fluidic resistance (*non-breakup regime*).In this work we are only interested on systems that preserve the droplet integrity across junctions, though the study of droplet transformations (e.g., splitting, merging, and so on) is an interesting research challenge that is left for future work.

We hence focus on the non-breakup regime that, according to the mathematical model proposed in [35], requires

$$\ell_d < \chi w Ca^{-0.21}\,, \tag{2.1}$$

where χ is a dimensionless parameter that decreases as the viscosity ratio between dispersed and continuous phase $\lambda = \frac{\mu_d}{\mu_c}$, increases [39]. Note that, the non-breakup regime sets an upper limit to the droplet speed

$$u_d < \frac{\sigma}{\mu_c}\left(\frac{\chi w}{\ell_d}\right)^{\frac{1}{0.21}}\,. \tag{2.2}$$

Considering (1.15), the conditions (1.2) and (2.2) yield a limit to the speed of the

continuous phase in any channel of the circuit, which is equal to

$$u^{\max} = \frac{\sigma}{\mu_c} \min \left\{ 10^{-2}, \left(\frac{\chi w}{\ell_d} \right)^{\frac{1}{0.21}} \right\} . \tag{2.3}$$

Under this assumption, a droplet entering a T-junction will not split, but rather proceed along the outlet with smallest instantaneous hydraulic resistance or, equivalently, greatest volumetric flow rate [40, 41]. This property is at the basis of the sorting mechanism that we developed and describe next.

2.1 T-junction switch

Let us consider a simple bifurcation with T-shape, which consists of a channel that branches out into two asymmetric rectangular channels 1 and 2, as depicted in Fig. 2.1 together with its equivalent electric circuit. We assume that all channels have the same cross section with width w and height h. Moreover, channel 2 is shorter than channel 1, i.e. $L_2 < L_1$. Recalling (1.12), this means that channel 2 has lower hydrodynamic resistance than channel 1, i.e. $R_2 < R_1$.

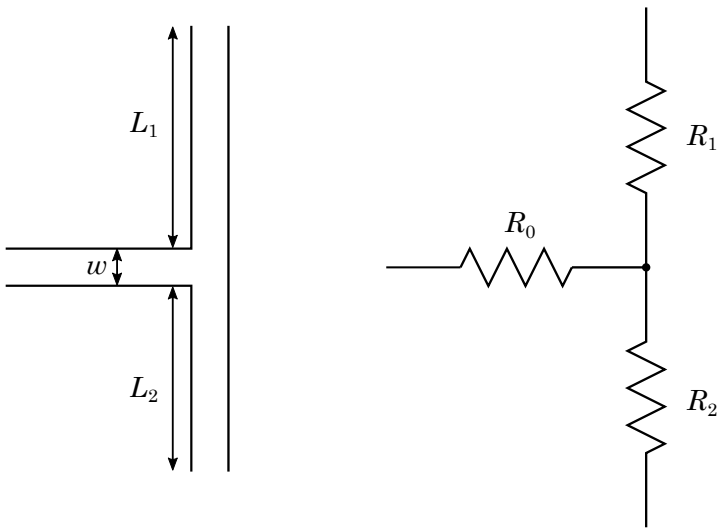

Figure 2.1: Simple T-junction switch.

Now, let us suppose to inject a pair of droplets cf (Fig. 2.2) that we will denote with *header* and *payload*, borrowing the terminology from the ICT field. Since $R_2 < R_1$ the first droplet (header) flows into channel 2. As a consequence, it increases the resistance of channel 2 by $\rho(\ell_H)$, where ℓ_H is the length of the

header and ρ is given by (1.14). Now, if the header is still in channel 2 when the payload arrives at the bifurcation, we distinguish two possible scenarios. If the new resistance of channel 2 is larger than the resistance of channel 1, i.e. $R_2 + \rho(\ell_H) > R_1$, the payload will flow into channel 1. Conversely, if $R_2 + \rho(\ell_H) \leq R_1$, the payload will flow into channel 2. In both cases, this involves an increase of $\rho(\ell_P)$ in the resistance of the channel selected by the payload. Therefore, the sorting of payload droplets at a bifurcation can be encoded in the distance between header and payload and/or in the length of the header droplet.

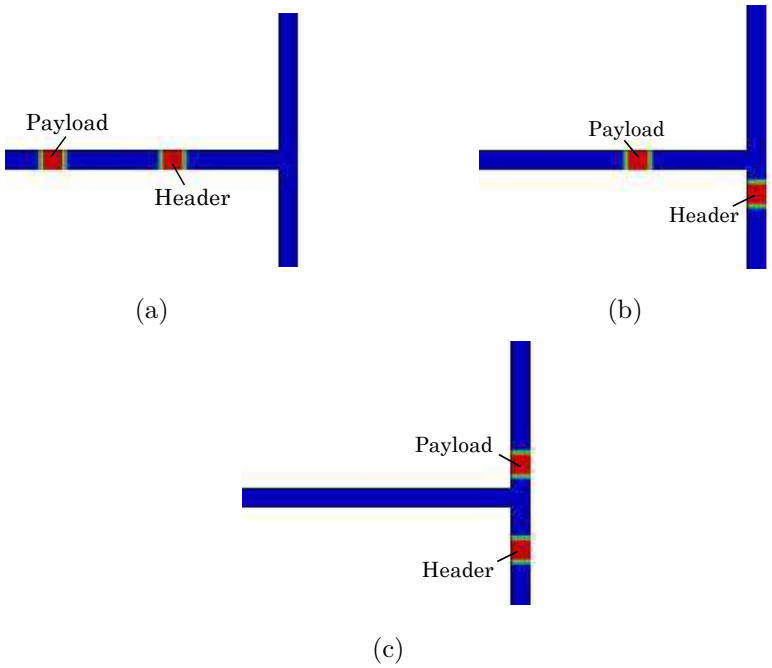

Figure 2.2: OpenFOAM simulation of a T-junction switch. (a)Header and payload approaches the bifurcation. (b)The header flows in the shorter branch, it increases its resistance and (c)deviates the payload to the opposite channel.

Unfortunately, the switching element in Fig. 2.1 is quite sensitive to small imperfections in the fabrication of the junction, noise and fluctuations in the operational parameters of the system. A solution to increase its robustness to such non-idealities and provide stronger control on the droplet behavior was proposed in [42] and described hereafter.

2.2 T-junction switch with bypass channel

The new switching element is sketched in Fig. 2.3, which also reports the equivalent electric circuit. It consists of a T-junction where the input channel bifurcates into two asymmetric channels 1 and 2, whose ends (nodes A and B in the picture) are connected by a *bypass channel*, and terminate in output channels 3 and 4, respectively. By analogy with the previous case, we assume that $L_2 < L_1$, such that $R_2 < R_1$.

The purpose of the bypass channel is to create a very low-resistance connection (R_{byp}) between the branches of the bifurcation. The effect achieved is to decouple the switching at the junction from the rest of the network. To this end, the bypass channel has to satisfy the following conditions.

- Its resistance R_{byp} needs to be extremely low (ideally null). This implies that the voltages (i.e., pressures) at points A and B in Fig. 2.3 are almost identical.

- It must not let the droplets flow inside. To meet this goal, the ends of the bypass channel are obstructed by barriers that block the passage of droplets, while letting the continuous phase flow freely through them.

Below we provide the analysis of the electric circuit in Fig. 2.3, which demonstrates that the switch works as desired when the above-mentioned conditions are satisfied.

As the input flow rate Q_0 splits between Q_1 and $Q_2 = Q_0 - Q_1$, the sign of $Q_1 - Q_2$ determines the path taken by a droplet that enters the switch. In fact, recalling that droplets follow the path with highest flow rate, if $Q_1 - Q_2 > 0$ the incoming droplet will flow into channel 1. On the contrary, if $Q_1 - Q_2 < 0$ the droplet selects channel 2. The expression for $Q_1 - Q_2$ can be obtained by applying Kirchhoff laws

$$\begin{cases} Q_0 = Q_1 + Q_2 \\ Q_1 = Q_3 - Q_{\text{byp}} \\ Q_2 = Q_4 + Q_{\text{byp}} \\ R_1 Q_1 = R_2 Q_2 + R_{\text{byp}} Q_{\text{byp}} \\ R_3 Q_3 = R_4 Q_4 - R_{\text{byp}} Q_{\text{byp}} \end{cases} \tag{2.4}$$

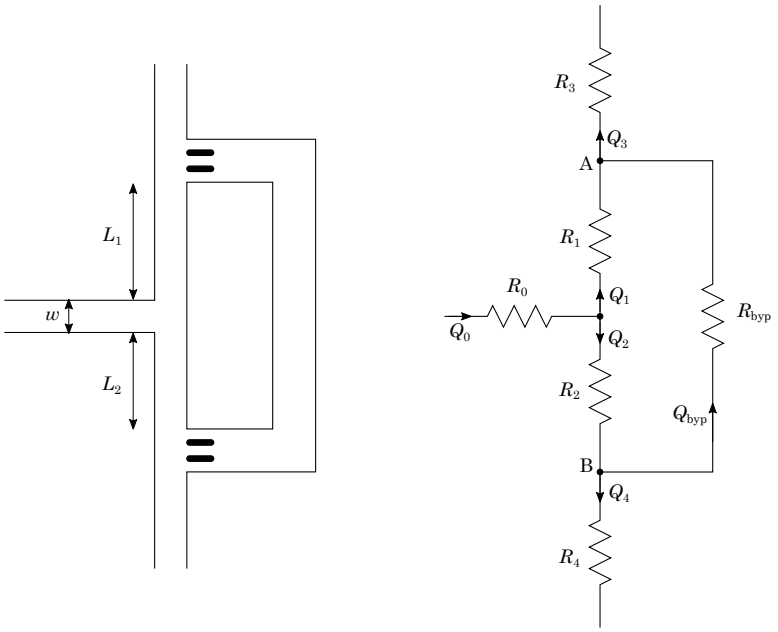

Figure 2.3: T-junction switch with bypass channel.

where Q_i is the current across resistor R_i. Its solution returns

$$\frac{Q_1 - Q_2}{Q_0} = \frac{R_2 - R_1 + \frac{R_{\text{byp}}}{Q_0 R_3 R_4}(R_4 P_A + R_3 P_B)}{R_1 + R_2 + R_{\text{byp}}}, \tag{2.5}$$

where P_B and P_A are the pressures at nodes B and A, respectively. If $R_{\text{byp}} \simeq 0$, (2.5) can be approximated as

$$\frac{Q_1 - Q_2}{Q_0} = \frac{R_2 - R_1}{R_1 + R_2}, \tag{2.6}$$

from which we see that the switching element becomes simultaneously very sensitive to $R_2 - R_1$ and insensitive to R_3 and R_4. This last aspect is particularly welcome since it allows to isolate the switching element from the rest of the system simplifying the design of complex networks as illustrated in Ch. 4. For the sake of simplicity, in the reminder of the work we assume that approximation (2.6) holds. Accordingly, we will consider the bypass channel as an electric short circuit.

Similar to the simple T-junction switch, we can exploit header droplets to sort payloads to the desired arm of the bifurcation. Specifically, let us consider a header and a payload with a distance δ_{HP} arriving at the T-junction of the switch. Since $R_2 < R_1$, the header droplet flows into channel 2. Then, we can distinguish two cases depending on the distance δ_{HP}:

- $\delta_{HP} > L_2 \frac{Q_0}{Q_2}$: This means that the header has already left channel 2 when the payload approaches the T-junction. Thus, as shown in the previous analysis, the header will not affect the path of the payload which will also flow into channel 2.

- $\delta_{HP} < L_2 \frac{Q_0}{Q_2}$: The header droplet is still in channel 2 and increases its hydrodynamic resistance by $\rho(\ell_P)$. Now, if $R_2 + \rho(\ell_P) > R_1$ the payload flows into channel 1, while it takes channel 2 if $R_2 + \rho(\ell_P) < R_1$.

This simple example shows an effective technique to route droplets in a microfluidic network using purely hydrodynamic rules.

However, the inter-dependencies among different components of a droplet-based microfluidic system, together with the time-varying effect of droplets motion throughout the channels, make its temporal analysis a challenging task. To address this problem, we implemented a simulator that is able to reproduce the macroscopic dynamics of a microfluidic system and predict the route of the droplets inside it. The next section is dedicated to its description and validation.

3 Microfluidic simulator

Dedicated simulation packages, such as OpenFOAM and COMSOL, can be used to characterize the behavior of microfluidic circuits. These software packages are designed to solve Computational Fluid Dynamics (CFD) problems based on finite element analysis. Their approach consists in partitioning the microfluidic system in a sufficiently dense volume grid to solve the differential Navier-Stokes equations that govern the interaction of liquids in microfluidics. These methods can be applied to solve a variety of CFD problems, with high degree of details. However, their execution time grows almost linearly with the number of elements in the grid such that the simulation of complex circuits may become prohibitively time consuming.

On the other hand, the microfluidic networking research is currently focused on the macroscopic characterization of droplet-based microfluidic networks, rather than on fine-grained analysis of its evolution. Indeed, since the interest is in controlling the path followed by droplets in complex circuits, we do not need the high accuracy provided by current CDF solvers, but rather a lighter model that captures the most significant interactions among the circuit elements. This makes it possible to correctly predict droplets motion across the network with reduced computational complexity and significant time saving.

Our objective is, hence, to define a mathematical model that cuts a suitable tradeoff between reality abstraction and model complexity. To this end, we exploit the concepts derived in Sec. 1.1. Based on these principles, it is possible represent the microfluidic system as a time-varying electric circuit and apply Kirchhoff laws to find the flow rate and pressure drop in any microfluidic channel of the circuit. The current distribution is then recomputed when the resistance of one or more

branches change, which happens, for example, when a droplet flows into another channel through a junction or exits the circuit. Following this argumentation, we proposed and developed an event-based simulator that reproduces the evolution of a microfluidic network as a discrete-time multidimensional process. Its thorough description and validation is provided in the reminder of this section.

3.1 Microfluidic system modeling

First of all, we represent a generic microfluidic system by means of a graph $G = (V, E)$, where $V = \{v_1, \ldots, v_{N_V}\}$ denotes the set of *vertices* where the different components of the microfluidic network interconnect, while $E = \{e_1, \ldots, e_{N_E}\}$ is the set of *edges* of the graph, each corresponding to an elementary building block described in Sec. 1.1 and Ch. 2, namely flow generator (FG), pressure generator (PG), droplet generator (DG), microfluidic channel (CH), bypass channel (BP), and microfluidic machine (MM). Each edge e_i is described by means of a vector $e_i = [\text{type}_i, v_{i-}, v_{i+}, L_i, p_i]$, where

- $\text{type}_i \in \{\text{FG}, \text{PG}, \text{DG}, \text{CH}, \text{BP}, \text{MM}\}$ denotes the type of microfluidic component associated to the edge;
- $v_{i-}, v_{i+} \in V$ are the endpoints of the edge, with the convention that the flow is oriented from v_{i-} to v_{i+};
- L_i is the length of the microfluidic channel associated to edge i;
- p_i is the value of the parameters vector related to the component type_i; i.e. imposed volumetric flow rate/pressure for FG/PG, imposed flow rate, droplet length and generation time processes for DG, fluidic resistance for CH and BP, and absolute pressure value for MM.

Note that, in this work, we consider MMs as sinks that somehow consume the incoming droplets. As such, they will be simply treated as drain-outlet ports that open to atmospheric pressure P_{atm}. Therefore, in the dual electric circuit, MMs will correspond to earth or floating ground. However, the framework can easily accomodate more complex models of MMs.

3.1.1 System state

Once defined the microfluidic circuit topology G, we need to capture its time evolution that depends on the motion of the droplets in the circuit. We denote by $d(t)$ the number of droplets in the circuit at time t and we associate each droplet $k \in \{1, \dots, d(t)\}$ to a vector

$$\omega_k(t) = [\ell_{d_k}, c_k(t), x_k(t)], \tag{3.1}$$

where ℓ_{d_k} is the k-th droplet length (or, more generally, the droplet volume in case channels have different sections), $c_k(t) \in E$ is the index of the edge that contains the k-th droplet at time t, and $x_k(t) \in [-1, 1]$ is the relative position occupied by the droplet at time t in channel $c_k(t)$, where the endpoints $v_{c_k(t)+}$ and $v_{c_k(t)-}$ correspond to the relative positions $+1$ and -1, respectively.

We then define the *system state* at time t as the set

$$\mathbf{\Omega}(t) = \left\{\omega_1(t), \dots, \omega_{d(t)}(t)\right\}. \tag{3.2}$$

Note that, given the circuit topology G, the set $\mathbf{\Omega}(t)$ completely characterizes the system behavior at time t, since it specifies where to place the additional resistors associated to the droplets and the distance that each droplet needs to cover before reaching a junction, thus making it possible to compute the speed of the droplets and the time to the next step-event.

More specifically, given $\mathbf{\Omega}(t)$ we can find the instantaneous resistance of each link in the electrical circuit associated to the microfluidic system, considering the additional resistance due to the presence of droplets. Formally, the resistance at time t of a channel e_i can be expressed as

$$R_i(t) = p_i + \sum_{k=1}^{d(t)} \rho(\ell_{d_k}) \delta_{c_k(t), e_i}\ ; \quad \forall e_i \in E\ :\ \text{type}_i \in \{\text{CH,BP}\}\,; \tag{3.3}$$

where $\delta_{h,k}$ is the Kronecker's delta, which equals one if $h = k$, and zero otherwise. By applying Kirchhoff laws, we compute the instantaneous currents (i.e., flow rate) $Q_i(t)$ in each channel $e_i \in E$ that, in turn, gives the speed u_i of the continuous phase and of the droplets in each channel,[1] as per (1.15).

[1] We recall that, the flow u_i through edge e_i is conventionally oriented from v_{i-} to v_{i+}, so that the droplets in the edge move towards v_{i+} if $u_i > 0$, and towards v_{i-} if $u_i < 0$.

State update

These quantities are constant as long as $\mathbf{\Omega}$ remains unchanged. The events that determine a variation in $\mathbf{\Omega}$ will be referred to as *step-events* and correspond to the injection of a new droplet into the circuit, the removal of a droplet through a sink node, the transition of a droplet from one channel to another through a junction, or any other discrete event that changes the flow rate in some part of the network. Keeping this in mind, we need to compute the (virtual) time that, with the current speed, each droplet would take to reach the endpoint of the channel that contains it. For the k-th droplet[2], we have

$$\tau_k = L_{c_k(t)} \frac{1 - \text{sign}(u_{c_k(t)}) x_k(t)}{2|u_{c_k(t)}|}\,, \qquad k = 1, \ldots, d(t)\,; \tag{3.4}$$

where $\text{sign}(X) = +1$ if $X \geq 0$, and $\text{sign}(X) = -1$ otherwise. Now, let $\tau_{d(t)+1}$ be the residual time to the next droplet generation event by any droplet-generator edge. The time to the next step-event is then given by

$$\tau = \tau_{k^\circ} = \min \tau_k,\ k = 1, \ldots, d(t) + 1\,, \tag{3.5}$$

where k° is the index of the droplet that triggers the event.

The system state can finally be updated according to the specific event that occurs at time $t + \tau$. It is easy to realize that, for any $k \neq k^\circ$, the state vector (3.1) can be updated as

$$\omega_k(t + \tau) = \omega_k(t) + \left[0, 0, \frac{2u_{c_k(t)}}{L_{c_k(t)}}\tau\right]\,, \quad k \neq k^\circ\,. \tag{3.6}$$

The update of ω_{k° is slightly more involved. We first distinguish between the event of new droplet generation ($k^\circ = d(t) + 1$), and junction crossing ($k^\circ \leq d(t)$). In the first case, the step-event is triggered by the generation of a new droplet, which is placed at one of the endpoints of the generating edge, which we denote by ℓ°. We then update the droplet counter as

$$d(t + \tau) = d(t) + 1\,,$$

and we add the state vector of the new droplet, given by

$$\omega_{k^\circ}(t + \tau) = [\ell_{d_{k^\circ}}, c_{\ell^\circ}, \text{sign}\,(Q_{c_{\ell^\circ}})]\,.$$

[2]For the sake of simplicity, we here consider droplets as dimensionless points.

Instead, if $k^\circ \leq d(t)$, the step-event is triggered by the exit of a droplet from the system or a junction crossing. We hence need to determine which channel is entered next by k°. To this end, we consider the set $\mathcal{E}(v^\circ)$ of all edges with an endpoint at vertex v°, and whose flow goes toward the opposite endpoint, i.e.,

$$\mathcal{E}(v^\circ) = \left\{ e_i \in E \ : \ \text{sign}(-Q_i)\delta_{v_{i+},v^\circ} + \text{sign}(Q_i)\delta_{v_{i-},v^\circ} > 0 \right\} . \tag{3.7}$$

Among them, the channel having the largest absolute volumetric flow rate at time t will then be the next entered by the k° droplet:

$$c_{k^\circ}(t+\tau) = \arg \max_{e_i \in \mathcal{E}(v^\circ)} \{|Q_i(t)|\} . \tag{3.8}$$

If $c_{k^\circ}(t+\tau)$ is a MM, then the droplet is assumed to leave the circuit and the droplet counter is decremented by one, i.e., $d(t+\tau) = d(t) - 1$. Otherwise, the droplet k° is placed in the new channel at position

$$x_{k^\circ}(t+\tau) = \delta_{v_{c_k(t+\tau)+},v^\circ} - \delta_{v_{c_k(t+\tau)-},v^\circ} . \tag{3.9}$$

By repeating iteratively these steps, it is hence possible to study the time evolution of microfluidic network and the route of the droplets across the circuit. Schematically, the simulative algorithm can be depicted as in Fig. 3.1.

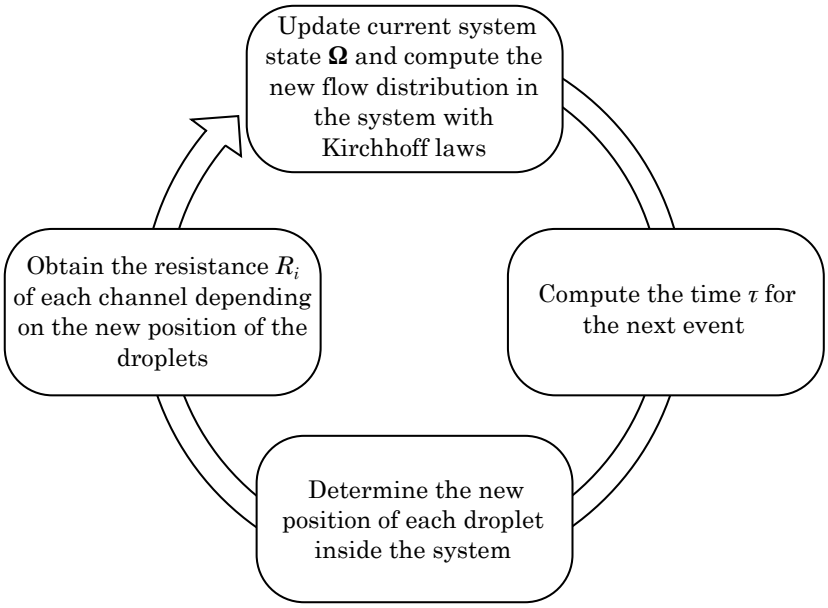

Figure 3.1: Schematic representation of the iterative procedure performed by the simulator.

3.2 Computational complexity of the simulator

Conversely to simulation tools currently used for microfluidic studies, like COMSOL and OpenFOAM (cf App. A.2), which resort to detailed finite element analysis in order to solve continuum hydrodynamic problems, our simulator is based on basic physics laws that govern the macroscopic aspects of microfluidic systems. This leads to a significant reduction in the computational complexity. Of course, this advantage is contrasted by a lower accuracy in the results and the lack of information at the microscopic level (e.g., the shape distortion of the droplets at the entrance of the bifurcations). However, the experimental validation provided in Sec. 3.3 shows that, as long as we are interested in evaluating the path followed by the droplets in a microfluidic circuit, our simulator is quite accurate.

Concerning the computational complexity of the proposed model, we consider the computation cycle represented in Fig. 3.1. We denote by N_L the number of independent loops in the microfluidic/electrical circuit to be simulated, and by d the number of droplets in the circuit in a given time. For each event, the iterative algorithm goes through the following steps:

- First, the algorithm finds the flows in each branch of the circuit by solving a linear system of V equations, given by Kirchhoff current law at each node, plus N_L equations obtained from the Kirchhoff voltage law at each independent loop. This operation has computational complexity $\mathcal{O}(V + N_L)^3$.

- Then, for each droplet in the microfluidic network, the algorithm computes the virtual time taken to generate the next event, using (3.4), and updates the state vectors as for (3.6), (3.8) and (3.9). These operations take constant time for each droplet, so that the execution time of this step scales linearly with the number of droplets d.

Thus, the overall computational complexity of our iterative algorithm is given by $\mathcal{O}((V + N_L)^3 + d)$, which depends on the system topology and the number of droplets in the circuit.

We implemented the proposed simulator in MATLAB®. As expected, it leads to a significant reduction in the running time with respect to traditional CFD solvers. For instance, the simulation of the access control scheme described in the next section, takes less than one second on a ordinary laptop, while the same

simulation using OpenFOAM takes 45 minutes. However, we remark that the proposed model is basically not comparable with the existing tools, having totally different objectives in terms of scope, precision, and generality. To begin with, it has been designed to predict the macroscopic motion of droplets in microfluidic circuits, i.e., considering the droplets as indivisible entities that move compactly along ideal channels. The model simply neglects all fine-grain physical phenomena that may have local effect on the droplet shape and motion, such as deformations or rotation moments, which are instead captured by OpenFOAM and COMSOL. Therefore, our model cannot replicate phenomena such as collisions, or coalescence events. Consequently, it can only be used under very specific conditions, where these microscopic phenomena have negligible impact on the macroscopic motion of the droplet along the channels. On the other hand, within these limits, the proposed model can provide an extremely fast prediction of the motion of the droplets in the circuit.

3.3 Experimental validation

In order to prove the reliability of the model described in Sec. 3.1, we carried out some experiments and compared the results with those given by the simulator.

3.3.1 Sorting in an asymmetric loop

The basic microfluidic system we designed and used for this purpose is illustrated in Fig. 3.2, together with its electrical equivalent circuit: basically, it consists of a T-junction droplet generator, followed by a loop with asymmetric branches. The device, made of polydimethylsiloxane (PDMS), was fabricated using the photolithography technique in our laboratories. Tab. 3.1 collects the geometry parameters of the chip, while Tab. 3.2 contains the physical parameters of the fluids used in the experiments.

A picture of the experimental set-up is shown in Fig. 3.3(a): the microfluidic circuit is connected to two independent syringe pumps[3] for the injection of the continuous/discrete phases, respectively, while the output channel is opened in air. A camera connected to a microscope was used to record real-time videos of the experiments.

[3]We used the PHD 2000 Harvard Apparatus, Holliston MA.

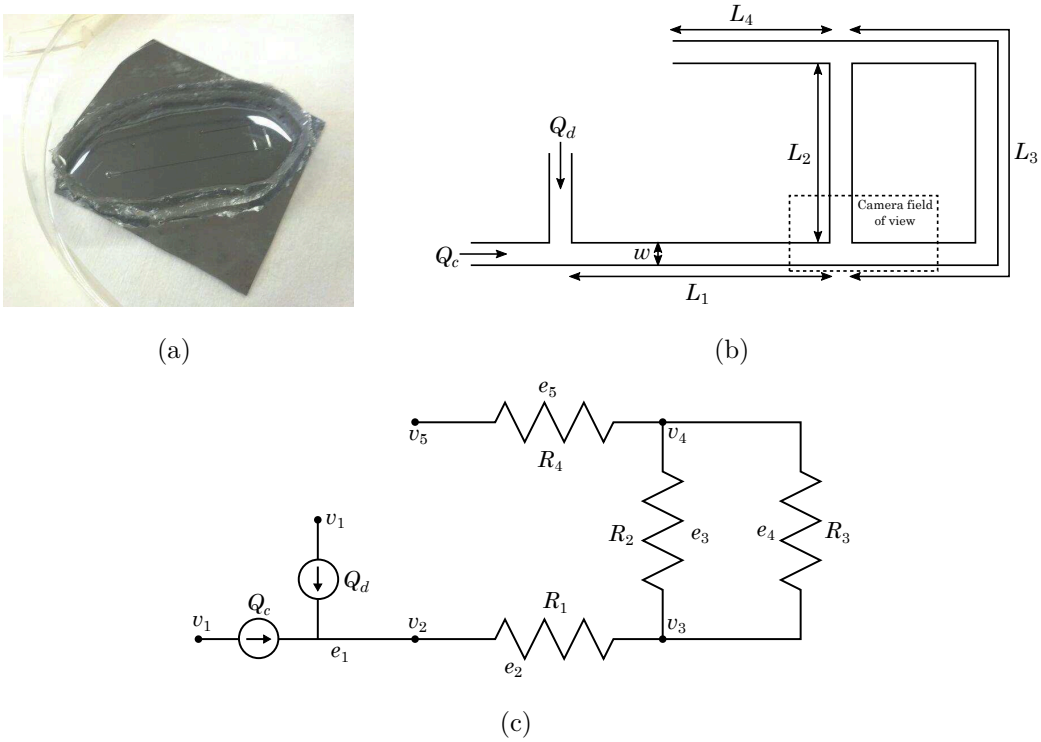

Figure 3.2: (a)Picture, (b)sketch, and (c)electrical equivalent circuit of the loop chip.

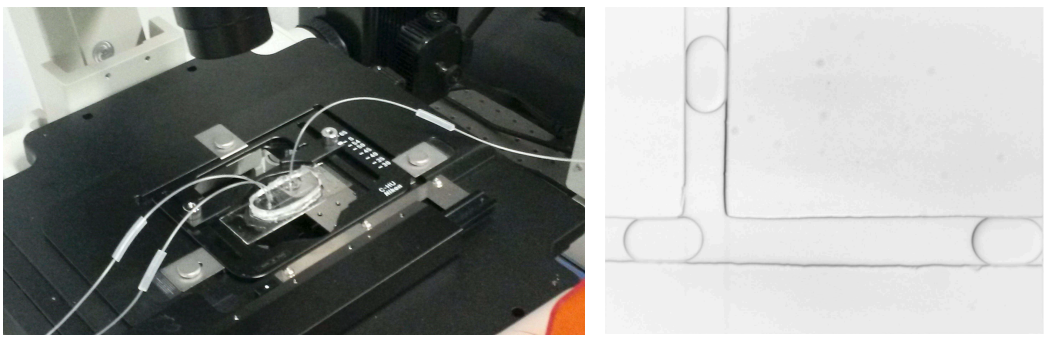

Figure 3.3: (a)Image of the experimental set-up in the laboratory and (b)a frame recorded by the camera.

Description	Value
Channels height	$h = 90\ \mu m$
Channels width	$w = 115\ \mu m$
Input channel length	$L_1 = 25\ mm$
Short branch length	$L_2 = 6\ mm$
Long branch length	$L_3 = 12\ mm$
Output channel length	$L_4 = 10\ mm$

Table 3.1: Geometrical properties of the loop chip.

Continuous phase	Viscosity	$\mu_c = 3\ mPa \cdot s$
$\downarrow$	Density	$\varrho_c = 0.77\ g/mL$
Hexadecane + 2% Span80	Temperature	$T_c = 20°C$
Dispersed phase	Viscosity	$\mu_d = 12.8\ mPa \cdot s$
$\downarrow$	Density	$\varrho_d = 1.15\ g/mL$
Glycerol Aqueous solution (60% w/w)	Temperature	$T_d = 20°C$

Table 3.2: Physical properties of the fluids in the loop chip.

The objective of the experiment was to evaluate the behavior of the droplets in correspondence of the loop (see Fig. 3.2). In particular, we wanted to observe and characterize the switching of the droplets in the two arms of the loop. Note that, because of the different length of the two branches, we expect an uneven distribution of the droplets between the two paths, with a preference for the shortest branch (L_2 in Fig. 3.2(b)) because of its lower resistance (see Sec. 2.1).

With this intent, we imposed the flows of the syringe pumps and, after stabilization of the droplets formation process, we recorded a video of the droplets behavior at the entrance of the loop (a screenshot is reported in Fig. 3.3(b)). The video was then post-processed to determine the fraction of droplets sorted in each of the paths.

This procedure has been repeated for different values of continuous/dispersed

phase flow rates as reported in Fig. 3.4, that collects the results in terms of average percentage of droplets switched into the shortest branch of the loop (L_2 in Fig. 3.2(b)). The percentage of droplets that flows in the longest arm is computed as the complementary.

The experiment has then been replicated by using our simulator. As a first step, we derived the electrical dual of the microfluidic system, as shown in Fig. 3.2(c). Following the method explained in Sec. 3.1, the circuit has been modelled as a graph $G = [V, E]$, where $\{v_i, i = 1, ..., 5\}$ denote the vertices V and $\{e_i, i = 1, ..., 5\}$ all the edges E of the associated graph G. We can identify five different components:

- Edge e_1 is the droplet generator (DG), with vertices v_1 and v_2, modeling the whole T-junction with the continuous and dispersed phase inlets.
- Edge e_2 models the duct of length L_1 between the droplet generator and the loop element. Hence, it is a simple microfluidic channel (CH) with vertices v_2 and v_3.
- Edge e_3, which is associated to the short branch of the loop. In our model, it is represented as a microfluidic channel (CH) of length L_2 with vertices v_3 and v_4.
- Edge e_4 that represents the long branch of the loop and is modelled as a microfluidic channel (CH) of length L_3 with vertices v_3 and v_4.
- Edge e_5, which corresponds to the output channel of the system, and is represented as a microfluidic channel (CH) of length L_4 with vertices v_4 and v_5.

Given this framework, we initialized the model by setting the input values of dispersed/continuous flow rates and used it to simulate the behavior of the microfluidic circuit of Fig. 3.2 and its time dynamics. The input parameters have been changed as for the different experimental sessions, in order to replicate exactly the same settings.

The three plots in Fig. 3.4 report the comparison between simulation results ($*$) and experimental outcomes ($\circ$) in terms of fraction of droplets that got switched along the shortest branch of the loop, for three different values of the continuous phase flow rate.

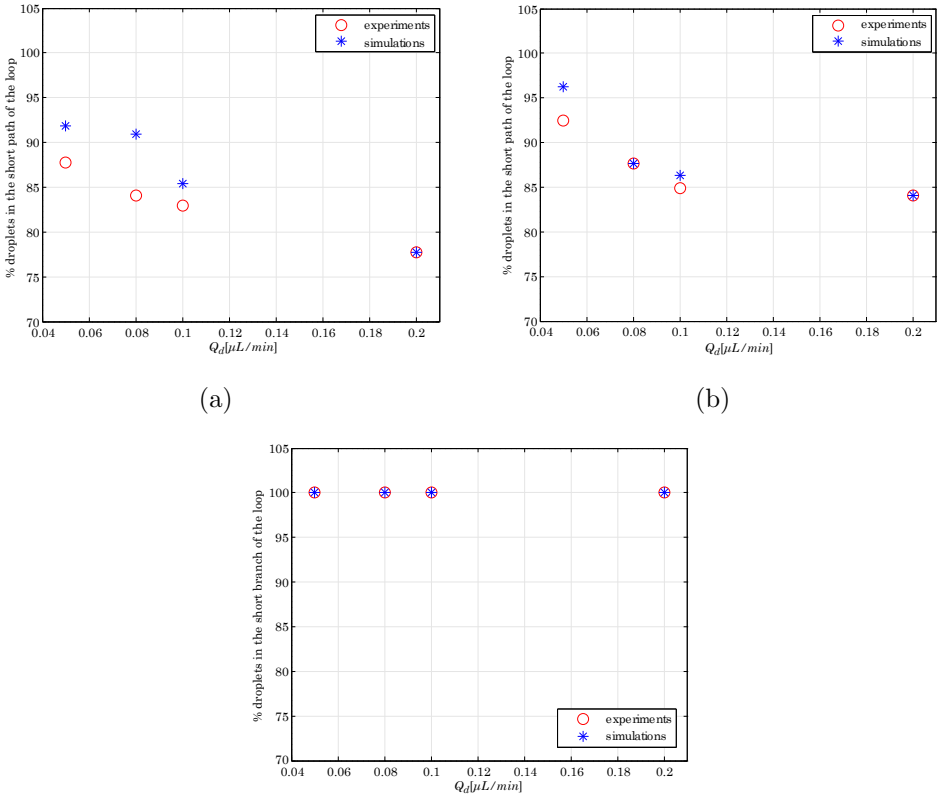

Figure 3.4: Experimental and simulative results representing the percentage of drops that select the shortest path of the loop for (a) $Q_c = 2\ \mu L/min$, (b) $Q_c = 2.5\ \mu L/min$, and (c) $Q_c = 5\ \mu L/min$.

A first consideration that can be drawn from this comparison concerns the reliability of our simulator. From Fig. 3.4, in fact, we can observe that simulation and experimental results are reasonably close, though not always in perfect agreement. This little discrepancy is likely due to the relatively low statistical confidence of the experimental results that we collected, for which we could observe only a low number of droplets (approximately 100) because of the limited memory of the camera.

In detail, data from Fig. 3.4 confirm that, as expected, a large majority of droplets switches into the shortest arm of the loop (L_2). The presence of droplets, however, increases the resistance of that channel and, when the number of droplets in L_2 is sufficiently large, a following droplet will be deflected to the other branch of the loop.

In addition, we note that, for a fixed continuous flow rate, the greater the

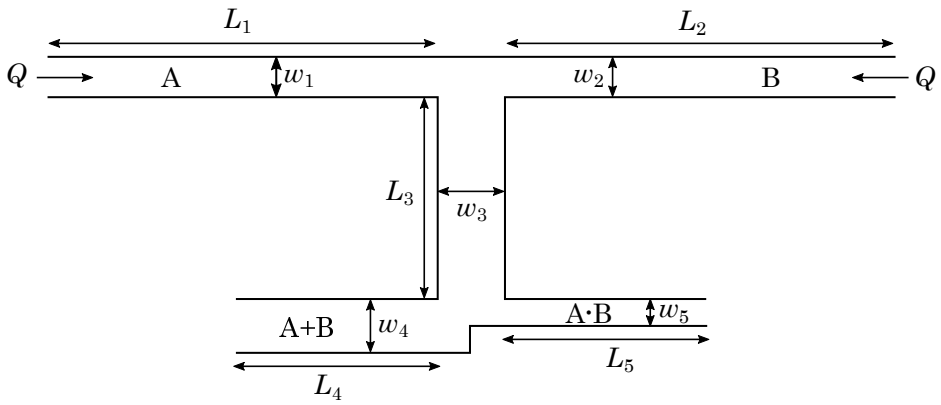

Figure 3.5: Schematic representation of the AND-OR gate.

dispersed flow rate, the lower the fraction of droplets that switch in the short arm. Conversely, fixed the dispersed flow rate, the greater the continuous flow, the greater the percentage of droplets in the short branch. To explain this behavior we shall recall the laws of droplets generation expressed in (1.3) and (1.10), according to which the ratio between dispersed and continuous flow rates affects the length and the inter-distance of the generated droplets. In particular, when $\frac{Q_d}{Q_c}$ decreases, droplets become shorter and more spaced apart. Therefore, the density of droplets in the short branch and their resistance decrease, and less and less droplets are deviated to the other branch. For instance, when $Q_c = 5\ \mu l/min$, droplets are very short and widely spaced apart, so that the maximum additional resistance they can introduce in the short channel of the loop is too low to compensate the initial unbalance between the resistance of the two branches. Thus, in this case, all droplets switch along the short channel.

3.3.2 Bubble logic

As a further validation of our mathematical model, we considered the microfluidic AND-OR gate reported in Fig. 1 of [43], where authors propose microfluidic circuits to realize basic logic ports. We hence reproduced at the simulator the circuit shown in Fig. 3.5, and we simulated the experiment using the parameters reported in Tab. 3.3 and Tab. 3.4. We were able to replicate the exact functioning of the AND-OR gate provided in [43] with identical results. In particular, for the parameters considered, the first droplet arriving at the junction always enters A+B arm (the wider channel with less resistance), increasing consequently the

output flow resistance of A+B and thus directing the following droplet to A·B. As highlighted in [43] and corroborated by our simulations, this behavior occurs as long as the droplets enter the system within a time window $\tau_0 \sim 0.5\ ms$ (for a flow rate of $Q = 0.25\ \mu L/s$).

Description	Value
Channels height	$h = 70\ \mu m$
Width of input channel A	$w_1 = 25\ \mu m$
Width of input channel B	$w_2 = 25\ \mu m$
Width of intermediate channel	$w_3 = 50\ \mu m$
Width of output channel A+B	$w_4 = 30\ \mu m$
Width of output channel A·B	$w_5 = 20\ \mu m$
Length of input channel A	$L_1 = 125\ \mu m$
Length of input channel B	$L_2 = 125\ \mu m$
Length of intermediate channel	$L_3 = 62.5\ \mu m$
Length of output channel A+B	$L_4 = 62.5\ \mu m$
Length of output channel A·B	$L_5 = 62.5\ \mu m$

Table 3.3: Geometrical properties of the AND-OR gate.

Continuous phase	Viscosity	$\mu_c = 1.002\ mPa \cdot s$
	Density	$\varrho_c = 1000\ kg/m^3$
Dispersed phase	Viscosity	$\mu_d = 5.511\ mPa \cdot s$
	Density	$\varrho_d = 1150\ kg/m^3$

Table 3.4: Physical properties of the fluids in the AND-OR gate.

3.3.3 Medium access control circuit

Lastly, we tested our mathematical model with the medium access control (MAC) circuit introduced in [44], to which the reader is referred for a thorough description

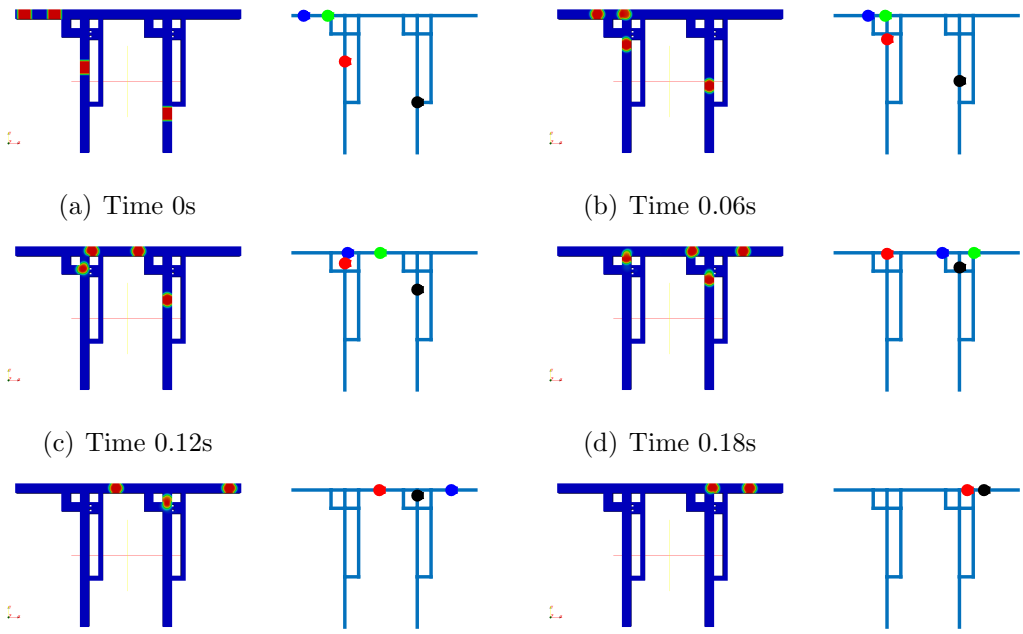

(a) Time 0s (b) Time 0.06s

(c) Time 0.12s (d) Time 0.18s

(e) Time 0.24s (f) Time 0.3s

Figure 3.6: Screenshots of the dynamics in the MAC circuit has predicted by OpenFOAM (left) and by our model (right).

of the circuit. The system considered in the test is shown in Fig. 3.6. The purpose of the MAC circuit is to avoid that the droplets flowing upward along the vertical branches enter the horizontal channel too close to the other droplets flowing in that channel.

We simulated the circuit in OpenFOAM, and repeated the test using our model. Fig. 3.6 reports a series of consecutive snapshots of the graphical output of the two simulators (OpenFOAM on the left). We can observe that the time evolution of the system is basically the same for both simulators, though the execution time of OpenFOAM was 2650 s, while the MATLAB simulation based on our proposed model took around 0.5 s.

4 Microfluidic network with bus topology

As a proof of concept, we applied the theory presented in Sec. 1.1 and Ch. 2 to design a simple purely hydrodynamic microfluidic network with bus topology, as sketched in Fig. 4.1, and develop a proper addressing scheme. Then, we analyse its performance thanks to the simulator described in Ch. 3. The bus topology has been chosen mainly because of its simplicity. However, the design and analysis of other regular topologies, such as a binary symmetric tree, can be performed in a similar manner. More complex topologies (e.g., meshes) will likely require the design of switching elements with multiple inlet and outlet branches and related addressing mechanisms that will likely yield stricter constraints to the design of the whole network. The analysis of the best topology for microfluidic networks is hence an open and quite interesting research topic that we leave for future work.

4.1 Design guidelines and addressing scheme

The system considered in this study consists of a main channel (the *bus*) and N secondary channels, which are perpendicularly linked to the bus via T-junctions at regular distances L_{sep}. Each secondary channel leads to a different MM. The continuous phase is pumped with constant flow rate Q_0 from the leftmost end of the bus, it fills up the bus and all the outlets, and exits from the circuit through the rightmost end of the bus, and into the N MMs. The outlets that lead to the MMs are numbered from 1 to N, starting from the right end of the bus and moving upstream towards the source. The length of the nth branch is denoted by L_n.

The lower part of Fig. 4.1 depicts the equivalent electric circuit of the microflu-

Description	Value
Expansion factor	$\alpha = 5$
Switching factor	$\beta = 1/2$
Additional factor	$\zeta = 1$
Interfacial tension coefficient	$\sigma = 0.046\ N/m$
Breakup parameter	$\chi = 0.187$
Continuous phase viscosity	$\mu_c = 1.002\ mPa \cdot s$
Dispersed phase viscosity	$\mu_d = 145.5\ mPa \cdot s$
Microchannels height	$h = 50\ \mu m$
Microchannels width	$w = 150\ \mu m$
Distance between outlets	$L_{\text{sep}} = 5.4\ mm$

Table 4.1: Main parameters used for the design of the bus networks.

idic bus network, as per the duality principle discussed in Sec. 1.1.3. According to (1.12), the fluidic resistance of the nth outlet is given by $R_n = R(\mu_c, L_n)$, whereas the resistances of the microfluidic segments that separate two consecutive branches are all equal to $R_{\text{sep}} = R(\mu_c, L_{\text{sep}})$. (Note that the resistance of the channels throughout the network depends on the intrinsic resistance of the MMs. Here, for the sake of simplicity, we suppose that the MMs have null resistance. However, with minimal adjustment on the expressions of R_n, the analysis can be generalized to account for a non-null resistance of the MMs.)

As indicated in Fig. 4.1, the equivalent downstream resistance seen after the n-th T-junction can be recursively expressed as

$$R_{\text{eq,n}} = \begin{cases} R_{\text{sep}} & n = 1 \\ R_{\text{sep}} + \dfrac{R_{n-1} R_{\text{eq},n-1}}{R_{n-1} + R_{\text{eq},n-1}}, & n = 2, \dots, N \end{cases} \tag{4.1}$$

Suppose now that we want to send a payload droplet to the n-th MM. To this end, we exploit the addressing mechanism studied in Sec. 2.1. In particular, we inject a pair header/payload of droplets very close to each other. Header droplets are used to sort payload droplets to the desired MM and do not contain useful samples. Accordingly, the system must be designed such that the header always flows through the entire bus without being deflected at any MM to avoid

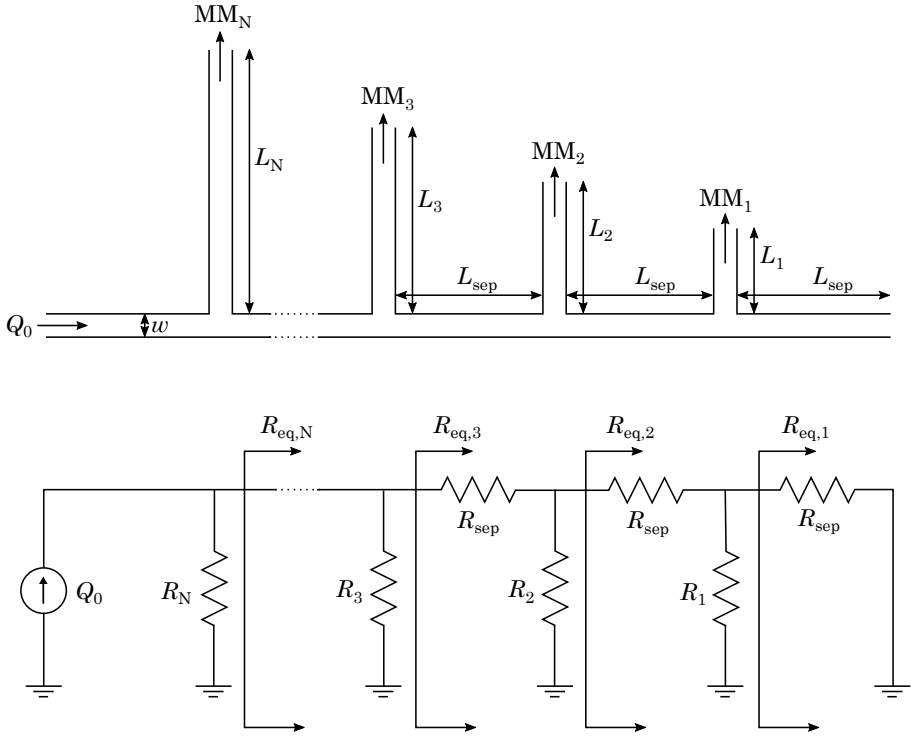

Figure 4.1: Microfluidic network with bus topology (top) and equivalent electric circuit (bottom).

undesirable reactions and finally discarded through the output on the right in Fig. 4.1. Thus, in plain conditions, the path with lowest resistance needs to be represented by the bus. Mathematically, this condition requires that $R_n > R_{\mathrm{eq},n}$ for all $n = 1, \ldots, N$. To meet this goal, we set

$$R_n = \alpha R_{\mathrm{eq},n}\,, \tag{4.2}$$

where $\alpha > 1$ is a design parameter, called the *expansion factor*, whose role will be better analyzed in App. A.1. Now, using (4.1) in (4.2), we get

$$R_n = \alpha R_{\mathrm{sep}} + R_{n-1}\frac{\alpha}{1+\alpha} \tag{4.3}$$

which, solving the recursion, yields

$$R_n = R_{\mathrm{sep}}\alpha(1+\alpha)\left(1 - \left(\frac{\alpha}{1+\alpha}\right)^n\right)\,. \tag{4.4}$$

From (4.4) we see that, for any $n = 1, \ldots, N-1$, it holds

$$R_n < R_{n+1} \quad \text{and} \quad R_{\mathrm{eq},n} < R_{\mathrm{eq},n+1} \tag{4.5}$$

according to which the length L_n of the secondary branches increases with n, as reflected by (1.12) and depicted in Fig. 4.1.

Now, we recall that the header droplet increases the resistance of the channel that it occupies according to (1.14). Exploiting this fact, we can deflect the payload towards any target MM by properly selecting the header length. Specifically, let $\rho_{H,n}$ denote the resistance produced by a header to steer a closely following payload towards the nth MM. In order to compute it, we have to impose the following conditions:

- The payload must take the n-th branch at the corresponding T-junction. Therefore
$$\rho_H(n) > R_n - R_{\text{eq},n} \tag{4.6}$$
- The payload cannot flow into any of the outlets that it encounters before the n-th branch. This is guaranteed by setting
$$\rho_H(n) < \min\{R_j - R_{\text{eq},j};\, j = n+1, \dots, N\} \tag{4.7}$$

Putting (4.6) and (4.7) together and noting that $R_j - R_{\text{eq},j}$ increases with j, we get
$$R_n - R_{\text{eq},n} < \rho_H(n) < R_{n+1} - R_{\text{eq},n+1} \tag{4.8}$$
in which we conventionally set $R_{N+1} - R_{\text{eq},N+1} = \infty$. Using (4.2) in (4.8) we can express the header resistance as
$$\rho_H(n) = \frac{\alpha - 1}{\alpha}\left(\beta R_{n+1} + (1-\beta)R_n\right) \tag{4.9}$$
where $\beta \in (0,1)$ is a design parameter, called *switching factor*, whose role is studied in App. A.1. Note that, from (4.9) and (4.5), it follows that $\rho_H(n)$ increases with n. Eventually, according to (1.14), this means that longer header droplets are needed to sort the payload to the target MM as n increases.

Following the guidelines given in this section and further discussed in App. A.1, we designed the microfluidic bus network and implemented the proposed addressing scheme. The final parameters, collected in Tab. 4.1, were chosen such that the system behaves as desired and the corresponding performance are investigated in Sec. 4.3. The equations derived for the bus network with simple T-junctions show that all the different part of the network are interdependent and, consequently, the presence of a single droplet in any position of the circuit affects the route of

any other droplet. This makes the design of the system quite complicated and requires to use a sort of time division access policy that we will call *exclusive access* for which only a single header/payload pair can be inside the network at a time. In fact, the presence of additional droplets would invalidate the theoretical analysis seen so far and make the route of the droplets unpredictable.

As anticipated in Sec. 2.2 and illustrated in the next section, a solution to avoid these issues is to use bypass channels at the T-junctions. This element, in fact, decouples the sorting mechanism at the T-junction from the rest of the circuit.

4.2 Bus network with bypass channels

To evaluate the potential benefits brought by bypass channels, we consider the same bus network presented before where we replace the standard T-junctions with bypass T-junctions, as depicted in Fig. 4.2 along with the associated electric circuit.

Once again, the MMs interconnected by the network are numbered from 1 to N starting form the rightmost side of the bus channel and moving upwards towards the droplet source. At any bifurcation, the incoming channel splits in two daughter channels 1 and 2, whose endpoints are connected through the bypass channel. Channel 1 is part of the bus while channel 2 is the first portion of the outlet towards the corresponding MM. Moreover, the channel that departs from the node that joins channel 1 and the bypass is named channel 3, while we denote as channel 4 the duct that leads to the MM. Following this notation, we indicate the resistance of channels 1, 2, 3 and 4 at the n-th T-junction with $R_{1,n}$, $R_{2,n}$, $R_{3,n}$, and $R_{4,n}$ respectively, and similarly for their lengths and flow rates.

Assuming $R_{\text{byp}} \simeq 0$, as discussed in Sec. 2.2, the equivalent resistance seen downstream of the n-th junction can be recursively expressed as

$$R_{\text{eq},n} = \frac{R_{1,n}R_{2,n}}{R_{1,n} + R_{2,n}} + \frac{(R_{3,n} + R_{\text{eq},n-1})R_{4,n}}{R_{3,n} + R_{\text{eq},n-1} + R_{4,n}} \tag{4.10}$$

with $R_{\text{eq},0} = 0$. Then, given the input flow rate Q_0 of the system, we can compute the distribution of the flow rate in the whole network. Solving the electric circuit

in Fig. 4.2, in fact, we have

$$\begin{cases} Q_{1,n} = Q_{3,n+1}\dfrac{R_{2,n}}{R_{1,n}+R_{2,n}} \\ Q_{2,n} = Q_{3,n+1}\dfrac{R_{1,n}}{R_{1,n}+R_{2,n}} \\ Q_{3,n} = Q_{3,n+1}\dfrac{R_{4,n}}{R_{3,n}+R_{\mathrm{eq},n-1}+R_{4,n}} \\ Q_{4,n} = Q_{3,n+1}\dfrac{R_{3,n}+R_{\mathrm{eq},n-1}}{R_{3,n}+R_{\mathrm{eq},n-1}+R_{4,n}} \end{cases} \tag{4.11}$$

where $Q_{3,N+1} = Q_0$.

We now need to determine the system parameters in order to achieve the desired behavior for the droplets applying the same rationale seen in Ch. 4.1. First of all, in plain conditions, i.e. without droplets, the flow rate along the bus must be the strongest so that header droplets will always flow all the way across the bus until its end from which they are discarded. According to (2.6), the switching behavior at the nth bypass T-junction is only determined by the parallel between $R_{1,n}$ and $R_{2,n}$. Therefore, to satisfy this condition we simply require

$$R_{1,n} < R_{2,n}\,. \tag{4.12}$$

Secondly, we need to establish the proper header resistance $\rho_H(n)$ to deviate a closely following payload droplet towards the n-th MM. To this end, two different conditions must hold

- The payload droplet must flow along the bus till it reaches the nth bifurcation. Mathematically, this requires $\rho_H(n) < \min\{R_{2,j} - R_{1,j};\, j = n+1, \ldots, N\}$ where we conventionally set $R_{2,N+1} - R_{1,N+1} = \infty$.

- The payload droplet must take the nth outlet when it arrives at the corresponding bifurcation, which requires $\rho_H(n) > R_{2,n} - R_{1,n}$.

Combining the two conditions we get

$$R_{2,n} - R_{1,n} < \rho_H(n) < R_{2,n+1} - R_{1,n+1}, \tag{4.13}$$

from which we see that the length of the header droplet must increase with n. However, there are still some degrees of freedom in the network design. For instance, we decide to set both $L_{1,n}$ and $L_{3,n}$ equal to $L_{\mathrm{sep}}/2$. In this way, the

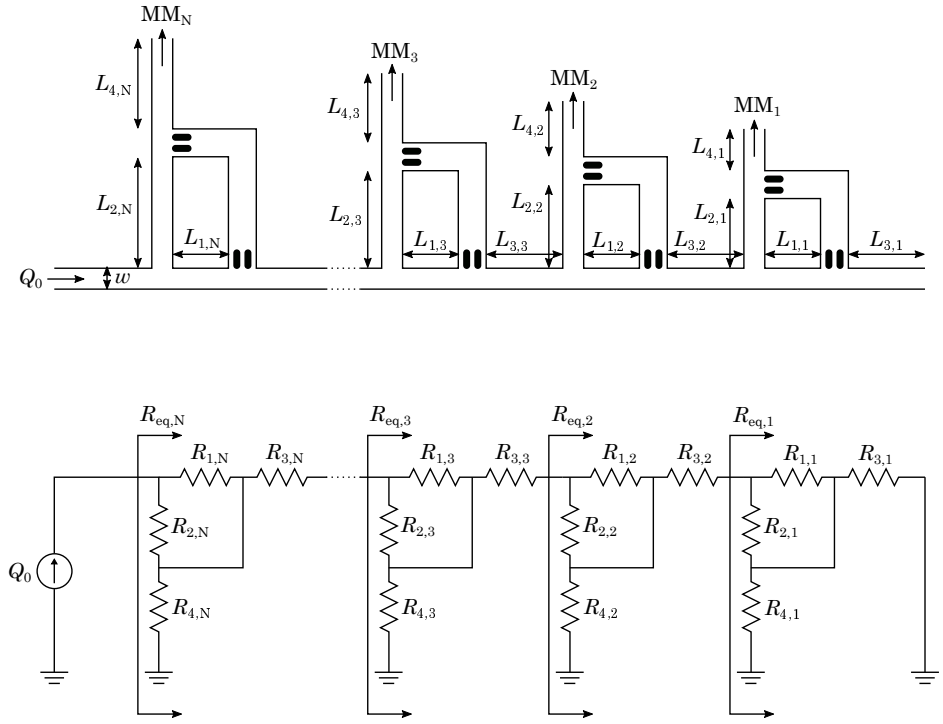

Figure 4.2: Microfluidic bus network with bypass channels (upper) and equivalent electric circuit (lower).

distance between two consecutive T-junctions is constant and identical to the separation that we had in the microfluidic network with simple T-junction, making the comparison between the two systems fair. Thus, we have $R_{1,n} = R_{3,n} = R_{\text{sep}}/2$ for $n = 1, ..., N$. Under this assumption, (4.13) yields $R_{2,n+1} > R_{2,n}$ such that $L_{2,n}$ and $R_{2,n}$ increase with n, as depicted in Fig. 4.2.

Then, to satisfy both (4.12) and (4.13) we set

$$R_{2,n} = R_{1,n}(1 + n\zeta) = \frac{R_{\text{sep}}}{2}(1 + n\zeta), \tag{4.14}$$

for some $\zeta > 0$ called *additional factor*, so that ρ_n can be expressed as

$$\rho_H(n) = \beta(R_{2,n+1} - R_{1,n+1}) + (1 - \beta)(R_{2,n} - R_{1,n}) = \frac{R_{\text{sep}}}{2}\zeta(n + \beta). \tag{4.15}$$

Concerning the length $L_{4,n}$, we see that, according to (4.11), large values of $R_{4,n}$ favors the flow of droplets along the bus and penalizes the speed along the outlet branches towards the MMs. Thus, the optimal value of $R_{4,n}$ comes from the tradeoff between these two effect. However, for fair comparison with the bus

network with simple T-junctions, in this study we simply set

$$R_{4,n} = 5n\frac{R_{\text{sep}}}{2}\,. \tag{4.16}$$

In this way, in fact, we obtain that the average lengths of the branches are almost equal to those of the previous network.

The simplification in the design of the network is not the only benefit brought by the utilization of the bypass channel. The new network, in fact, is more robust to perturbations and can easily accommodate more efficient policies than the simple exclusive access. An analysis in this sense is provided in the next section.

4.2.1 Multiple access scheme

Thanks to the introduction of the bypass channel, the switches in the new bus network are isolated from the rest of the network. So, contrary to the previous case, the presence of multiple header/payload pairs may not compromise the functioning of the network but rather improve it, as we will see in Sec. 4.3. Indeed, one may think of a multiple access strategy where a train of header/payload pairs separated by a distance δ_{pairs} is injected in the system concurrently.

Suppose, for example, that we want to send several payloads to the same microfluidic machine, say the n-th MM. Accordingly, each payload will be preceded by a header with resistance $\rho_H(n)$ as per (4.15) and followed by another header/payload pair at distance δ_{pairs}. Thanks to the effect of the bypass, the path taken by a payload at the n-th T-junction will not be affected by the presence of other droplets inside the network except for those contained in the channels delimited by the corresponding bypass (i.e. channels 1 and 2 of the n-th bifurcation in Fig. 4.2). Thus, if δ_{pairs} is large enough to guarantee that each header/payload pair has already left those channels when the following pair reaches the n-th T-junction, the network will behave as desired and all payloads will be correctly conveyed to the n-th MM.

This principle is exploited in the next section where we show the corresponding performance and compare it with the previous policies.

4.3 Performance analysis

Interconnecting different MMs through purely hydrodynamic microfluidic networks can potentially bring a number of advantages in terms of device flexibility, manufacturing costs, number and complexity of enabled analysis processes, and so on. From a networking perspective, some performance figures of interest are the number of supported MMs in the network, the average time to deliver a payload droplet to the intended MM, the average number of payload droplets conveyed per unit of time, the probability of errors (which include droplets coalescence, merging or splitting, wrong turns at junctions, and so on), the overhead that can be intended as the cost of producing header droplets to control the payload droplets, and others.

However, in this work we focus on the *throughput* performance metric. Importing the term from the the ICT domain where it generally defines the average number of useful bits delivered to the intended destination per unit of time, we can reinterpret it, in the microfluidic context, as the average volume of payload droplets delivered to the intended MM in unit of time. Mathematically

$$S = \lim_{t \to \infty} \frac{V(t)}{t} \tag{4.17}$$

where $V(t)$ is the total volume of dispersed fluid delivered to the intended receivers in time t.

Then, we used the parameters listed in Tab. 4.1 to design both the bus network depicted in Fig. 4.1 and Fig. 4.2, assuming that we have $N = 10$ connected MMs, and implement them in our simulator (cf Ch. 3). In Fig. 4.3 and Fig. 4.4 we show the throughput achievable when targeting different MMs (namely, number 3, 4, and 7) as a function of the payload length for the two systems. The curves are obtained directing all the traffic to the same MM under the exclusive access policy.

Note that the trend of the two graphs is quite alike. Indeed, similar considerations can be drawn for the two systems. For instance, the throughput in both networks is lower for MMs closer to the source (larger n). The reason for this result is twofold. Firstly, according to the design guidelines of the systems, the length of the ramifications increases rapidly with n and, consequently, droplets need to travel longer distances to reach the target MM. Secondly, the header droplet length $\ell_H(n)$ also increases with n, thus limiting the maximum input

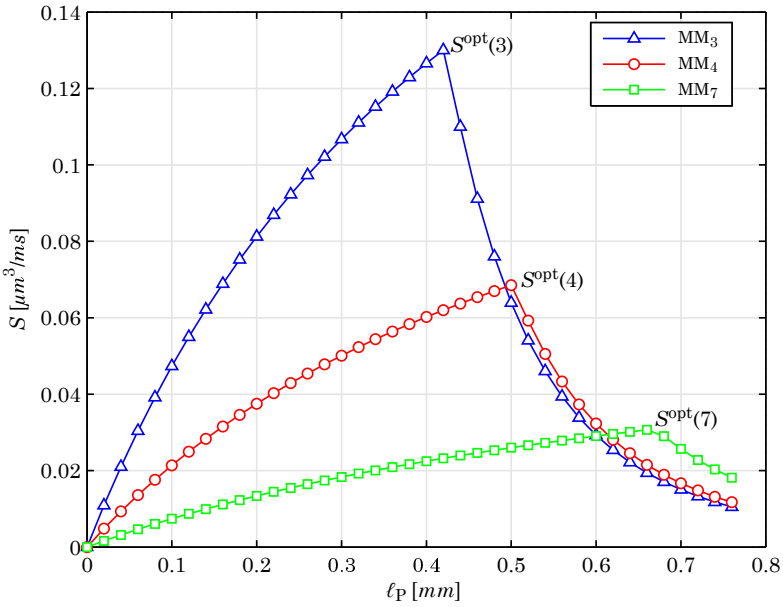

Figure 4.3: Throughput as a function of the payload length for the bus network with simple T-junctions.

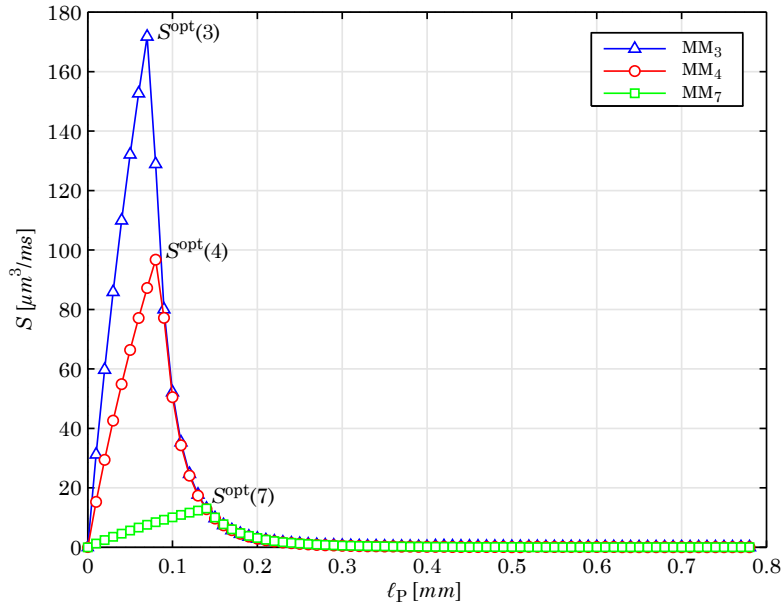

Figure 4.4: Throughput as a function of the payload length for the bus network with bypass channels.

speed $u_0 = \frac{Q_0}{wh}$ according to (2.3).

Moreover, given the n-th target MM, we see that the throughput starts increasing with the payload length ℓ_P until it reaches a maximum and then drops quickly. The analysis shows that the corresponding peak is obtained for $\ell_P = \ell_H(n)$, i.e. when the payload length is equal to the length of the header droplet that sort the payload towards the n-th MM. For larger values of ℓ_P, in fact, the input flow rate and, hence, the speed of the droplets must be decreased according to (2.2) to avoid break-ups at the junctions. Eventually, this leads to a significant reduction of the throughput. A somehow unexpected consequence of this fact is that, even operating under exclusive access policy, if the length of the payload that we want to send is large, it is more convenient to split it and send multiple sub-droplets rather than keeping it entire and deliver it in one go.

Beside these analogies between the two networks, it is clear that the configuration with the bypass largely outperforms the solution with simple T-junctions. Comparing Fig. 4.3 and Fig. 4.4, in fact, we can see that the maximum throughput achievable by the network with bypass channels is 3 order of magnitude greater than the corresponding values in the other network, even if we adopt the exclusive access policy, which is rather conservative in the utilization of the network.

In addition, as we have explained in Sec. 2.2, bypass channels decouple the behavior at the junction from the rest of the network, which is not true for simple T-junction switches. Exploiting this property, we can treat every switch in the bypass bus network separately from the rest of the system, which allows us to design advanced access policies as described in Sec. 4.2.1.

Thus, we now remove the exclusive access assumption for the network in Fig. 4.2 and consider the case where a train of header/payload droplets intended for the same MM is injected into the circuit. Depending on the target MM, we set the length of the payload droplets equal to the value that guarantees the maximum throughput in the exclusive access scenario (i.e., the values at the peaks in Fig. 4.4). Then, we vary the distance δ_{pairs} or, equivalently, the injection time $t_{\text{pairs}} = \frac{\delta_{\text{pairs}} wh}{Q_0}$ between two consecutive header/payload pairs in the input circuit.

In Fig. 4.5 we report the throughput when varying such parameter. The curves are limited on both sides by specific thresholds and the results show a non-linear growth of the throughput when reducing δ_{pairs}. In particular, the right-most values in the graph equal the throughput of the exclusive access policy.

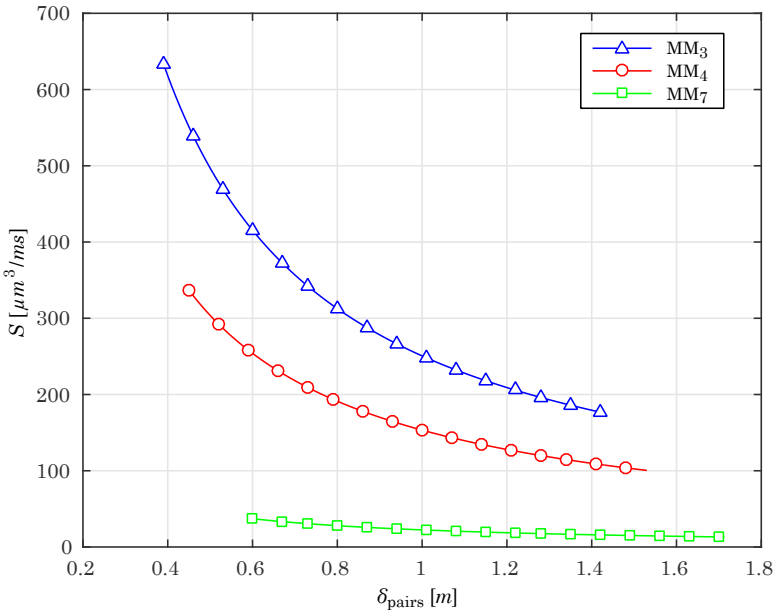

Figure 4.5: Throughput as a function of the distance between consecutive pairs of droplets for the multiple access policy.

The corresponding values of δ_{pairs}, in fact, are exactly the distance for which a header/payload pair is injected into the system right after the previous one has left it, as in the exclusive access policy. On the other hand, we cannot reduce δ_{pairs} too much, otherwise some payload droplets would be delivered to the wrong MM. Indeed, the left-most values in Fig. 4.5 correspond to the minimum spacing for which a header/payload pair reaches the target switch right after the previous pair has left the branches of the same bifurcation delimited by the bypass (channels 1 and 2 in Fig. 4.2).

As expected, the introduction of multiple access techniques further increases the performance of the network with respect to the exclusive access policy. Following the previous reasoning, this gain corresponds to the difference between the maximum and the minimum throughput in the curves of Fig. 4.5.

5

Transmit information in microfluidic systems

In the last few years, physics researchers have advanced the idea of exploiting microfluidic systems to build tiny computing units [31, 43], and the possibility of using them in order to realize simple boolean functions has been experimentally proved. Even more interesting is the recent proposal of introducing communication notions in the microfluidic domain: a preliminary step in this direction was done in [41,45], where the authors proposed to encode information in the distance between consecutive drops.

Inspired by these works, we carried out some experiments using real microfluidic devices with the intent of investigating a proper way to transmit information in a microfluidic channel. In particular, we exploited the T-junction droplet generator governing laws presented in Sec. 1.1 in order to modulate the length of generated droplets (and, consequently, their interdistance) and develop a sort of binary Pulse Amplitude Modulation scheme. Our aim is to design a microfluidic communication system in which the information is encoded in the droplets length/interdistance.

To this end, we considered a 4-levels modulation scheme with symbols $s^{(i)}$, $i \in \{0, 1, 2, 3\}$, which are associated, respectively, to the bit strings $\{00, 01, 10, 11\}$. For each symbol we set a different level for the dispersed phase flow $Q_d^{(i)}$ in order to obtain different droplet lengths $\ell_d^{(i)}$ and interdistances $\delta^{(i)}$ as per (1.3) and (1.10). The continuous phase flow Q_c is fixed. We then investigate the performance of a T-junction in generating trains of droplets with a given size and interdistances.

This theoretical model was tested by means of real-case experiments conducted in our laboratories. In the reminder of the chapter we describe such experimental setup, focusing on the characterization of the methodologies and hard-

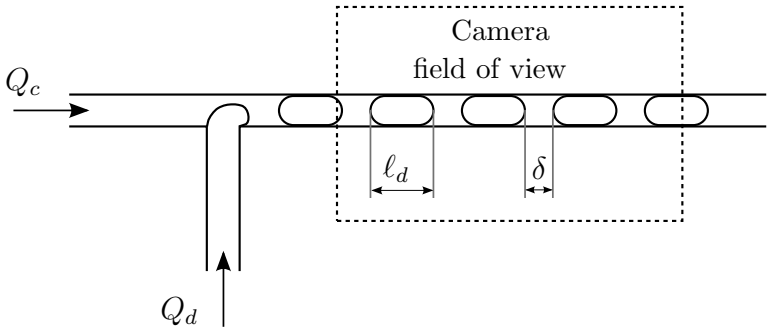

Figure 5.1: Sketch of the experimental setup for the information encoder.

ware used. Then, we assess the symbol error probability for a PAM-like system in which modulation is realized by exploiting the droplet length/interdistance. Finally, we discuss the challenges and the performance tradeoff of such a system.

5.1 Experimental anlysis

The microfluidic device we considered for our experiments is a simple T-junction droplet generator. The device, made of PDMS, was fabricated using the photolithography technique. We designed the chip with channels of height $h = 90\,\mu m$ and width $w = 115\,\mu m$. The continuous and the dispersed phase are injected in the system through two PHD 2000 Harvard Apparatus syringe pumps, while the output channel opens on air.

The continuous phase is a solution of Hexadecane, an alkane hydrocarbon, and Span80, a nonionic surfactant that lowers the surface tension. The dispersed phase is instead an Glycerol Aqueous solution (Glycerol 60% weight/weight).

We connected a camera to a microscope to record real-time videos of the experiments (see *www.youtube.com/channel/UCSAv6jxxZq4xmmFSpNKyoSw*). The camera takes 20 frames per second, for a time duration of 50 seconds per experiment. The camera field of view is centered on a section of the output channel of the T-junction, as shown in Fig. 5.1. Hence, the droplet length/interdistance are obtained from the acquired frames through an image processing script.

We set the continuous phase flow $Q_c = 5\,\mu l/\text{min}$, whereas the dispersed phase phase flow $Q_d^{(i)}$ takes values in the set $\{0.5, 1, 1.5, 2\}\,\mu l/min$, for symbols $s^{(i)}$, $i \in \{0, 1, 2, 3\}$ respectively. For each value of $Q_d^{(i)}$ the system is left running for a sufficiently long time. The camera connected to the microscope acquires 1000

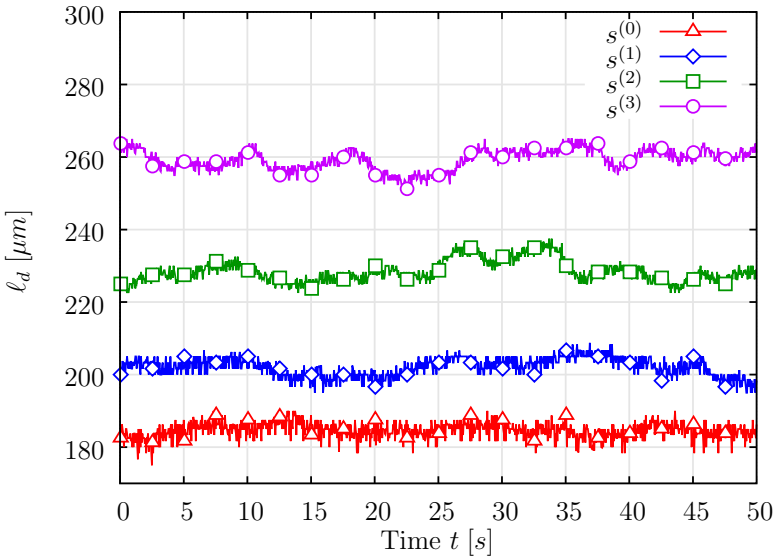

Figure 5.2: Droplet lengths results.

frames, which are post processed to obtain the values for $\ell_d^{(i)}$ and $\delta^{(i)}$ in the 50 s acquisition time interval.

5.1.1 Results

Fig. 5.2 and Fig. 5.3 show the results, obtained through image processing, for $\ell_d^{(i)}$ and $\delta^{(i)}$. It can be noted that there are non negligible fluctuations around the average values. Tab. 5.1 reports the mean value, as well as the standard deviation for both the droplet lengths and the interdistances. Specifically, we define $\bar{\ell_d}^{(i)}$ and $\sigma_\ell^{(i)}$ as the average droplet length and the standard deviation for the i-th symbol respectively. Similarly, $\bar{\delta}^{(i)}$ and $\sigma_\delta^{(i)}$ indicate the average interdistance and the standard deviation of the droplets interdistance for the i-th symbol.

Symbol error probability

In order to evaluate the performance of the microfluidic communication system we assume that, for each symbol, the length/interdistance can be modeled as a Gaussian random variable $\mathcal{N}^{(i)}(\mu_i, \sigma_i^2)$, where $\mu_i \in \{\bar{\ell}_d^{(i)}, \bar{\delta}^{(i)}\}$ and $\sigma_i \in \{\sigma_\ell^{(i)}, \sigma_\delta^{(i)}\}$ depending on whether we consider the length of the droplets or their inter-distance as the modulating quantity. Although further analysis is needed, the normal approximation for these quantities appears reasonable, as qualitatively proved

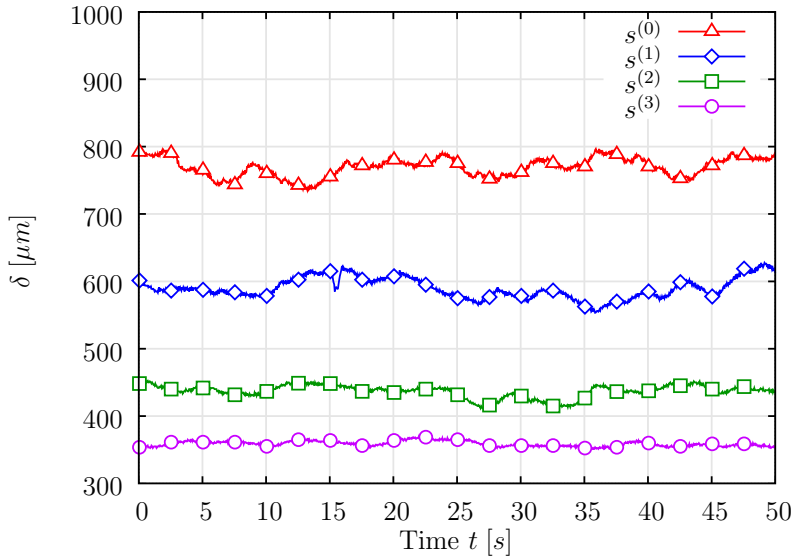

Figure 5.3: Droplet interdistances results.

by Fig. 5.4 that shows the empirical cdf of the droplet length for symbol $s^{(0)}$, as well as the theoretical normal cdf. As it can be seen, the theoretical curve approximates tightly the empirical cdf. The same assumption holds also for the other symbols, and for the distribution of the interdistances.

Given the Gaussian random models, we identify the decision thresholds for the decoding of the symbols at the receiver of the microfluidic communication system as:

$$\text{thr}_{\ell}^{(i,i+1)} = \frac{\bar{\ell}_d^{(i)} + \bar{\ell}_d^{(i+1)}}{2} \ , \ i \in \{0,1,2\} \ ; \tag{5.1}$$

for the droplet lengths. Correspondingly we use $\bar{\delta}^{(i)}$ for the evaluation of the thresholds for the interdistance case, $\text{thr}_{\delta}^{(i,i+1)}$. The values of the decision thresholds are reported in Tab. 5.1

Fig. 5.5 and Fig. 5.6 show the probability distribution functions (pdfs) for the droplet lengths and the interdistances. It can be noted that in both cases the pdfs of different symbols are sufficiently spaced apart and that the overlapping between pdfs is minimal.

Following the standard procedure for a PAM-like modulation system, the error probability is derived by first computing the conditional probabilities of error and then applying the total probability theorem. Assuming equally likely symbols,

i	$\bar{\ell}_d^{(i)}$	$\sigma_\ell^{(i)}$	$\text{thr}_\ell^{(i,i+1)}$	$\bar{\delta}^{(i)}$	$\sigma_\delta^{(i)}$	$\text{thr}_\delta^{(i,i+1)}$
0	184.52	2.26	193.29	769.65	14.04	679.5107
1	202.05	2.56	215.26	589.37	15.30	513.0877
2	228.47	3.08	243.85	436.80	9.44	397.8275
3	259.24	2.88	⁄	358.85	4.09	⁄
e_ℓ	$1.80 \cdot 10^{-5}$			e_δ	$8.95 \cdot 10^{-7}$	

Table 5.1: Numerical results for the droplet lengths, interdistances, decision thresholds and total symbol errors in the four experimental setup considered.

we have:

$$e = \frac{1}{4} \sum_{i=0}^{3} P(E|s^{(i)}) \, , \tag{5.2}$$

where $P(E|s^{(i)})$ is the conditional probability of error when symbol $s^{(i)}$ is transmitted, and it is obtained using the decision thresholds and the symbol pdf. The last row of Tab. 5.1 summarizes the results for the error probability when using the droplet length, e_ℓ, or the droplets interdistance, e_δ, as the modulating variable.

5.2 Open research challenges

The analysis provided in this chapter shows the feasibility of extending communication concepts to the microfluidic domain. Specifically, we illustrate how to implement basic modulation techniques in microfluidic systems. On this basis, we carried out some experiments in order to investigate simple communication solutions in microfluidic channels using droplet length and interdistance modulation.

Results show that the noise that affects both droplet length and inter-distance can be modeled as a zero-mean normal random process, whose variance, however, depends on the transmitted symbol, i.e., on the working point of the system. More specifically, droplet-based modulation exhibits stronger noise for symbols associated to relatively short droplets, while interdistance-based modulation is more

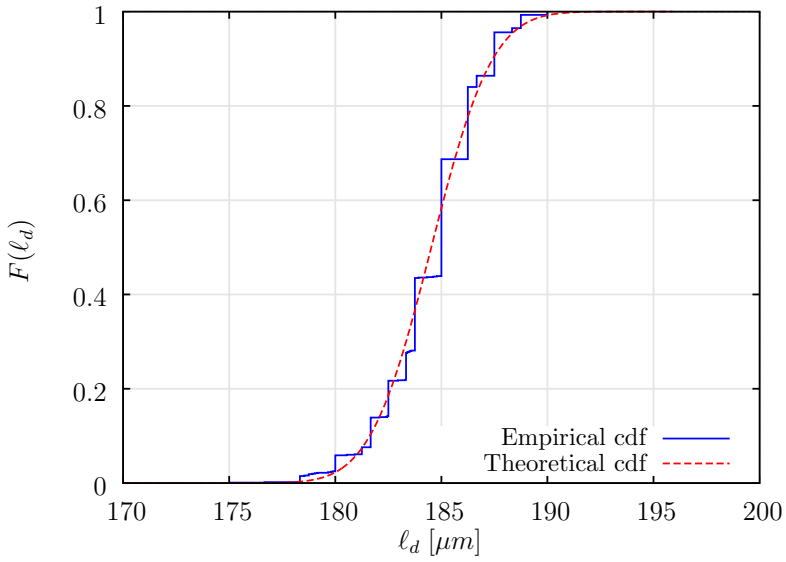

Figure 5.4: Empirical and theoretical cdfs of the droplet length for symbol $s^{(0)}$.

noisy when droplets are more spaced apart. Overall, however, droplet interdistance appears to be more robust a signal than droplet length for PAM modulation, though both techniques can achieve relatively low bit error probability in the considered scenarios. Although this analysis moves some initial steps toward the performance characterization of a microfluidic-based PAM transmission system, the way to go is still very long and unexplored. To begin with, the impact of the hardware used in the experiments shall be characterized, in order to sort out the microfluidics effects from other sources of noise. As an example, the transient exhibited by the droplet generation circuit when changing the volumetric flow rates at the input has not yet been analyzed, nor has it been considered the actual bitrate that can be achieved with such a mechanism. To this end, we are planning to carry out further experiments that will hopefully shed light on these and other aspects.

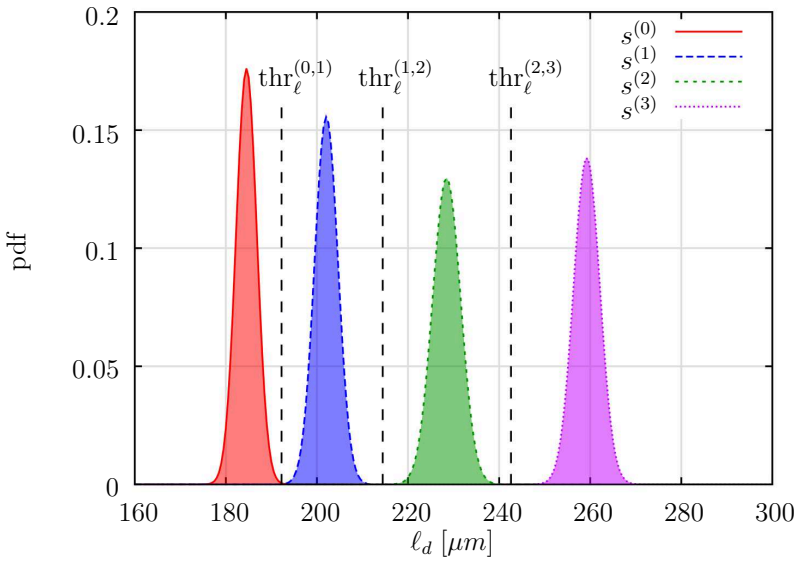

Figure 5.5: Estimated pdfs of the four symbols when using droplet length modulation.

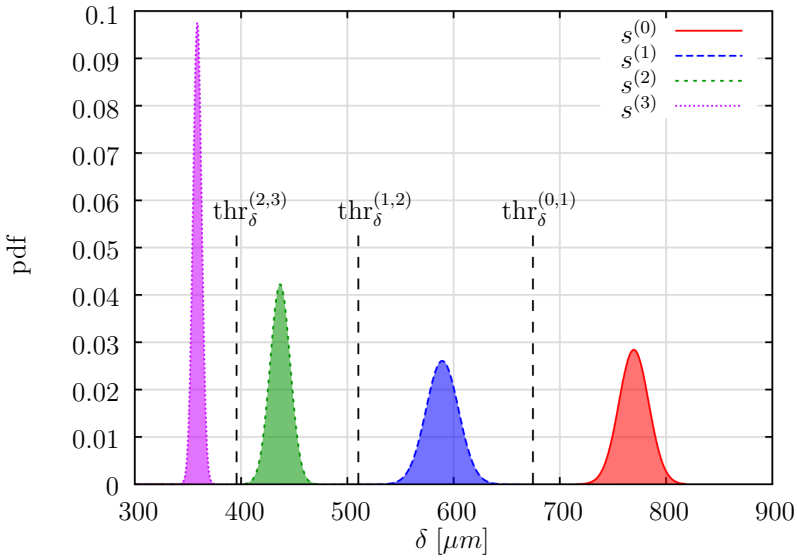

Figure 5.6: Estimated pdfs of the four symbols when using droplet interdistance modulation.

6 Conclusions

In this work we have illustrated the main concepts of droplet-based microfluidic and proposed simplified mathematical models that capture the main interrelations between the system parameters. If suitably controlled, these behaviors can be used to implement basic networking functionalities, such as addressing and switching, using totally passive hydrodynamic techniques. Based on such models, we developed a simulator that reproduces the time dynamics of an arbitrarily complex microfluidic network at a macroscopic level and, thus, is able to predict the path of droplets inside it. As a proof of concept, we applied the simulator to design a pure hydrodynamic network with bus topology, for which we derived the throughput, in terms of average volume of dispersed flow delivered to the intended MM in the unit time. Finally, we also showed how it is possible to encode information in the droplets length/interdistance.

All these results provide a first evidence of the potentialities of microfluidic networking. The ultimate objective of this work is to open the way to a new, challenging, research ground that aims at the realization of networking technologies for microfluidic applications, enabling the realization of a new generation of LoCs that are more flexible, less expensive, and more effective. Some of the basic building blocks of the microfluidic network considered in this work have been realized and tested in our laboratories. Although the experimental results are still preliminary and partial, they bode well for the feasibility of purely hydrodynamic microfluidic networks, and foster the viability of this new research field.

M2M COMMUNICATIONS

7 Introduction

As telecommunication technologies continue to evolve rapidly, fueling the growth of service coverage and capacity, new use cases and applications are being identified. Many of these new business areas (e.g., smart metering, in-car satellite navigation, e-health monitoring, smart cities) involve fully-automated communication between devices, without human intervention. This new form of communication is generally referred to as Machine-to-Machine (M2M) Communication, or Machine-Type Communication (MTC), while the involved devices are called Machine-Type Devices (MTDs). Examples of common MTDs are environmental and biomedical sensors, actuators, meters, radio frequency tags (RFtags), but include also smartphones, tablets, vehicles, and cameras.

The number of MTDs is continuously growing, together with the set of M2M applications and services that they enable. As a matter of fact, MTDs are key elements in the emerging Internet of Things (IoT) and Smart City paradigms [46,47], which are expected to provide solutions to current and future social-economical demands for sensing and monitoring services, as well as for new applications and business models in areas like building and industrial automation, remote and mobile healthcare, elderly assistance, intelligent energy management and smart grids, automotive, smart agriculture, traffic management, and many others [48].

In the last years the potential of the M2M paradigm has been recognized by both academia and industry, which have generated a number of studies, protocols and products oriented to the support of M2M services. Worth mentioning for their popularity and market penetration are the IEEE 802.15.4 standard for low-bitrate short-range transmissions [49], the 6LowPAN protocol suite for low power devices [50], the ZigBee solution for MTD interconnection in small wireless

sensor networks [51], and other communication systems like EIB/KNX, LON and BACnet for home automation [52]. Another interesting technology that can be adapted to M2M services is the 3GPP Proximity-based Service (ProSe) protocol [53]. The idea behind it is to offload the network by exploiting the physical proximity of the terminals, e.g., enabling direct communication between user devices, or limiting the signaling to the local area, without involving core network elements.

Despite the appeal of such solutions, the potential of the M2M vision can be fully unleashed only when MTDs connectivity will be possible everywhere, with no (or minimal) configuration, and without the need for deploying additional devices, such as gateways or concentrators. Unfortunately, the technologies that can support some form of MTC are currently incapable of fulfilling the demand for ubiquitous access of MTDs to the communication systems. Local network solutions, such as ZigBee/6LoWPAN or IEEE 802.11ah extension for MTC, are suitable to interconnect MTDs in the same local area, but neither are able to offer coverage everywhere nor they guarantee highly reliable coordinated control of the network. On the other hand, the ubiquitous coverage offered by satellite connections has prohibitively high cost, both economically and in terms of energy consumption, and pose significant challenges when used in indoor environments. The proliferation of M2M communications, hence, call for terrestrial radio technologies that are capable of providing widespread (ideally ubiquitous) coverage, with extremely low energy consumption, low complexity at the end device, possibly low latency, and minimal cost per bit. A few proprietary solutions that satisfy some of these requirements have been recently commercialized, though the deployment of a new infrastructure network at a global scale is economically challenging. Therefore, the most natural and appealing solution is to add MTC to the services provided by the existing cellular networks. Indeed, cellular networks have a world-wide established footprint and are able to deal with the challenge of ubiquitous and transparent coverage. Furthermore, the wide-area mobile network access paradigm offers a number of other advantages over local-area distributed approaches, such as higher efficiency, robustness and security, thanks to locally coordinated control, coordinated infrastructure deployment, ease of planning, performance predictability and the possibility of deploying advanced MTC-tailored PHY/MAC schemes that shift complexity from MTDs to base stations (BSs).

The MTC paradigm is hence expected to play a significant role in current and future cellular networks, both as the enabler of potentially disruptive markets (e.g., Smart Cities [54]) and for the new challenges that M2M services will pose to the communication systems. Indeed, today's standards are designed to provide access to a relatively small number of devices that need to transfer a significant amount of data, so that the signaling traffic generated by the management and control plane is basically negligible. M2M services, instead, are generally expected to involve a huge number of devices that generate sporadic transmissions of short packets. The risk is then a collapse of current wireless cellular systems under the weight of the signaling traffic generated by MTDs [55]. In addition, although transmissions from MTDs are, in many cases, delay tolerant (smart metering, telemetry), there is also an important class of M2M applications that require ultra-low latency (e-health, vehicular communications). Furthermore, most MTDs are expected to be severely constrained in terms of computational capabilities, storage and energy capacity. Thus, they require the development of transmission protocols with minimal power consumption.

7.1 M2M Challenges

For all these reasons, the M2M scenario is considered a major challenge for next generation wireless cellular systems, commonly referred to as 5G [78]. In addition to increased energy efficiency of the terminals and of the whole system, 5G will hence be required to provide minimal latency to critical services and seamless integration of IoT nodes, and to support massive M2M communication services, all without degrading the quality of conventional services like voice, audio/video streaming, and web browsing. The interested reader is referred to [7] to have a more thorough description of such issues. Here we just report a list of the main solutions proposed so far by the scientific community to address them. Tab. 7.1, in particular, offers a compound view of such solutions with an indication of the characterizing features and the main targeted performance indices. More specifically, we consider the following aspects:

- **3GPP**: the scheme has been proposed in 3GPP technical report and is designed with explicit reference to 3GPP standards (LTE in particular);
- **Performance indices**: the scheme is designed to improve the following

figures of merit

- minimization of *access delay*;
- minimization of *energy consumption* of MTDs;
- maximization of *access probability/throughput* of UEs and/or MTDs.

Solution	**3GPP**	**Performance indices**		
		Delay	*Energy Efficiency*	*Access Prob.*
Resource Separation [56]	✓			✓
Slotted Access [56]	✓			✓
Pull-based Scheme [56]	✓	✓		✓
Backoff Tuning [56]	✓			✓
Access Class Barring [56]	✓	✓		
SOOC [57]		✓		✓
RA for Fixed-Location [58]		✓		✓
Bulk Signalling [59]			✓	✓
Q-learning [60]		✓		✓
Game Theory Scheme [61]			✓	✓
Energy-efficient clustering [62, 63]			✓	
QoS-based clustering [64–66]		✓		
M2M-Aware Scheduling [67]		✓		✓
Matching Theory Scheme [68]				✓
Reinforcement Learning [69]		✓		✓
Physical Layer Design [70–73]	✓		✓	✓
Cooperative Coverage Extension [74]			✓	
Clean Slate Approaches [75–77]				✓

Note: *Delay* is intended as the time from the first transmission attempt until the successful conclusion of the access procedure.

Table 7.1: Comparison of the proposed approaches to support M2M Communications.

With this in mind, Ch. 8 will be dedicated to the analysis of energy-efficiency in M2M Communications. Specifically, we will provide a theoretical analysis of the optimal protocols and the corresponding performance achievable when varying the capabilities of the Base Station (BS) in terms of both complexity and accuracy on the Channel State Information (CSI).

Nonetheless, a quick look at Tab. 7.1 shows how much attention has been devoted to the massive access problem. Indeed, the IoT paradigm envisions the integration of billions of sensors and actuators into physical objects and their interconnection via wireless links. Since such a huge number of terminals may lead to an enormous number of simultaneous accesses, researchers concern is often on resolving contention among devices. This scenario calls for novel solutions, whose design, in turn, requires a deep and solid comprehension of the fundamental properties and characteristics of the M2M communication paradigm. In this respect, studies that adopt a clean-slate and standard-agnostic approach can provide insights on the basic aspects of M2M communication, thus shedding light on the fundamental performance limits of these types of systems.

Motivated by these considerations, in Ch. 9 we will depart from the centrally coordinated access mechanisms adopted by most of today's wireless cellular systems to show the potential of uncoordinated access schemes based on Multi-Packet Reception (MPR) and Successive Interference Cancellation (SIC) in this context. Finally, in Ch. 10 we wrap up the work providing some final remarks.

8

Energy-efficiency in M2M Communications

As anticipated in Ch. 7, a critical issue in the M2M context is energy saving. Indeed, the energy sources for machine-type devices may be costly to replace or recharge frequently. Just to give an idea, a specific class of MTDs, e.g. devices for landslide monitoring, is developed with the aim of collecting sensory data in remote or impervious areas. Such condition makes their battery replacement very hard and, consequently, calls for extremely long battery duration, in the order of months or even years. Furthermore, machine-type communication (MTC) often has timing constraints in the form of end-to-end deadlines. As an example, surveillance may require alarm reports within few seconds, while vehicle-to-road unit communication may have even stricter latency constraints.

Motivated by these considerations, in this work we investigate the energy efficiency of uplink machine-type transmissions with timing constraints. Although short-range air interfaces such as Zigbee, Bluetooth, or WiFi could be used, according to the considerations made in Ch. 7, we consider wide-area applications, such as mobile sensing, which rely on the cellular infrastructure. Whereas most other studies on energy efficiency consider only the transmit energy related to the power amplifier, in this work, we use an energy model that also accounts for the so-called *circuit energy*, i.e., the rate-independent energy consumption of the board, which has non-negligible impact on the transmission policy in certain scenarios [79], such as the typically low-bitrate IoT communications. We assume that transmission occurs over up to N time slots of duration T seconds (such that NT seconds is the maximum latency), and that a circuit energy cost is incurred whenever a nonzero amplifier energy is applied in a slot to transmit information. For a given packet payload size, given the assumption of channel state knowledge

and under a maximum outage probability constraint, we derive the strategy for allocating energy across one or more time slots to minimize the average total amplifier and circuit energy.

We consider a block fading channel model where we assume that the channel state for each of the N time slots is independently drawn from the same Rayleigh distribution. The channel state is assumed to be known at the receiver, and we consider scenarios with three different levels of channel state information (CSI) at the transmitter:

1. **Full CSI.** The transmitting device has full, ideal, non-causal knowledge of the CSI (complex amplitude of a frequency non-selective channel). The knowledge is non-causal in the sense that the CSI is known over all N time slots, and energy could be allocated over any subset of these time slots. This assumption is not realistic in practice, but the resulting performance provides an optimistic bound on the achievable energy performance. In the remainder we will denote this scenario as *fullCSI*.

2. **Local CSI.** The transmitting device has ideal knowledge of the CSI in the current time slot. It then decides how to allocate energy over this time slot based on the number of bits it still has to transmit. A data packet is hence transmitted over multiple independently encoded subpackets. In practice, this scenario could be implemented in a time-division duplexed system or in a frequency-division duplexed (FDD) system where the channel is estimated by the base and a resource allocation message is sent to the device. We will label this scenario as *localCSI*.

3. **Average CSI.** The transmitting device has knowledge of only the average channel but not the Rayleigh fading realization. In practice, this scenario could be implemented in an FDD system by having the device listen to the downlink broadcast channel. Hereafter, we will use *avgCSI* to refer to this scenario.

At first we will assume that the transmitters can perform both modulation rate and transmit power adaptation from slot to slot to minimize the total energy consumption. Afterward, we simplify the transmitter potentialities in order to get closer to a low complexity M2M-like device. With this intent, we will remove

the power adjustment capability and assume that the device can transmit only with constant power over the allocated resources.

After deriving the resource and power allocation strategies corresponding to each of the above scenarios, we compare their performance using a numerical analysis in the context of an uplink macrocellular network for short packet transmission.

8.1 Related Work

Similar studies have been proposed in the literature but, to the best of our knowledge, they miss one or more of the specific characteristics of the current work. A study on energy-efficient scheduling for M2M communication is reported in [80], where the circuit energy cost and outage are neglected. Similarly, the work in [81] addresses energy efficiency issues for time division multiple access over fading channels with finite-rate feedback, but again without taking into account the overhead due to the circuit energy. In [82], the energy efficient transmission and bit allocation schemes are investigated in multi-source single-sink wireless sensor networks. In contrast to our system model, Rayleigh fading and circuit energy are both neglected. An algorithm known as MoveRight is derived in [83] to solve general energy-minimization scheduling problems. However, the algorithm assumes that the energy for each device is monotonically decreasing with the number of allocated resources, an assumption that no longer holds when considering the circuit energy cost.

We point out that our proposed algorithms are optimal and, thus, they represent the best achievable target for their respective scenarios. However, a clarification is dutiful concerning the localCSI case, for which we will describe the optimal policy and then also propose a strategy that, although suboptimal, requires simpler computations while leading to very similar results. Such narrow gap between the two policies justifies the usage of the latter policy. Our analysis aims at investigating the impact of the channel knowledge, power control and circuit energy on the maximum achievable energy efficiency for time-division scheduling schemes. A comparison with other resource management schemes proposed in the literature is hence out of the scope of this work, though it can be interesting to assess the gap to the optimal performance figures.

The remainder of the chapter is organized as follows. In Sec. 8.2 we illustrate the general system specifications with particular emphasis for the considered energy model. Furthermore, the section will formally state the optimization problem addressed in the work. The core part of the dissertation will be devoted to the description of the solution of the problem when varying the assumptions on the available channel information and the complexity of the transmitter/receiver. Then, in Sec. 8.7 we will collect and compare the corresponding results and, finally, Sec. 8.8 concludes the dissertation with some final remarks.

8.2 System model

We start by considering a single wireless communication link between a transmitter and a receiver. Time is partitioned into slots of duration T seconds each. The transmitter hopes to communicate a payload of L bits within N slots, corresponding to a maximum latency $T_{max} = NT$ seconds, as determined by the application. We assume a fixed bandwidth W Hertz for each slot and denote with N_0 the power spectral density of the AWGN at the receiver.

8.2.1 Channel model

We assume that the channel gain experienced by the user in each slot is affected by independent Rayleigh fading, so that the channel gain in any resource n is an independent exponential random variable g_n with mean $\bar{g}$, which depends on the user's distance from the base station (BS) according to the considered path loss model. Thus

$$\Pr[g_n \leq x] = 1 - e^{-\frac{x}{\bar{g}}}, \quad x \geq 0. \tag{8.1}$$

For the sake of simplicity, we assume that the number of bits that can be reliably transmitted in a given slot n with channel gain g_n and transmit power $P_n^{(tx)}$ is equal to the Shannon bound, i.e.,[1]

$$\rho_n = TW \log_2(1 + g_n P_n^{(tx)}/(N_0 W)), \tag{8.2}$$

[1]The SNR $\Gamma_n = g_n P_n^{(tx)}/N_0 W$ could be scaled by a proper margin factor to account for the gap between the spectral efficiency of practical modulation schemes and the Shannon bound. Nonetheless, for the sake of simplicity and without loss of generality of the model, here we neglect this constant term.

and the transmit power required to deliver ρ_n bits is

$$P_n^{(tx)} = f(\rho_n, g_n) = \frac{(2^{\rho_n/(TW)} - 1)N_0 W}{g_n}\,. \tag{8.3}$$

Note that, if the number of bits transmitted by the user in slot n exceeds ρ_n, we assume that the received packets contains unrecoverable errors. We say that the user experiences *outage* if it does not transmit all the L bits within the N available slots, irrespective of whether the transmission has failed or has not been performed in order to save energy.

8.2.2 Energy model

Since we are interested in comparing different transmission strategies in terms of energy efficiency, we neglect all the energy terms that do not depend on the adopted transmission strategy (e.g., battery leakages). Instead, for each transmission resource we account for the energy related to the over-the-air transmitted power, i.e., $\mathcal{E}_n^{(tx)} = P_n^{(tx)} T$, where $P_n^{(tx)}$ is given in (8.3), and an additional energy term, called *circuit energy* and denoted by $\mathcal{E}^{(c)}$, which accounts for the energy consumed by the device for other operations (e.g., stay active, synchronization, and so on). We assume that the circuit energy is actually spent only when the node transmits in a certain slot.

As a result, the overall energy consumed by the device to transmit a packet within N slots can be expressed as

$$\mathcal{E}^{(tot)} = \sum_{n=1}^{N} \left(P_n^{(tx)} T + \mathcal{E}^{(c)} \chi \left\{ P_n^{(tx)} \right\} \right), \tag{8.4}$$

where $\chi\{x\} = 1$ if $x > 0$ and zero otherwise.

8.2.3 Problem statement

Given N slots that can be used to deliver a packet of L bits to the BS, and assuming that these bits can be arbitrarily divided among the N resources, we want to find the best power allocation per slot such that the user can deliver the packet with an overall outage probability lower than ϵ, while minimizing the

expectation of the total aggregate energy cost given by (8.4). Mathematically:

$$\begin{aligned} &\min_{\{N,P_n^{(tx)}\geq 0\}} \mathrm{E}\left[\sum_{n=1}^{N}\left(P_n^{(tx)}T+\mathcal{E}^{(c)}\chi\left\{P_n^{(tx)}\right\}\right)\right] \\ &\text{subject to: } \Pr[\text{outage}]=\Pr\left[\sum_{n=1}^{N}\rho_n<L\right]\leq\epsilon\,, \end{aligned} \tag{8.5}$$

where the statistical nature of the result is due to the Rayliegh fading across the N slots. In the following three sections we derive the solutions of the problem (8.5) in various scenarios that differ for the CSI available at the transmitter. A common assumption for these cases, instead, is that the devices are able to perform power adaptation through the slots.

8.3 Optimal power allocation with full CSI

We start by assuming that the scheduler knows in advance the channel gains $g_n,\ n=1,\ldots,N$, in all the N available slots, a scenario that we dub fullCSI. The reader can think that this information is provided by the BS to the users through channel state estimation procedures. The performance achievable under this rather idealistic assumption will provide an upper bound that will be used as benchmark to compare the performance loss incurred when considering more realistic scenarios. Knowing the channel realization, the device can adapt both the transmit power and the modulation rate in each slot in order to deliver all the bits in the allotted time, with minimum energy consumption.

We observe that the allocation problem closely resembles the classical power allocation problem in parallel Gaussian channels, where the objective is to maximize the aggregate throughput under a constraint on the total transmit power. In this case, the optimal solution is provided by the *water filling* strategy [84], which assigns powers to the different users according to the reciprocal of their channel gains. Our problem, however, departs from the classic one in three aspects: first, we wish to minimize the aggregate energy cost under a constraint on the total number of bits to be transmitted over a given number of resources; second, we have to account for a penalty (the circuit energy) any time we decide to use one such resource; third, we admit that a fraction of the packets equal to the outage probability ϵ can be directly dropped at the source to save energy if the channel is particularly harsh.

To solve our problem, we propose a multi-stage approach the leads to the optimal solution for (8.5). First, we apply the water-filling algorithm to find the optimal power allocation to transmit L bits in no more than N slots for a given channel realization vector $\mathbf{g^{(N)}} = [g_1, \ldots, g_N]$, with zero outage probability. This solution does not consider the circuit energy. We then add the circuit energy cost and find the total energy cost $\mathcal{E}^{(tot)}(N)$, given by (8.4). Note that the circuit energy is considered only for the slots with positive power allocation. We then recursively remove the slots with lower channel gain and solve the energy allocation problem again, with a reduced number of slots, until we find the M^* slots for which $\mathcal{E}^{(tot)}(M^*)$ is minimized. We remark that M^* and $\mathcal{E}^{(tot)}(M^*)$ depend on the channel realization vector $\mathbf{g^{(N)}}$ and, hence, may vary at each packet transmission. We then determine the probability distribution of $\mathcal{E}^{(tot)}(M^*)$ and find the threshold $\mathcal{E}_{thr}$ such that $\Pr\left[\mathcal{E}^{(tot)}(M^*) > \mathcal{E}_{thr}\right] = \epsilon$. The optimal transmission policy, finally, consists in computing the M^* and $\mathcal{E}^{(tot)}(M^*)$ for the given $\mathbf{g^{(N)}}$ and to allocate the power to the M^* slots as dictated by the water filling algorithm if $\mathcal{E}^{(tot)}(M^*) \leq \mathcal{E}_{thr}$, and do not allocate any power (i.e., avoid the transmission of the packet) if $\mathcal{E}^{(tot)}(M^*) > \mathcal{E}_{thr}$.

In the following we detail this algorithm step by step. Successively, we discuss the optimality of the policy.

Step 1 (solving the water filling problem)

Without loss of generality, we assume that the resources are numbered in decreasing order of channel gain, so that $g_1 \geq g_2 \geq \ldots \geq g_N$. As a first step, we determine the optimal power allocation over the N slots, with channel gain vector $\mathbf{g^{(N)}} = [g_1, \ldots, g_N]$ without considering the circuit energy.

To find the optimal solution, we map the problem into the classical sum-capacity maximization problem in parallel Gaussian channels, with total power constraint, which can be formulated as follows:

$$\max_{\substack{\left\{P_n^{(tx)}\right\} \\ \sum_{n=1}^{N} P_n^{(tx)} \leq P_t}} \quad C = W \sum_{n=1}^{N} \log_2 \left(1 + \frac{P_n^{(tx)} g_n}{N_0 W}\right), \tag{8.6}$$

where P_t is the total power constraint and C denotes the aggregate bitrate obtained from the N slots with channel gain vector $\mathbf{g^{(N)}}$. The optimal power allocation is provided by the water filling algorithm, which assigns to the nth slot

the power

$$P_n^{(tx)^*} = \left[\nu - \frac{N_0 W}{g_n}\right]^+ \tag{8.7}$$

where $[x]^+ = \max(0, x)$ and ν is the "water level" that, in the classical water-filling solution, is computed so as to respect the total power constraint, i.e., $\sum_{n=1}^{N} P_n^{(tx)^*} = P_t$. In our formulation of the problem, the goal is to minimize P_t and the constraint is on the sum capacity, which shall be equal to L/T. Therefore, we need to find ν such that $C = L/T$, which yields

$$\nu = N_0 W \sqrt[\mathcal{M}]{\frac{2^{L/(WT)}}{\prod_{n=1}^{\mathcal{M}} g_n}}, \tag{8.8}$$

where $\mathcal{M} = \sum_{n=1}^{N} \chi\left[P_n^{(tx)^*}\right]$ is the total number of slots with non-zero power allocation.

Note that, according to the water-filling algorithm, the power assigned to a certain slot cannot be larger than the power allocated to another slot with better channel gain. Therefore, if slot n is assigned zero power, then all other slots k with $g_k \leq g_n$ will also be unused for transmission. Consequently, the optimal power allocation can be reached by considering the subset of the $\mathcal{M}$ slots with higher channel gain, i.e., solving the problem for the reduced channel vector $\mathbf{g}^{(\mathcal{M})} = [g_1, \ldots, g_{\mathcal{M}}]$. It is easy to realize that, further reducing the set of available slots, i.e., by limiting the set of available slots to the best $M \leq \mathcal{M}$ with a channel vector $\mathbf{g}^{(\mathbf{M})} = [g_1, \ldots, g_M]$, the water-filling algorithm will allocate positive power to all the M slots, yielding a total transmit power

$$\mathcal{E}^{(tx)}(M) = \sum_{n=1}^{\mathcal{M}} P_n^{(tx)^*} T \tag{8.9}$$

which is non-increasing with M, and reaches its minimum for $M \geq \mathcal{M}$. We can then limit our attention to the subset of $\mathcal{M}$ slots with channel gain vector $\mathbf{g}^{(\mathcal{M})}$.

Step 2 (adding the circuit energy term)

Assuming that we restrict the solution to the $M \leq \mathcal{M}$ best slots, the overall energy consumption will be given by

$$\mathcal{E}^{(tot)}(M) = \mathcal{E}^{(tx)}(M) + M\mathcal{E}^{(c)}\,. \tag{8.10}$$

Since, for any given $\mathbf{g}^{(\mathbf{N})}$, the function $\mathcal{E}^{(tx)}(M)$ is non-increasing in M, while $M\mathcal{E}^{(c)}$ is linearly increasing in M, the total energy $\mathcal{E}^{(tot)}(M)$ will be minimized for $M = M^*$, where

$$M^* = \max\left\{M \leq \mathcal{M} : \mathcal{E}^{(tx)}(M) - \mathcal{E}^{(tx)}(M+1) \geq \mathcal{E}^{(c)}\right\} .$$

As an example, we report in Fig. 8.1 the total energy when varying M, for a toy example with $N = 100$, $L = 500$ bits, $\bar{g} = 10^{-11}$, $W = 50$ kHz, $T = 1$ ms, $N_0 = -164$ dBm, and considering three values for $\mathcal{E}^{(c)}$.

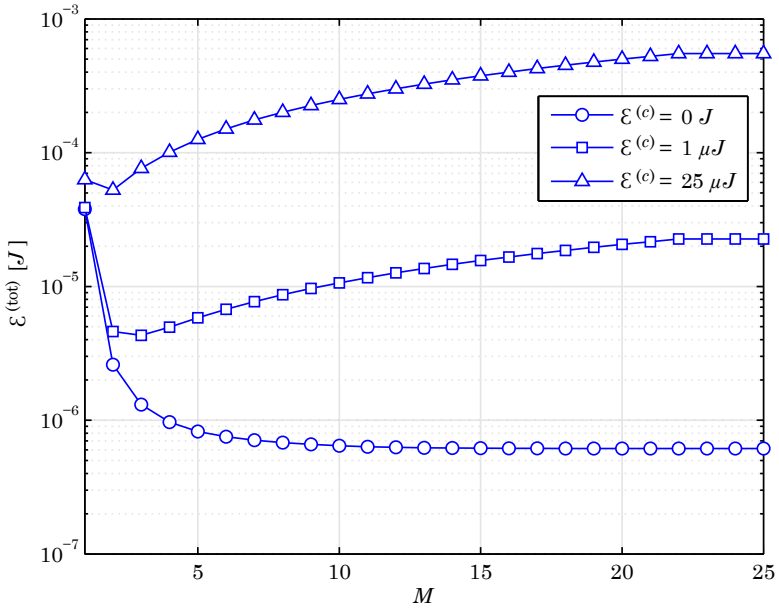

Figure 8.1: Total energy cost as a function of M when the circuit cost changes for the fullCSI case.

Observe that with zero circuit energy, we have $M^* = \mathcal{M}$, while for larger circuit energy costs the optimal number of slots M^* to be used decreases.

Step 3 (introducing outage condition)

The power allocation obtained in Step 2 minimizes the total energy under the assumption that the outage probability is zero. If we admit a certain outage probability $\epsilon > 0$, it is possible to save energy by skipping the transmission of a fraction ϵ of the packets. Clearly, to maximize the energy saving, it is convenient

to discard the packets whose transmission will incur higher energy cost. We hence compute the distribution of the overall energy consumption $\mathcal{E}^{(tot)}(M^*)$ and find the threshold $\mathcal{E}_{thr}$ such that $\Pr\left[\mathcal{E}^{(tot)}(M^*) > \mathcal{E}_{thr}\right] = \epsilon$. An example of the cdf of the total energy cost is provided in Fig. 8.2 along with the outage threshold. The optimal policy is to avoid transmission, i.e. incur in outage, any time the channel realization $\mathbf{g}^{(\mathbf{N})}$ is such that the corresponding optimal $E^{(tot)}(M^*)$ is larger than $\mathcal{E}_{thr}$. In this way, all transmissions that would cost more than $\mathcal{E}_{thr}$ are dropped to save energy.

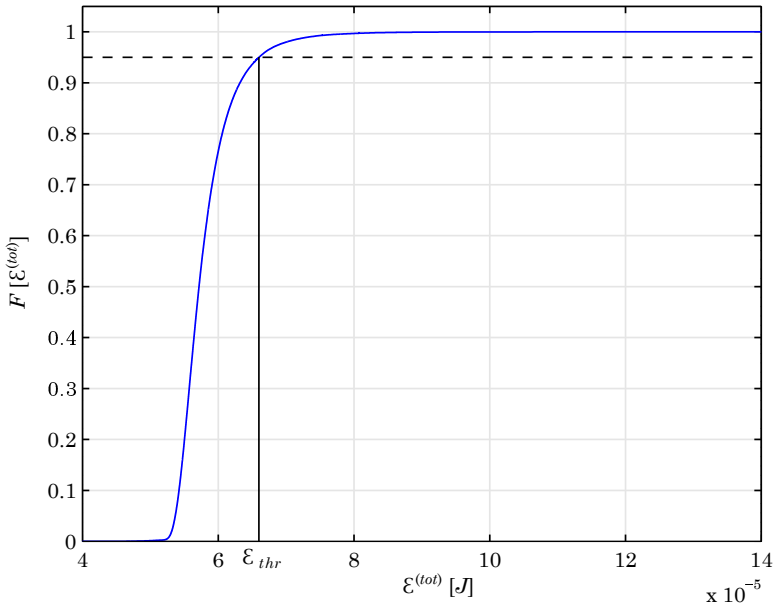

Figure 8.2: Cdf of the total energy cost under fullCSI assumption.

Unfortunately, deriving the exact statistical distribution of $\mathcal{E}^{(tot)}(M^*)$ is a formidable task. We hence resort to an approximate method that, rather than considering the statistical distribution of $\mathcal{E}^{(tot)}(M^*)$, which depends on the random vector $\mathbf{g}^{(\mathbf{N})}$, only considers the distribution of the sum of the channel gains, $G = \sum_{i=1}^{N} g_i$. The rationale is that the energy consumption is strictly correlated with the average channel gain and, in turn, to G. Under the assumption of independent Rayleigh fading, G is distributed as an Erlang random variable with shape parameter N and rate $\bar{g} = \mathrm{E}[g_n]$, whose cumulative distribution function is given by $F_G(x) = \frac{\gamma(N, x/\bar{g})}{(N-1)!}$ where $\gamma(\cdot)$ is the incomplete gamma function. We then find the threshold G^* such that $F_G(G^*) = \epsilon$ and avoid transmission any

time $G \leq G^*$. Although this criterion is suboptimal, it turns out to provide very good results. As an example, in Fig. 8.3 we report the average energy obtained by using the exact and approximate packet-discarding criterion in a simulation scenario with cell-edge user (parameters are in Tab. 8.1). As we can see, the two curves are almost perfectly overlapping.

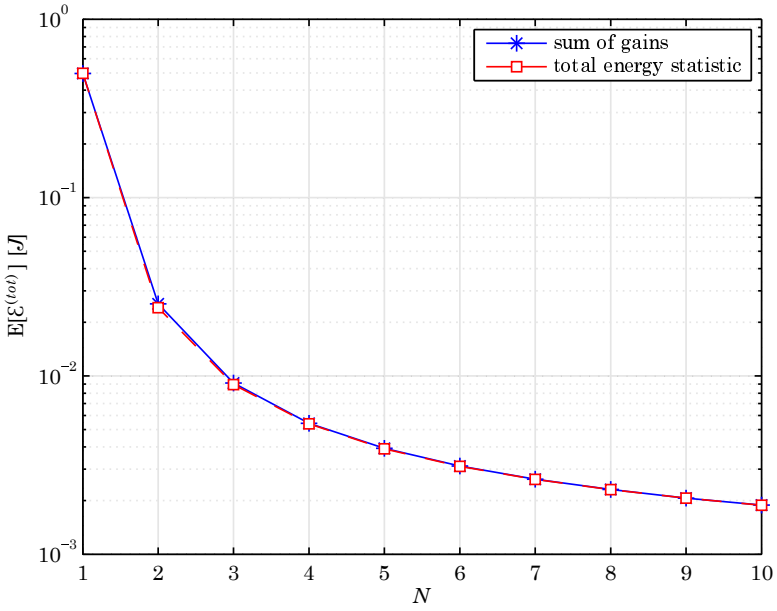

Figure 8.3: Average energy cost in the fullCSI scenario with different packet discarding policies.

8.3.1 An intuitive discussion about the policy optimality

We observe that the allocation obtained by the described policy (with the exact packet-discarding criterion) is optimal, in the sense that it minimizes (8.10) while guaranteeing an outage probability not larger than ϵ. This property follows from the optimality of the solutions obtained at each step for the related subproblem. Indeed, the water filling algorithm provides the power allocation that minimizes the transmission power, given a certain set of slots. When adding the circuit energy, we then choose the set of slots that provide the best tradeoff between circuit and transmission energy costs. Finally, avoiding transmission for the fraction ϵ of packets that would incur in the highest energy cost is the best strategy to save

energy while guaranteeing an outage probability ϵ.

8.4 Power allocation with local CSI

In this section we assume to know the long-term average channel gain $\bar{g}$ and the channel state of only the current slot n. The goal is to determine, in each slot, the transmit strategy for the current slot, given that there are $N - n$ remaining slots. The policy must specify how many bits to transmit in the current slot and with what power. These choices have to be based on the channel gain in the current slot and the expected energy cost to complete the transmission in the remaining slots. Its optimal solution (cf App. B.2), however, is quite involved and particularly demanding in terms of numerical elaboration. Therefore, here we will propose a simpler sub-optimal solution that, yet, turns out to be very close to the optimum one.

Specifically, we formulate the localCSI problem as a finite-horizon Markov Decision Problem which can be solved applying the well-known dynamic programming approach [85]. Let then $x_n \in S$ denote the system state in slot n, with $n = 1, 2, \ldots, N$, where S is the state space that collects all states $x = (\ell, g)$ being $\ell \in \mathbb{N}$ the number of pending bits before the current slot and $g \in \mathbb{R}^+$ the current channel gain.

The decision rule in slot n is a function that maps the system state to an admissible action b_n which, in our case, corresponds to the number of bits to be transmitted in the current slot. Thus, from the state $x_n = (\ell_n, g_n)$ in slot n, the admissible actions are $b_n \in \{0, 1, \ldots, \ell_n\}$.

Now, let $U_n(\ell_n)$ denote the average energy cost incurred in slots from n to N, starting from state $x_n = (\ell_n, g_n)$, and applying the optimal policy in the slots from n to N. Clearly, $U_n(\ell_n) = 0$ for $\ell_n \leq 0$. If the state in the last available slot is $x_N = (\ell_N, g_N)$, with $\ell_N > 0$, the required power to complete the transmission is $f(\ell_N, g_N)$, where $f(\cdot, \cdot)$ is as in (8.3). However, if the channel is particularly harsh, the transmission should be avoided to save energy. The channel gain g_o below which transmission is aborted at the last slot[2] is determined by the outage probability ϵ. Specifically, in order to guarantee that the overall outage is lower

[2]Note that assumption leads to a sub-optimal policy. Indeed, such threshold should depend on the number of pending bits at the beginning of the slot, as illustrated in App. B.2.

than ϵ, it must hold

$$\begin{aligned}&\Pr\left[\text{outage}\right] = 1 \cdot \Pr\left[g_N \leq g_o, \ell_N \neq 0\right] = \Pr\left[g_N \leq g_o\right] \cdot \Pr\left[\ell_N \neq 0\right] \\ &= 1 - e^{g_o/\bar{g}}(1 - \Pr\left[\ell_N = 0\right]) \leq \epsilon\end{aligned} \tag{8.11}$$

where the first equality comes from the fact that transmissions that has already been completed before the last slot (i.e., that have no pending bits in the N-th slot) cannot be in outage while the second equality exploits the independence of the two events $g_N \leq g_o$ and $\ell_N \neq 0$. Thus, from (8.11) it results

$$g_o = -\bar{g} \ln\left(1 - \frac{\epsilon}{1 - \Pr\left[\ell_N = 0\right]}\right) . \tag{8.12}$$

where, for ease of notation, we define $\hat{\epsilon} = \frac{\epsilon}{1-\Pr\left[\ell_N=0\right]}$. The average energy spent in the last slot, given that ℓ_N bits have to be transmitted, is hence given by

$$\begin{aligned}U_N(\ell_N) &= \int_{g_o}^{\infty} \left[\mathcal{E}^{(c)} + \frac{\left(2^{\frac{\ell_N}{TW}} - 1\right) N_0 WT}{y}\right] \frac{e^{-\frac{y}{\bar{g}}}}{\bar{g}} dy \\ &= \mathcal{E}^{(c)}\left(1 - \hat{\epsilon}\right) + \frac{\left(2^{\frac{\ell_N}{TW}} - 1\right) N_0 WT}{\bar{g}} \mathrm{Ei}\left(-\ln\left(1 - \hat{\epsilon}\right)\right) ,\end{aligned} \tag{8.13}$$

where $\mathrm{Ei}(a) = \int_a^{\infty} y^{-1} \exp(-y) dy$ is the exponential integral function.

The optimal transmit policy can then be obtained by finding the best action in any slot n, in reverse order. Assuming the state in slot $n < N$ is $x_n = (\ell_n, g_n)$, with $\ell_n > 0$, an action b_n will yield an energy cost equal to the sum of the energy required to send b_n bits with the current channel gain and the expected energy to transmit the remaining bits in the following slots:

$$u_n(b_n; \ell_n, g_n) = \mathcal{E}^{(c)} \chi\left\{b_n\right\} + f(b_N, g_N) T + U_{n+1}(\ell_n - b_n) . \tag{8.14}$$

Note that, for $b_n = 0$, no energy will be spent in slot n.

The optimal action rule $\pi_n(\ell_n, g_n)$ in slot n consists in the transmission of the number of bits that minimizes (8.14):

$$\pi_n(\ell_n, g_n) = \arg \min_{0 \leq b_n \leq \ell_n} \left\{u_n(b_n; \ell_n, g_n)\right\} \tag{8.15}$$

which can be found recursively, as a function of n, proceeding backwards in time from N to 1 by noting that:

$$U_{n+1}(\ell) = \mathrm{E}\left[u_{n+1}(\pi_{n+1}(\ell, g_{n+1}); \ell, g_{n+1})\right] . \tag{8.16}$$

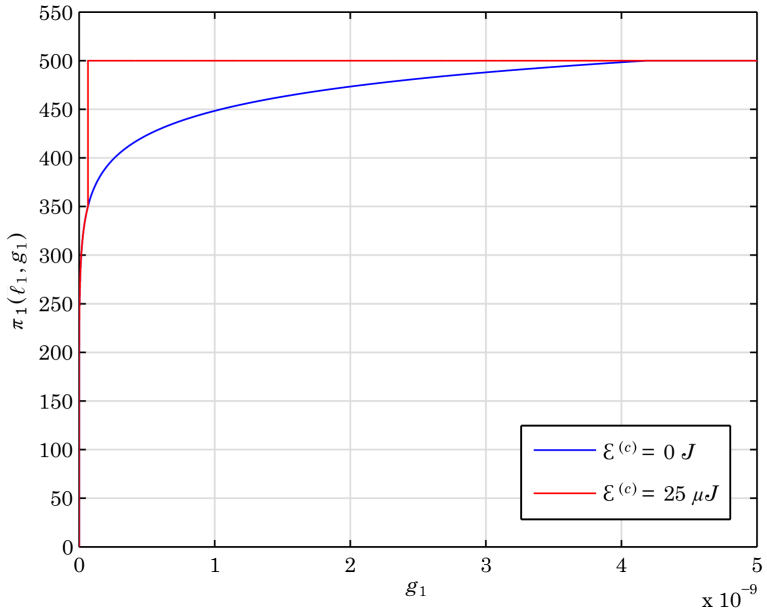

(a) $N = 2$

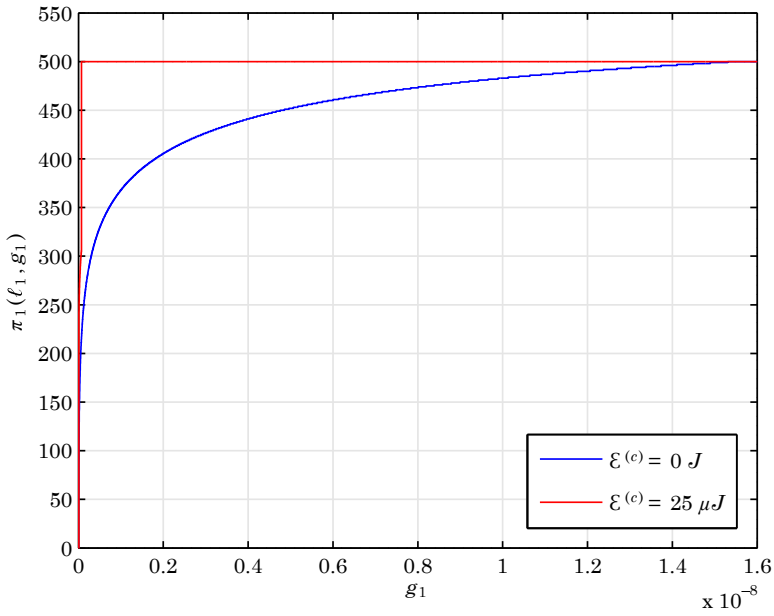

(b) $N = 8$

Figure 8.4: Optimal bit allocation strategy as a function of the channel gain for different time horizons and circuit energy costs in the localCSI case.

Finally, we can easily find the transmit power associated to slot n by substituting (8.15) in place of ρ_n in (8.3).

It is worthwhile to note how the best strategy $\pi_n(\ell_n, g_n)$ depends on both the time horizon $N-n$ and the circuit cost $\mathcal{E}^{(c)}$. To this end, we report the graphs of Fig. 8.4 where we collect the results given by (8.15) for two different values of $N-n$. Also, for each of them, we plot the curves obtained when imposing two different values of $\mathcal{E}^{(c)}$. The other parameters, identical for all configurations, are the following: $\ell_n = 500$ bits, $\epsilon = 0.05$ and $\bar{g} = 10^{-11}$.

Concerning the time horizon, the graphs show that, in general, as $N-n$ decreases the optimal policy becomes more "aggressive," i.e., keeping the channel gain and the circuit energy fixed, we send more bits. This trend is explained by noting that when $N-n$ increases we have more slots ahead left for usage. Thus, it is more likely to find later resources with very good channel quality and the system is led to be more conservative in terms of bits delivered in the current slot.

Coming to the contribution given by the circuit energy, we realize that it acts on the thresholds corresponding to zero bit loading and full bit loading. In particular, as $\mathcal{E}^{(c)}$ grows, the critical gain value below which the optimal strategy is to remain silent ($\pi_n(\ell_n, g_n) = 0$) moves to the right while the threshold above which the device forwards all the pending bits in the current resource ($\pi_n(\ell_n, g_n) = \ell_n$) moves to the left. This tendency originates from the fact that, for larger values of $\mathcal{E}^{(c)}$, the penalty associated to the usage of a slot increases. Therefore, the user either avoids transmission not to incur in the circuit overhead in the current slot or it forwards all its bits immediately so that he will not pay the circuit energy cost in the next slots. Accordingly, the interval of g_n for which the optimal policy corresponds to the delivery of an intermediate number of bits $0 < \pi_n(\ell_n, g_n) < \ell_n$ will progressively reduce with $\mathcal{E}^{(c)}$. Also, this behavior is stressed more and more as $N-n$ increases.

8.5 Optimal power allocation with average CSI

For the third CSI scenario, we assume that only the average channel gain $\bar{g}$ of the Rayleigh distribution is known. Since the channel state realizations are unknown, the coding, modulation, and allocated power in each slot needs to

be determined *a priori*. Starting from the original problem statement (8.5), we derive the following:

$$\begin{aligned}
&\begin{cases} \min_{\{P_n^{(tx)}\geq 0\}} \mathrm{E}\left[\sum_{n=1}^{N}\left(P_n^{(tx)}T + \mathcal{E}^{(c)}\chi\left\{P_n^{(tx)}\right\}\right)\right] \\ \text{s.t. } \Pr\left[\sum_{n=1}^{N}\rho_n < L\right] \leq \epsilon \end{cases} \\
=&\begin{cases} \min_{\{M\leq N; P_n^{(tx)}\geq 0\}} \mathrm{E}\left[\sum_{n=1}^{M} P_n^{(tx)}T + \mathcal{E}^{(c)}M\right] \\ \text{s.t. } \Pr\left[\sum_{n=1}^{M}\rho_n < L\right] \leq \epsilon \end{cases} \\
=&\begin{cases} \min_{\{M\leq N; P^*\geq 0\}} M\left(P^*T + \mathcal{E}^{(c)}\right) \\ \text{s.t. } \Pr\left[W\sum_{n=1}^{M}\log_2\left(1+\frac{g_nP^*}{N_0W}\right) < \frac{L}{T}\right] = \epsilon \end{cases}
\end{aligned} \tag{8.17}$$

The first equality comes from optimizing over all possible values of $M \leq N$, where M denotes the number of slots we allocate non-zero power. Note that, because the channel gains g_n are identically distributed we can, without loss of generality, assign non-zero energy to the first M slots $\{1, \ldots, M\}$. Note that given M, it is optimal to allocate equal power across the M slots since the distribution of the channel realization is identical across the slots. Also, note that, as the power per slot decreases, the outage probability increases monotonically. Hence the last line of (8.17) follows, where P^* is the power allocated per slot such that the outage probability equals ϵ. Given P^*, we compute the associated total energy consumption $\mathcal{E}^{(tot)} = M\left(P^*T + \mathcal{E}^{(c)}\right)$ and finally determine the optimal number of slots M^* used which minimizes such quantity.

Practically, coding across the different time slots is necessary: the packet is encoded across the M^* slots, and a single code can reliably communicate at rate L/T bps whenever the capacity condition in (8.17) is met [86].

8.6 Optimal resource allocation without power control

In the current section we considered MTDs with reduced complexity by removing their power adaptation capability. Accordingly, a device is bounded to transmit with uniform power over all the allocated resource and cannot adjust it depending on channel variations. Note that the general problem statement given in Sec. 8.2.3 still applies in this context with the only difference that, now, the transmit power in the resources used is constant, i.e. $P_n^{(tx)} = P^{(tx)}$, $\forall n = 1, \ldots, N$. Irrespective

of the other assumptions considered, the solution to this novel scenario develops along the following three steps:

- For a given number N of assigned resource, we compute the minimum constant transmit power per resource $P^{(tx)^*}(N)$ that satisfies the outage condition in (8.5). Note that, for the moment, we do not need to consider the circuit energy since it does not affect the success of the transmission.

- For the above $P^{(tx)^*}(N)$ we compute the average number of resources $\bar{n}(N)$ that are actually used for transmission. Indeed, the power $P^{(tx)^*}(N)$ guarantees that, when N resources are available, the probability that the user is not able to successfully deliver its L bits is less than ϵ. Nonetheless, depending on the specific channel realization, the transmission can be successfully completed before the N-th resource.

- Finally, we add the circuit energy term. Given $P^{(tx)^*}(N)$ and $\bar{n}(N)$ we can rewrite the optimization function in (8.5) as

$$\min_{N} \bar{n}(N) \left[P^{(tx)^*}(N)T + \mathcal{E}^{(c)} \right] \tag{8.18}$$

  and compute the expectation of the total energy cost when varying N. The number of resources $N = M^*$ for which (8.18) is minimized and the associated $P^{(tx)^*}(M^*)$ and $\bar{n}(M^*)$ correspond to the optimal solution of our optimization problem.

8.6.1 Local CSI case

We first consider the localCSI scenario, i.e. we assume that the transmitter knows the long-term average channel gain $\bar{g}$ and the exact channel state of the current slot. We remind that we removed power adaptation at the transmitter so that it uses fixed power within its transmission window and is only able to adapt the modulation rate according to the current channel realization. This case is indicated as *localCSInoPA*.

For the sake of clarity, we will use Fig. 8.5 to characterize the success and outage events in this context. Suppose that a certain user has to send a payload of L bits and the BS assigns him N total resources for the purpose. We remind that the device transmits with fixed power $P^{(tx)}$ in every slot. However, since,

by hypothesis, the transmitter is aware of the exact instantaneous channel gain, it can adjust, from slot to slot, the modulation rate and thus exploit the full capacity of the resource. Accordingly, two cases can occur

- Success: the overall capacity of the N available resources, i.e. $\sum_{n=1}^{N} \rho_n/T = \sum_{n=1}^{N} W \log_2 \left(\frac{g_n P^{(tx)}}{N_0 W} \right)$, is greater than or equal to L/T (see top image in Fig. 8.5). Note that, depending on the channel quality, the transmission might also require less than N slots to be successfully completed.

- Outage: the overall capacity of the N slots when transmitting with power $P^{(tx)}$ is not sufficient to sustain the data size L required by the user (see bottom image in Fig. 8.5).

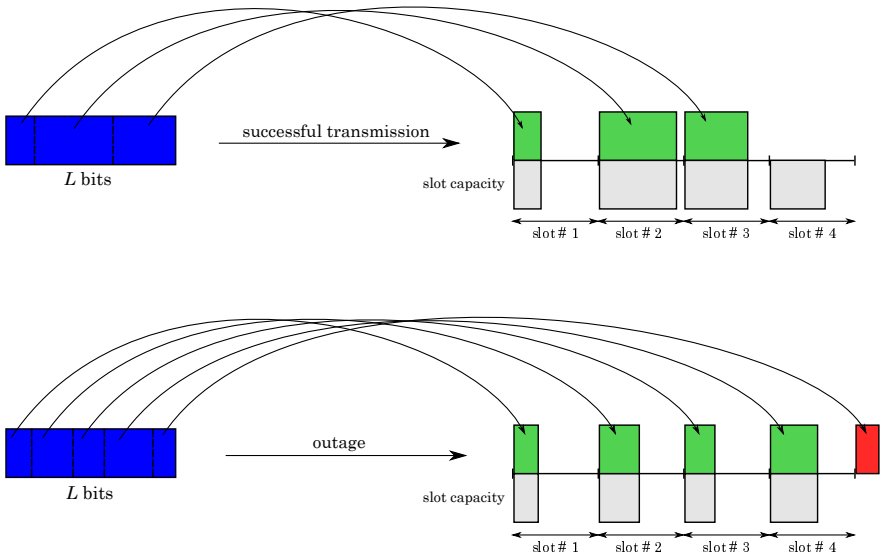

Figure 8.5: Success and outage events in the localCSInoPA scenario.

The optimization problem under such scenario can be expressed as follows

$$P^{(tx)^*} = \min \left\{ P^{(tx)} : \Pr \left[\sum_{n=1}^{N} \rho_n < L \right] \leq \epsilon \right\} . \tag{8.19}$$

Recalling (8.2), the probability on the right-hand side of (8.19) can be rewritten as

$$\Pr \left[\sum_{n=1}^{N} TW \log_2 \left(1 + \frac{g_n P^{(tx)}}{N_0 W} \right) < L \right] . \tag{8.20}$$

Then, given $P^{(tx)^*}$, we need to evaluate the corresponding $\bar{n}$. Let X_i indicate the event that L bits are successfully transmitted within $i \leq N$ resources, while the complementary event (outage) will be denoted as Y_i. We hence have

$$X_i = \left\{ \sum_{n=1}^{i} TW \log_2 \left(1 + \frac{g_n P^{(tx)^*}}{N_0 W} \right) \geq L \right\} . \tag{8.21}$$

Then, the probability mass distribution (pmd) of the number of resources that are actually used by the node can be expressed as

$$g(i) = \begin{cases} \Pr[X_1] & i = 1 ; \\ \Pr[X_i, Y_{i-1}] & i \in \{2, \ldots, N-1\} ; \\ \Pr[Y_{N-1}] & i = N . \end{cases} \tag{8.22}$$

and the average number of used resources is given by

$$\overline{n} = \sum_{i=1}^{N} i \cdot g(i) \tag{8.23}$$

which is a non-decreasing function of N, as proved in App. B.1.

Unfortunately, (8.20) and (8.23) cannot be expressed in closed form. A possible way to overcome this problem is to resort to Monte-Carlo analysis to find them. Another escamotage is to find closed form expressions that well approximate (8.20) when operating in the high- or low-SNR scenarios, as explained next.

Approximation for low SNR

If we assume a low SNR regime, i.e., $\Gamma_n = \frac{g_n P^{(tx)}}{N_0 W} \ll 1$, the following approximation holds

$$\log_2 (1 + \Gamma_n) \simeq \Gamma_n \log_2 e = \frac{g_n P^{(tx)}}{N_0 W} \log_2 e. \tag{8.24}$$

Replacing (8.24) in (8.20), we get

$$\Pr \left[\sum_{n=1}^{N} g_n < \frac{L N_0}{T P^{(tx)} \log_2 e} \right] . \tag{8.25}$$

The sum of N iid exponential random variables with parameter $\bar{g}$, as appears in (8.25), has Erlang distribution of parameters $(N, 1/\bar{g})$, whose cumulative distribution function (cdf) is

$$\mathrm{F}_{Erl}(x; N, 1/\bar{g}) = 1 - \sum_{i=0}^{N-1} \frac{\left(\frac{x}{\bar{g}}\right)^i e^{-x/\bar{g}}}{i!}. \tag{8.26}$$

Using (8.26) and (8.25) into (8.19) we finally get

$$P^{(tx)^*} = \min\left\{P^{(tx)} : \mathrm{F}_{Erl}\left(\frac{LN_0}{TP^{(tx)}\log_2 e}; N, 1/\bar{g}\right) < \epsilon\right\}. \tag{8.27}$$

Considering that the cdf is monotonic, (8.27) can be easily solved with bisection method.

We now need to find $\bar{n}$. In the low SNR regime, we have

$$\begin{aligned}\Pr[X_i] = 1 - \Pr[Y_i] &= \Pr\left[\sum_{n=1}^{i} g_n \geq \frac{LN_0}{TP^{(tx)^*}\log_2 e}\right] \\ &= 1 - \mathrm{F}_{Erl}\left(\frac{LN_0}{TP^{(tx)^*}\log_2 e}; N, 1/\bar{g}\right) = 1 - \mathrm{F}_{Erl}\left(\tilde{L}; N, 1/\bar{g}\right)\end{aligned}$$

where, for ease of notation, we set $\tilde{L} = \frac{LN_0}{TP^{(tx)^*}\log_2 e}$.

The pmd of the number of resources actually used, given by (8.22), can then be computed in closed form (though using the implicit functions $\mathrm{F}_{Erl}(x; i, 1/\bar{g})$). In particular, for $i = 2, \ldots, N-1$, we have

$$g(i) = \Pr\left[X_i, Y_{i-1}\right] = \int_0^{\tilde{L}} \mathrm{f}_{Erl}(x; i-1, 1/\bar{g})\, e^{-\frac{\tilde{L}-x}{\bar{g}}} \mathrm{d}x\,.$$

The value of $\bar{n}$ can finally be obtained as in (8.23), which involves a finite sum of known terms.

Approximation for high SNR

Assuming a high SNR regime, i.e. $\Gamma_n \gg 1$, the following approximation holds

$$\log_2\left(1 + \Gamma_n\right) \simeq \log_2\left(\Gamma_n\right). \tag{8.28}$$

The probability in (8.20) can then be approximated as

$$\Pr\left[\sum_{n=1}^{N} TW \log_2\left(\frac{g_n P^{(tx)}}{N_0 W}\right) < L\right] \tag{8.29}$$

that, replaced in (8.19), yields

$$P^{(tx)^*} = \min\left\{P^{(tx)} : \Pr\left[\prod_{n=1}^{N} g_n < \frac{2^{\frac{L}{TW}}(N_0 W)^N}{{P^{(tx)}}^N}\right] \leq \epsilon\right\}. \tag{8.30}$$

In this case, we have the product of N iid exponential random variables with parameter $1/\bar{g}$, whose non trivial cdf $\mathrm{F}_{PE}(x; N, 1/\bar{g})$ was derived in [87].

Accordingly, (8.30) becomes

$$P^{(tx)^*} = \min\left\{P^{(tx)} : \mathrm{F}_{PE}\left(2^{\frac{L}{TW}}\left(\frac{N_0 W}{P^{(tx)}}\right)^N; N, 1/\bar{g}\right) \leq \epsilon\right\} \tag{8.31}$$

whose solution is obtained by inverting the cdf $\mathrm{F}_{PE}(x; N, 1/\bar{g})$.

To compute $\bar{n}$, we express (8.21) as

$$\begin{aligned}\Pr[X_i] = 1 - \Pr[Y_i] &= \Pr\left[\prod_{n=1}^{i} g_n \geq 2^{\frac{L}{TW}}\left(\frac{N_0 W}{P^{(tx)^*}}\right)^i\right] \\ &= 1 - \mathrm{F}_{PE}\left(2^{\frac{L}{TW}}\left(\frac{N_0 W}{P^{(tx)^*}}\right)^i; i, 1/\bar{g}\right) .\end{aligned}$$

The computation of $\bar{n}$ follows the same rationale used for the low SNR case.

In Fig. 8.6 we compare the exact solution of the localCSInoPA scenario with the approximations obtained in the low and high SNR regimes both for the case of user close to the BS and at cell edge. The corresponding system parameters, which lead to the average total energy consumption of Fig. 8.6, can be found in Tab. 8.1. As expected, the high SNR approximation (HSNR) is much more accurate than the low SNR (LSNR) solution when we consider a user close to the BS. In this case, in fact, the system tends to operate in the high SNR regime because the path loss near the BS is small. Quite surprisingly, a similar result is shown for the user at cell edge, where the high path loss would involve a lower SNR with respect to user near the BS. However, this holds as long as the power used by the users is equal, which is clearly not true in our framework. Indeed, given N and in order to minimize the energy consumption, they will both work at the lowest SNR that keeps the outage below a certain threshold ϵ. Therefore, those who experience a greater path loss are obliged to transmit with higher power, as reflected by the greater energy consumption, to maintain the same SNR. For small values of N, in particular, the actual SNR needed by the system to satisfy (8.20) is high because we have few slots available, which explains the accuracy of the HSNR solution in this case. When we increase N, instead, the transmit power per slot and, equivalently, the SNR can be reduced so that the low SNR assumption becomes progressively more reasonable. For further comments on the results the reader is referred to Sec. 8.7.

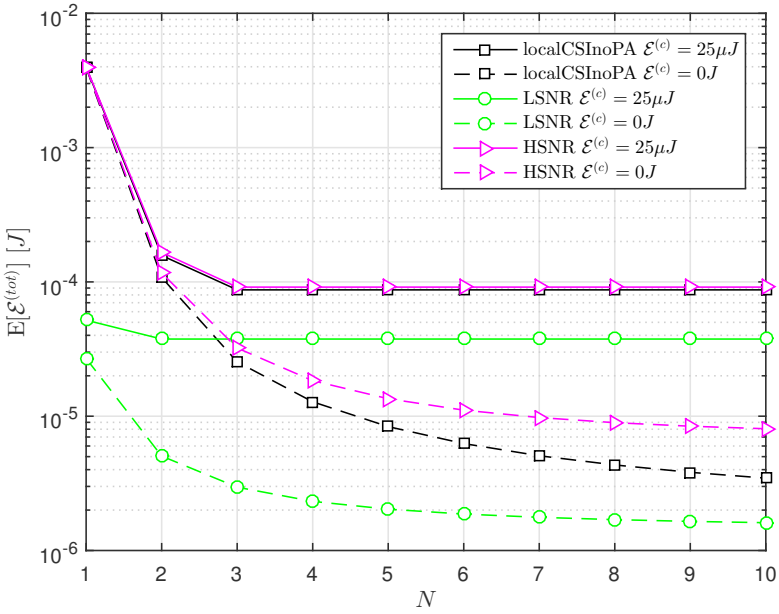

(a) User close to the BS

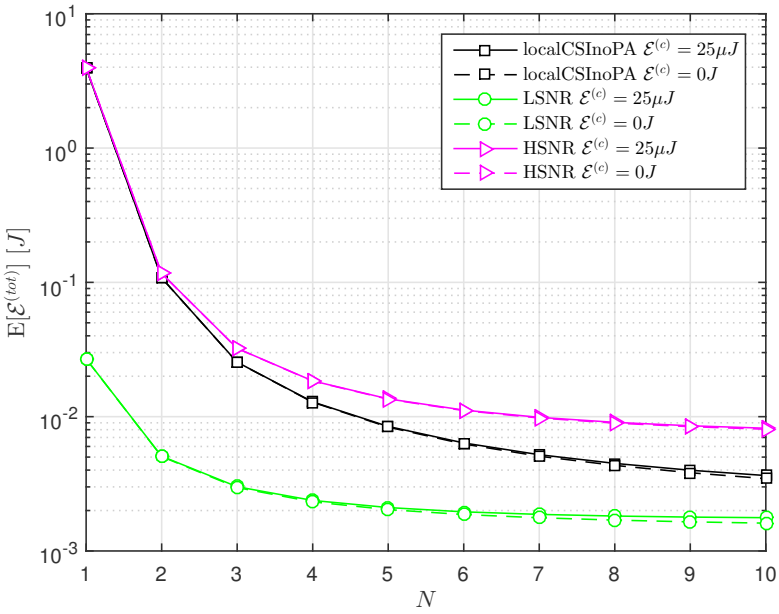

(b) User at cell edge

Figure 8.6: Average total energy versus number of available slots N for the localCSInoPA scenario and approximate solutions.

8.6.2 Average CSI case

We now assume that the transmitter only knows the average channel gain towards the BS, but not the exact fading term for any transmission resource. This scenario is denoted with *avgCSInoPA*. As usual, the first step consists in finding the minimum power that guarantees that the overall outage probability is less than ϵ when all the N resources are available.

Because of the lack of information about the current channel gain and the outcome of previous attempts, the best strategy for the device is to equally split the L bits in M sub-packets, and transmit such L/M bits in each resource, with constant power $P^{(tx)}$. Thus, both the transmit energy and the rate are kept constant over the transmission window, so that the channel fluctuations may cause packet losses. In particular, we remind that, according to (8.2), if $L/M > \rho_n$, the transmission in slot n is assumed to fail. Since, in this scenario, the failure of a single transmission attempt is sufficient to determine the loss of the entire packet, the corresponding overall outage probability is given by

$$\begin{aligned} \Pr[\text{outage}] &= 1 - \left(\Pr\left[TW \log_2 \left(1 + \frac{g_n P^{(tx)}}{N_0 W} \right) \geq \frac{L}{M} \right] \right)^M \\ &= 1 - \exp\left(-M \frac{(2^{L/(MTW)} - 1) N_0 W}{P^{(tx)}} \right), \end{aligned} \tag{8.32}$$

where the last term follows from the exponential distribution of g_n.

Similarly to the localCSInoPA case, we report in Fig. 8.7 a pictorial representation of the success and outage events in this context.

A simple functional analysis of (8.32) reveals that the outage probability is monotonically decreasing in M. Therefore, from the outage probability perspective, the best strategy is to use all the available resources, i.e. to set $M = N$.

Thus, imposing the outage probability equal to ϵ yields the following minimum required power per resource:

$$P^{(tx)^*} = \frac{N \left(2^{\frac{L}{NTW}} - 1 \right) N_0 W}{\ln\left(\frac{1}{1-\epsilon} \right)}. \tag{8.33}$$

Note that, with this assumption, the average number of transmissions is $\bar{n} = N$ because we are always using all the available resources to transmit.

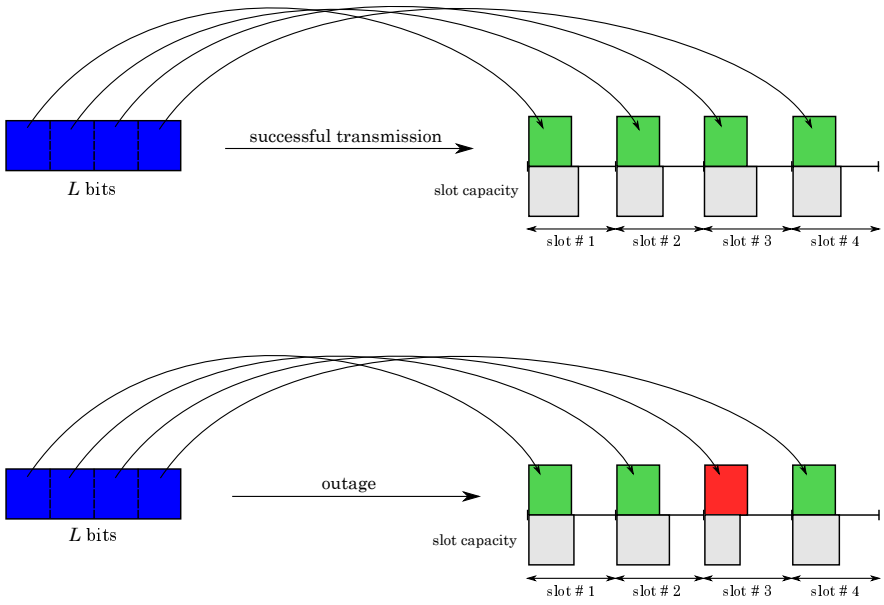

Figure 8.7: Success and outage events in the avgCSInoPA scenario.

8.6.3 Average CSI case with ARQ

In this section we extend the avgCSInoPA case by introducing Automatic Repeat-reQuest (ARQ) capabilities at the receiver. Thus, this scenario will be named *avgCSInoPA+ARQ*. Once again, we assume that the end device can arbitrarily split the payload in M packets of length L/M, where $1 \leq M \leq N$. In addition, the device can now retransmit the packets that are not acknowledged by the BS in the remaining resource blocks, if any. Therefore, the system is capable of recovering up to $N - M$ packet transmission failures. Following this reasoning, the outage event occurs when at least one of the sub-packets is not correctly detected at the receiver, accounting both the initial transmissions and possible retransmissions (see bottom image in Fig. 8.8). Conversely, when at least M out of N slots have capacity greater than $\frac{L}{MT}$ the message is correctly conveyed to the receiver (see top image in Fig. 8.8).

The number of potential successes in N resources can then be modelled as a Binomial process $V \sim \text{Bi}(N, 1 - \text{PER})$ with parameters N and $1 - \text{PER}$, where PER is the failure probability of a single packet transmission of length L/M. The condition on the outage probability can hence be expressed as

$$\Pr[V \leq M - 1] = 1 - I_{\text{PER}}(N - M + 1, M) \leq \epsilon \tag{8.34}$$

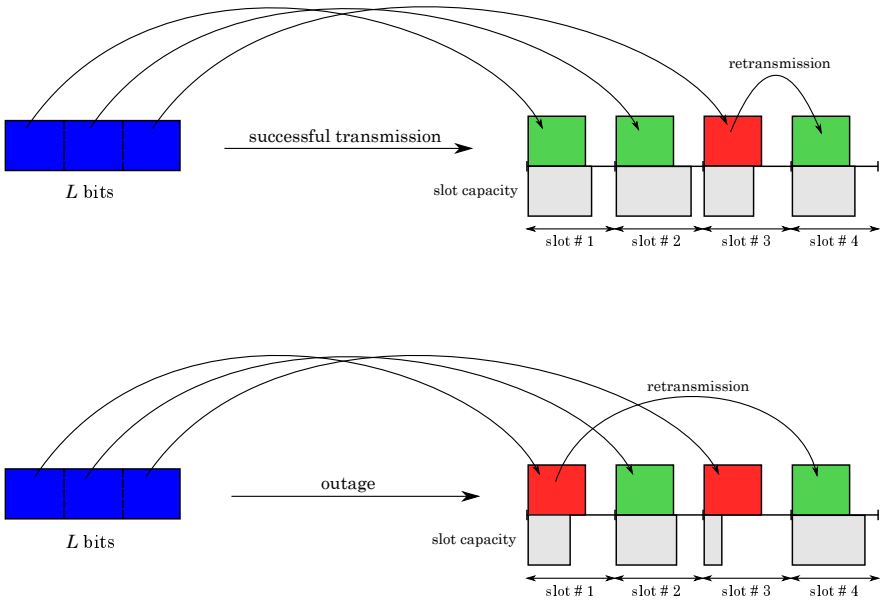

Figure 8.8: Success and outage events in the avgCSInoPA+ARQ scenario.

where $I_x(a,b) = \frac{\int_0^x t^{a-1}(1-t)^{b-1}\mathrm{d}t}{\int_0^1 t^{a-1}(1-t)^{b-1}\mathrm{d}t}$ is the regularized incomplete Beta function. Given N, we can invert the previous equation to obtain the maximum value PER_ϵ of the packet error probability that satisfies (8.34).

Now, recalling that $\{g_n\}$ are iid exponentially distributed, the error rate for any resource is

$$\mathrm{PER} = 1 - \exp\left(-\frac{\left(2^{\frac{L}{MTW}} - 1\right) N_0 W}{P^{(tx)}}\right) . \tag{8.35}$$

Setting (8.35) equal to PER_ϵ and solving in $P^{(tx)}$ we finally get

$$P^{(tx)^*} = \frac{\left(2^{\frac{L}{MTW}} - 1\right) N_0 W}{\ln\left(\frac{1}{1-\mathrm{PER}_\epsilon}\right)} , \tag{8.36}$$

which gives the minimal required transmission energy $P^{(tx)^*}$ per resource, as a function of M.

As an example, we report in Fig. 8.9 the optimal power per resource when varying M, for $N = 10$ and $\epsilon = 0.05$. Note that the rightmost value, i.e. $M = N$, which corresponds to the power obtained for the case without ARQ, as given by (8.33), is not the minimum. Therefore, by introducing the ARQ mechanism, it is possible to achieve the same outage probability with less energy consumption

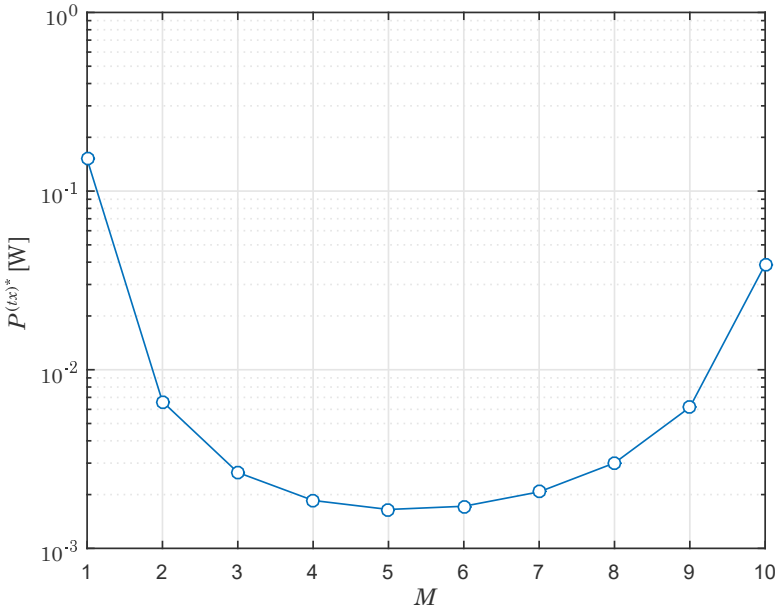

Figure 8.9: Minimal power per resource as a function of M with $N = 10$ and $\epsilon = 0.05$ in the avgCSInoPA+ARQ scenario.

per resource. However, the ARQ mechanism requires a feedback channel and some further processing. To account for the extra energy consumption due to the ARQ mechanism at the device side, we add a fixed cost $\mathcal{E}_{ARQ}$ per resource[3] in the energy metric defined in (8.4). Accordingly, the total energy cost per device for the ARQ case becomes

$$\mathcal{E}^{(tot)} = \sum_{n=1}^{N} \left(P^{(tx)^*} T + [\mathcal{E}^{(c)} + \mathcal{E}_{ARQ}] \chi \left\{ P^{(tx)^*} \right\} \right) \tag{8.37}$$

whose expectation is the function to be minimized.

In this case, the distribution of the number of resources that are actually used by the device in case of success can be modeled as a negative binomial function $\mathrm{NB}(M, 1 - \mathrm{PER}_\epsilon)$, which models the probability distribution of the number of independent Bernoulli trials, each with success probability $1 - \mathrm{PER}_\epsilon$, required to obtain exactly M successes. Instead, in case of outage, we will use all the N slots

[3]For the sake of simplicity, we assume that the ARQ cost is fixed. However, the framework can also accommodate more complex metrics.

available. We hence have

$$g(i) = \binom{i-1}{i-M}(1-\mathrm{PER}_\epsilon)^M \mathrm{PER}_\epsilon^{i-M},$$

for $i = M, \ldots, N-1$, while $g(N) = 1 - \sum_{i=1}^{N-1} g(i)$.

The average value $\bar{n}$ is then computed as in (8.23) and, in this case, it also depends on M.

8.7 Numerical Results

In this section we report the simulation results obtained by applying the different transmission policies described in the previous sections, namely fullCSI, localCSI, localCSInoPA, avgCSI, avgCSInoPA, and avgCSInoPA+ARQ. For each of them, we considered two reference scenarios: the user at the cell edge (low SNR), and the user close to the BS (high SNR), and computed the results with and without considering the circuit energy. The simulation parameters used are listed in Tab. 8.1. In particular, we underline that the circuit energy has been set to $E^{(c)} = 25\ \mu J$ per slot because, considering a slot duration of 1 ms, it corresponds to a basal power consumption of 25 mW, which is reasonable for common M2M transceiver chips [88].

Fig. 8.10 shows the average total energy as a function of N in the high SNR (left-most graph) and low SNR (right-most graph) cases for the strategies with power adaptation. The performance obtained with a circuit energy of $E^{(c)} = 25\ \mu$J are reported in solid lines, while dashed lines are used for the case with zero circuit energy.

At first glance, we note that the avgCSI case exhibits the worst performance. Of course, this is expected and is due to the reduced accuracy of the CSI with respect to the other scenarios.

Concerning localCSI, instead, its performance is very similar to that of the ideal fullCSI case. In particular, for a single resource ($N = 1$) the two policies are identical because in both cases they have knowledge of the channel gain in the only available slot. Increasing N, i.e., relaxing the delivery delay constraint, the performance gap between the two policies widens in favor of fullCSI, though the difference remains rather limited. Therefore, the localCSI strategy can be considered as a good compromise between practical applicability and performance. In

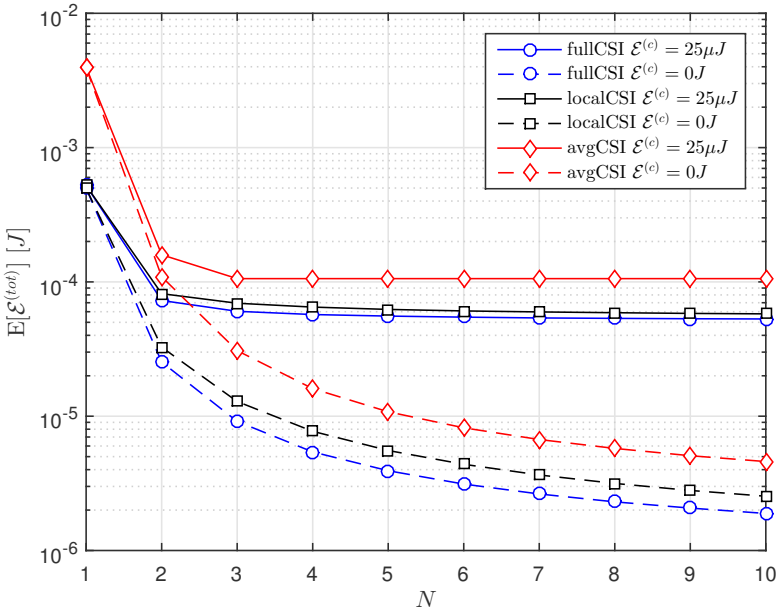

(a) User close to the BS

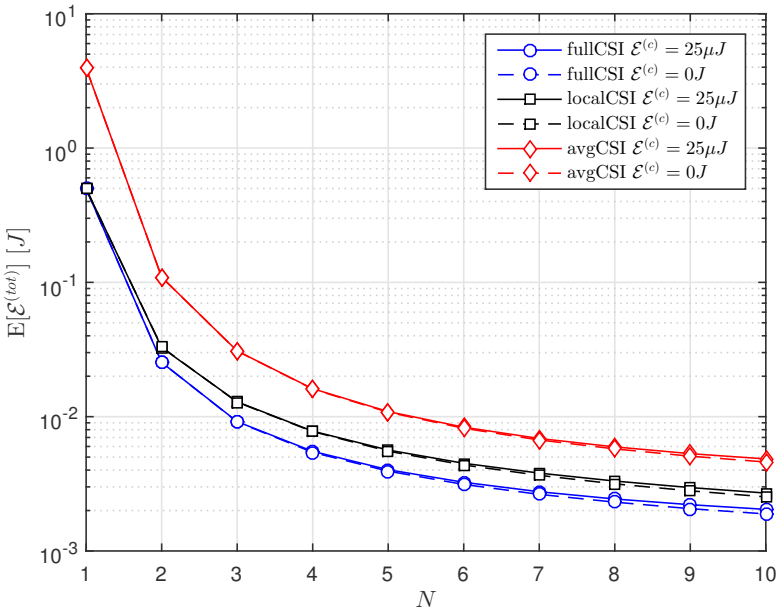

(b) User at cell edge

Figure 8.10: Average total energy versus the total number of available slots for the power adaptation schemes.

Description	Value
Packet length	$L = 500$ bits
Power spectral density	$N_0 = -164\ dBm$
Time duration per resource	$T = 1\ ms$
Bandwidth per resource	$W = 50\ kHz$
Average channel gain of the user close to the BS	$\bar{g} = -110\ dB$
Average channel gain of the user at cell edge	$\bar{g} = -140\ dB$
Circuit energy	$\mathcal{E}^{(c)} = 25\ \mu J$
Outage probability	$\epsilon = 0.05$

Table 8.1: Main parameters considered in the study on M2M energy minimization.

fact, if the assumption of knowing the channel gains over all resources beforehand as in the fullCSI case is unrealistic (especially when N is large), the localCSI policy requires only to estimate the current channel gain at the beginning of each slot, which is more realistic. We also point out that the solution of the dynamic programming problem described in Sec. 8.4, although computationally demanding, can be determined offline and then stored at the end-device.

Now, we focus on the impact of the circuit energy. With $\mathcal{E}^{(c)} = 0$, the average total energy cost decreases when increasing N, because the transmitter can split the packet in a greater number of sub-packets reducing the average rate per slot. Although such energy saving becomes progressively smaller as N increases, yet the expected total energy is monotonically decreasing with N, meaning that, without considering the circuit energy cost, it is always beneficial to increase the number of slots available for transmission. Of course this comes at the cost of accepting a greater delay $T_{max} = NT$ in the packet transmission. The situation changes when the circuit energy is non-negligible. Indeed, from Fig. 8.10 we see that, in this case, the minimal total energy is reached for a certain value of N: further increasing the available resources does not bring any benefit in terms of energy consumption.

To better appreciate these aspects we report in Fig. 8.11 the number of slots actually used by the different policies, again with and without circuit energy.

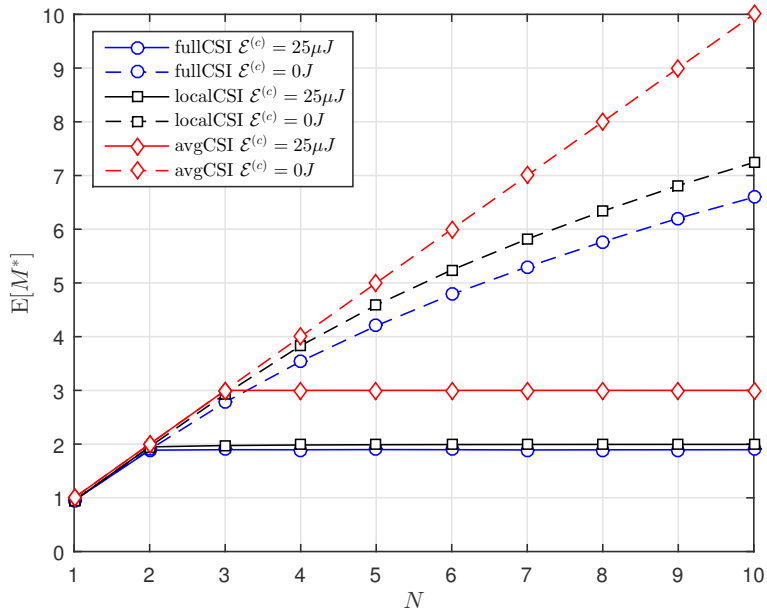

(a) User close to the BS

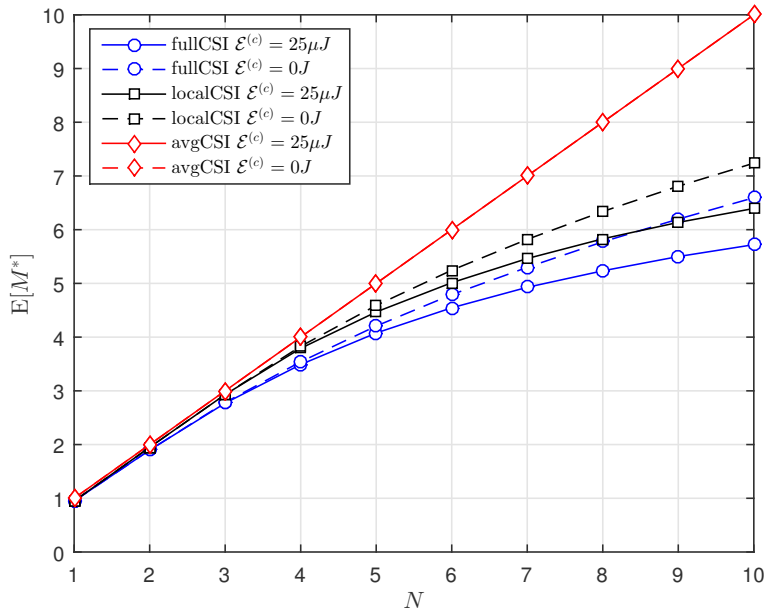

(b) User at cell edge

Figure 8.11: Average number of slots used (with non-zero energy) versus the total number of available slots for the power adaptation schemes.

In the avgCSI case all slots are equally good. Therefore, if the circuit energy is negligible, the optimal strategy consists in using all of them. Conversely, in the fullCSI and localCSI cases the user transmits only in the best time slots and stays silent in the remaining slots, even when the circuit energy is zero. These considerations hold for both the cell-edge and close to the BS users.

When the user is at the cell edge, we have that the transmit energy cost $P_n^{(tx)}T$ in (8.4) is much greater than the circuit energy term, because of the bad channel conditions. Therefore, the impact of the circuit energy on the transmission policies becomes less relevant, and the performance achieved with and without circuit energy is basically equivalent, as shown by the solid and dotted lines in Fig. 8.10(b) and Fig. 8.11(b), which are almost identical. A small gap can be seen for large values of N, because the transmit power per slot decreases and, thus, the impact of the circuit cost is more visible.

The circuit energy cost, instead, affects significantly the policies' performance in case the user is close to the BS. The transmit energy term is now similar to the circuit energy cost, even for a small number of slots, because of the good channel conditions. Therefore, the circuit energy cost becomes the limiting factor. In particular, from Fig. 8.11(a) we can see that for $N > 2$ the effect of the circuit energy cost is dominant, and makes not convenient, in terms of total energy, to transmit over a larger number of slots, even if available. For the avgCSI case we reach a minimum for $N = 3$, while for the fullCSI and localCSI cases, the performance still increases for $N > 2$, but the energy saving becomes almost insignificant.

Moreover, in Fig. 8.12 and Fig. 8.13 we report the corresponding results for the policies without power adaptation, i.e. localCSInoPA, avgCSInoPA, and avgCSInoPA+ARQ. Concerning CSI and circuit energy impact, we can draw similar considerations to those seen before for the strategies with power adaptation.

To evaluate the impact of ARQ capability, instead, we compare avgCSInoPA and avgCSInoPA+ARQ results. For small N, the two performance curves are almost identical, though the ACnoARQ case yields slightly higher total energy (hardly visible at the scale of the figure) due to the E_{ARQ} energy overhead. When there are few resources available, in fact, the set of possible values for M is very limited (see Sec. 8.6.3) and the retransmission capability cannot be exploited efficiently. In this case, the best choice is just to equally divide the message

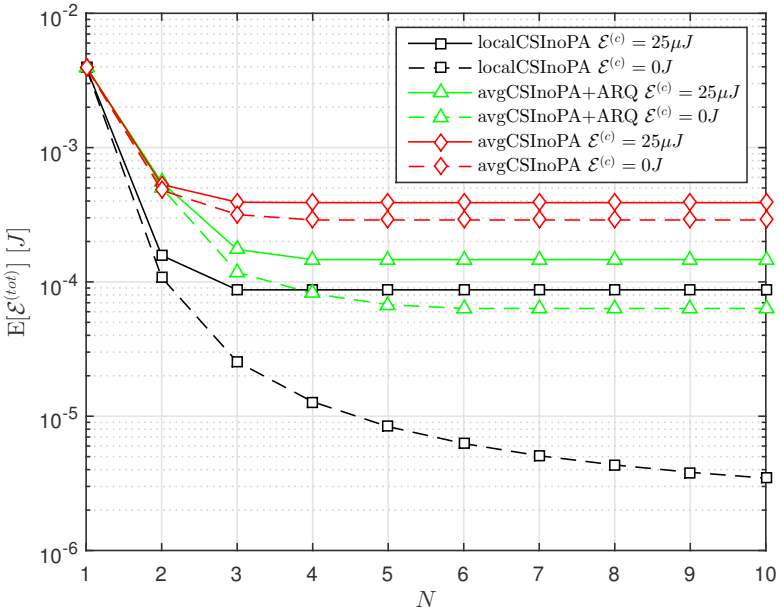

(a) User close to the BS

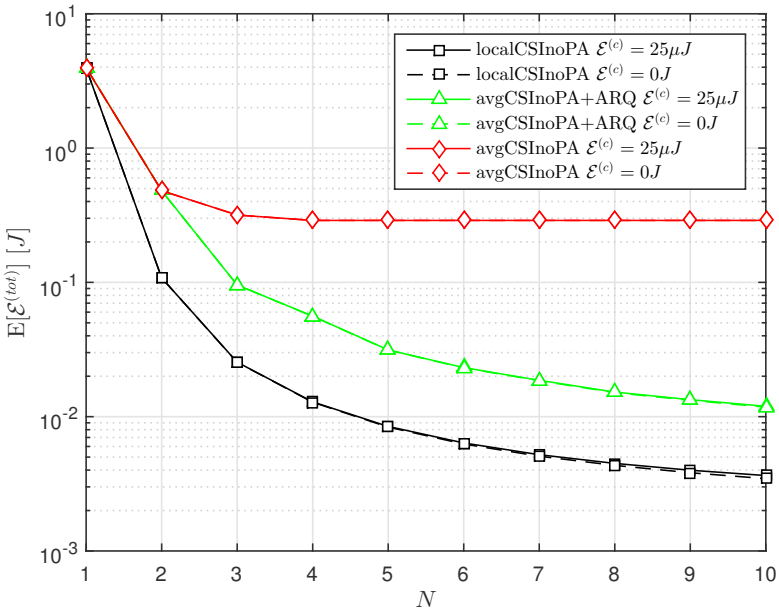

(b) User at cell edge

Figure 8.12: Average total energy versus the total number of available slots in the scenarios without power control.

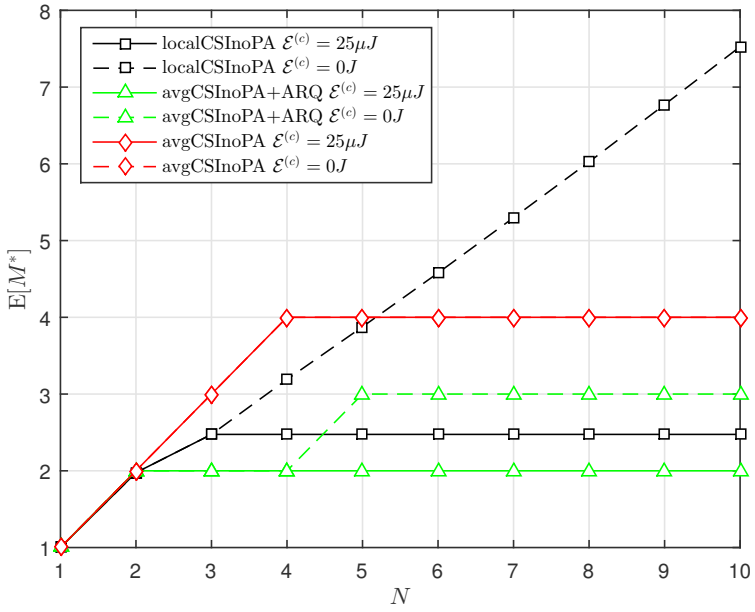

(a) User close to the BS

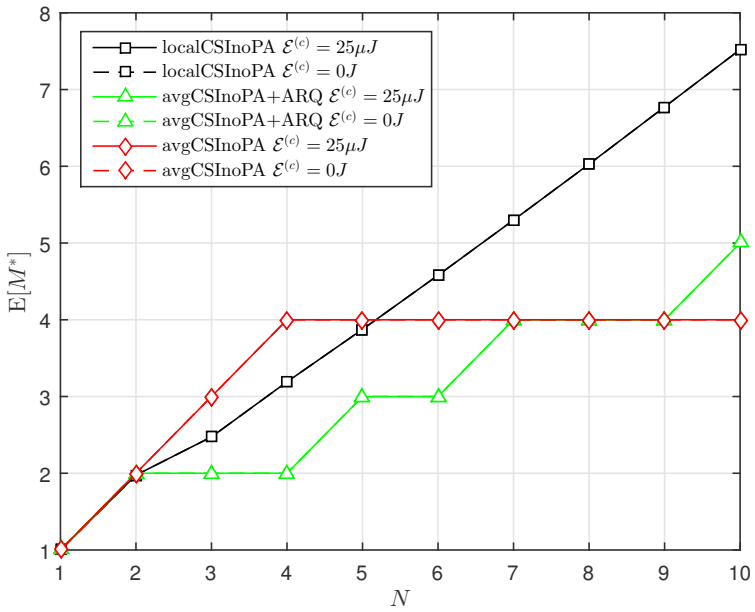

(b) User at cell edge

Figure 8.13: Average number of slots used (with non-zero energy) versus the total number of available slots in the scenarios without power control.

over all N resources, as for the scenario without ARQ, to make the most of the corresponding reduction on the required bitrate per slot. For larger values of N, instead, the contribution of the ARQ mechanism becomes significant (cf Fig. 8.9). In this case, the best strategy is to divide the message in a number $M < N$ of packets, and exploit the remaining resources to recover some failed transmissions.

Finally, comparing Fig. 8.12 and Fig. 8.13 with Fig. 8.10 and Fig. 8.11 we have a visual feedback of the impact of power adaptation. As expected, the possibility of adjusting the irradiated power throughout the transmission window significantly improves the performance. As a matter of fact, avgCSInoPA and avgCSInoPA+ARQ scenarios lead to the worst performance. Moreover, when we have power adaptation, it is sufficient to have only average channel information to reach almost the same performance as in the local CSI case without power control.

8.8 Discussion

In this work we solved the problem of energy minimization in a single-user wireless uplink network, with varying assumptions on the CSI at the transmitter and considering an energy model that accounts for both the device circuit energy cost and the transmit energy consumption. In particular, we derived the solution to the optimization problem in three different scenarios: perfect channel knowledge (fullCSI); exact knowledge of the channel gain in the current slot only (localCSI); and, finally, average information on channel conditions (avgCSI), which is probably the most likely case in an M2M context. We showed results for the different transmission strategies and, comparing their performance, we evaluated the impact of channel information and circuit cost on energy efficient scheduling. We noticed that the performance gap given by the complete knowledge of the channel gain in all slots, rather than the knowledge of the channel gain in the current slot only, may not justify the effort of collecting such a detailed information. Furthermore, we showed that the circuit energy can significantly affect the optimal transmission policies, in particular in good channel conditions.

9 Asymptotic analysis of M2M massive access

As anticipated in Ch. 7, M2M communications are expected to play a major role in the transition from the current cellular standard to next generation networks. Indeed, while the ad hoc reengineering of existing systems (GSM, UMTS, LTE) recently carried forward by 3GPP and some research groups [55, 56, 59] may initially satisfy the rising demand of wireless access from Machine-Type Devices (MTDs), the Internet of Things revolution will likely require new solutions designed from scratch, in order to become a reality. Today's radio systems, in fact, have been originally designed to support relatively few connections with high data rates. Thus, they are intrinsically unsuitable for M2M communications, which are conversely characterized by sporadic transmissions of small data packets from possibly a very large number of devices, with heterogeneous QoS specifications.

This vision motivates the study of new cellular protocols and network architectures natively designed to support both M2M applications and conventional Human-to-Human (H2H) services. However, while the fundamental limits for broadband systems are generally well understood, a similar level of understanding for M2M systems is still lacking. As a matter of fact, the centrally coordinated access mechanism, adopted by most of today's wireless cellular systems, presents severe limitations in the M2M context. Indeed, with machine-type applications typically generating payloads of less than 1 kB, the signaling commonly used to set up and maintain mobile broadband data connections may become the bottleneck of the system, substantially limiting the performance of both M2M and conventional services. On the other hand, uncoordinated schemes have been proved to be able to asymptotically reach the efficiency of coordinated access protocols, without the burden of the signaling overhead associated to the latter.

Some such evidence is given in [80], where the performance of coordinated and uncoordinated transmission strategies for multiple access is analyzed. That work shows that, for the typical length of M2M data payloads, uncoordinated access schemes support more devices than coordinated access mechanisms, because of the lower signaling overhead.

In the context of random access schemes, a promising solution to increase the capacity of wireless networks based on uncoordinated access schemes consists in providing Multi-Packet Reception (MPR) capabilities to the receiver, which will hence be able to decode multiple overlapping packets by using different techniques [88, 89]. A possible method to enable MPR without excessively increasing the complexity of the end devices consists in using pseudo-orthogonal spreading codes to decrease the power spectral density of the transmission and, hence, limit the interference at the receiver. This is particularly effective if combined with Successive Interference Cancellation (SIC) at the receiver, which allows the receiver to (partially) remove the contribution of all decoded signals from the compound received signal, thus possibly enabling the successive decoding of other overlapping transmissions. The combination of MPR and SIC can hence enable the correct decoding of a large number of transmissions that overlap in time and frequency, thus dramatically increasing the probability of successful channel access in random access wireless systems [90]. The downside is that the spreading techniques enlarge the bandwidth required to transmit the signal which, for a fixed system bandwidth, decreases the effective bit rate that can be offered to the higher layers, while on the other hand SIC requires rather sophisticated receivers.

Nonetheless, the combined use of MPR and SIC appears particularly appealing in the context of M2M, where the aim is to guarantee high channel access probability to many nodes that have low transmit rates [77]. In this chapter we investigate the limiting performance of such a scenario when the population of transmitters grows, while the per-user bitrate decreases. By building upon the model developed in [90], we find an approximate model to estimate the maximum throughput of a wireless cellular system, where the receiver is capable of performing MPR and perfect SIC. The throughput here is defined as the average number of transmissions that can be successfully decoded per packet duration. The theoretical results provided by the model are validated against simulation results, which show that the model tends to slightly overestimate the actual system

throughput, but is able to capture the general trend when changing the scenario, i.e., the statistical distribution of the received signal powers and the MPR capabilities of the receiver. Furthermore, the model shows that the throughput tends to grow linearly with the MPR capabilities of the system that, in turn, are inversely proportional to the per-user bitrate. This tradeoff implies that the product of throughput and bitrate asymptotically tends to a constant which depends on the statistical distribution of the signal powers at the receiver.

The remainder of this chapter is organized as follows. Sec. 9.1 overviews the prior work related to this subject. In Sec. 9.2 the asymptotic analysis of an MPR system with SIC capabilities is presented. Then, theoretical and simulation results for such a system are illustrated in Sec. 9.3. Finally, Sec. 9.4 presents some final remarks.

9.1 Related work

As mentioned, the introduction of uncoordinated access schemes with MPR capabilities at the receiver may significantly impact the performance in M2M scenarios since it allows the detection of multiple overlapping signals in the event of a collision, thus making it possible to increase the system throughput even when transmitters are not centrally coordinated. The relevance of such a signal-capture phenomenon in mobile radio systems has been recognized since long, producing a quite rich literature. A first attempt at the analysis of MPR-capable wireless systems was made in [91], where the stability of the ALOHA system is studied under infinite-user single-buffer assumptions. The paper, however, models the number of transmissions successfully decoded in a slot as a random variable that only depends on the number of overlapping signals, without considering the signal power distribution. Another simplistic capture model is considered in [92], where the authors assume that all signals are decoded if the sum rate of all the transmitting users does not exceed the capacity of the channel, whereas in [93] a signal is captured whenever the strongest interferer is sufficiently far apart from the target receiver, according to a statistical geometry approach.

Successively, the analysis of the capture effect was extended and made more realistic by including in the capture model basic physical propagation phenomena and the cumulative character of interference, considering the random distribution

of the signal powers at the receiver, and introducing a capture criterion based on the Signal-to-Interference-plus-Noise-Ratio (SINR) of the signals [90, 94, 95].

On the other hand, the use of interference cancellation to improve the channel access probability has been investigated in [75], where the authors present an enhanced version of Slotted ALOHA, called Frameless ALOHA, that exploits SIC to increase the number of packets that can be successfully transmitted over a single slot. This protocol takes inspiration from the rate-less code paradigm: users transmit replicas of their packets in the slots of a frame, whose length is changed at each contention round according to the outcomes of the previous round. The transmission slots are picked at random, according to a Bernoulli process of given probability. Every packet includes pointers to all its replicas so that, upon decoding one packet, the receiver can cancel the corresponding signal from the compound signals received in all the slots where a replica of the packet was sent. This can lead to the resolution of new packets, thus increasing the system throughput. The effectiveness of this approach is confirmed by the results provided in [75], where the protocol is shown to achieve an asymptotic efficiency around 87%, much larger than the classical Slotted ALOHA performance.

Recently, interference cancellation was also applied to cognitive radio networking. In [96], the authors investigate a scenario where primary (licensed) users and secondary (unlicensed) users share the same spectrum in order to communicate with their respective receivers. Primary users are assumed to implement a retransmission-based error control technique, which implies the retransmission of a copy of the failed packets over subsequent time slots. This behavior gives rise to redundancy in the interference generated by the primary user to the secondary user, which can be exploited to design secondary transmission policies. The basic idea is that, if a secondary receiver detects the primary user message in a given initial transmission, then it can use this knowledge to cancel the primary interference in the subsequent slots in case of primary retransmissions, thus achieving a larger secondary throughput. Indeed, this result is confirmed by the comparison between the performance of the above-mentioned technique and those of a couple of suboptimal policies that do not exploit interference cancellation.

In this work, we focus on the maximum number of transmissions that can be successfully decoded in a single slot, without considering the possibility of exploiting retransmissions in successive slots to further increase the performance.

Instead, the analysis takes into account the MPR capabilities of the receiver, and the effect of signal power distribution.

9.2 Asymptotic massive access capacity

As mentioned, the model presented in this work builds upon the mathematical framework developed in [90], which provides the expression of the probability mass distribution of the number r of signals that can be successfully decoded when n transmissions overlap in time and frequency at the receiver. The reference model is reported in the following, for the reader's convenience.

Denoting with P_i the power of the ith signal at the receiver, the SINR is given by

$$\gamma_i = \frac{P_i}{\sum_{j \neq i} P_j + N_0} \tag{9.1}$$

where N_0 is the background noise power, which will be henceforth neglected for simplicity. Signal i is assumed to be successfully decoded if

$$\gamma_i > b, \tag{9.2}$$

where $b > 0$ is the so-called *capture threshold* of the system. Note that, without SIC, the maximum number of signals that can be successfully decoded is limited to $\left\lceil \frac{1}{b} \right\rceil$. Therefore, MPR capabilities require $b < 1$ or SIC, or both.

We consider a scenario where n terminals (machine type devices) simultaneously transmit packets of equal size to a common receiver, the Base Station (BS), which is capable of MPR and *perfect SIC*. More specifically, we assume that signal decoding at the BS is an iterative process. At each iteration, all signals that satisfy the capture condition (9.2) will be successfully decoded. Hence, the corresponding contributions can be cancelled out of the compound received signal. The entire decoding procedure is then repeated on the remaining signal, until all overlapping transmissions are successfully detected, or no signal satisfies (9.2).

The received signal powers at the BS are modelled as independent and identically distributed (iid) random variables $\{P_j, j = 1, \ldots, n\}$, with common Cumulative Distribution Function (CDF) $F(x)$, $x \geq 0$. The number of correctly decoded signals at the first iteration [90] can be expressed as

$$\rho = \sum_{j=1}^{n} \chi \{\gamma_j > b\} \tag{9.3}$$

where $\chi\{A\} = 1$ if condition A holds true and 0 otherwise. Taking the expectations of both sides, we hence get

$$r = n \Pr[P_j > \mathcal{I}_0] \tag{9.4}$$

where $\mathcal{I}_0 = \sum_{i \neq j} P_i b$. Eq (9.4) is the average number of signals that are captured by the BS before performing SIC. Now, in [90], a simple recursive method is proposed to estimate the mean number of signals that can be decoded at each successive SIC iteration. Being the basis of the analysis developed in this work, we here recollect the recursive method, considering only the case with zero-residual interference after cancellation (i.e., assuming $z = 0$ according to the notation used in [90]).

9.2.1 Recursive throughput expression with SIC

First of all, (9.4) is simplified by replacing $\mathcal{I}_0$ with its first order approximation $I_0 = (n-1)b\,\mathrm{E}[P_j]$, which gives:

$$\tilde{r} = n \Pr[P_j > (n-1)b\,\mathrm{E}[P_j]]\,. \tag{9.5}$$

We then denote as $\tilde{r}_h$ the estimation of the mean number of signals that are captured at the hth iteration, where $h = 0, 1, \ldots$. In particular, from (9.5), we get:

$$\tilde{r}_0 = n \Pr[P_j > I_0]\ . \tag{9.6}$$

These signals are then removed from the set of n overlapping signals, so that after the first SIC operation, the remaining signals are (approximately):

$$n_1 = n - \tilde{r}_0 = n \Pr[P_j \leq I_0] = nF(I_0)\,. \tag{9.7}$$

Note that all these signals have power less than or equal to I_0, otherwise they would have been decoded at the previous iteration.

Repeating this reasoning, the average number of signals decoded at this new iteration can be approximated as:

$$\tilde{r}_1 = n_1 \Pr[P_j > I_1 | P_j \leq I_0]\,, \tag{9.8}$$

where $I_1 = b(n_1 - 1)\,\mathrm{E}[P_j | P_j \leq I_0]$ is the approximate expression of the aggregate interference power of $n_1 - 1$ signals, scaled by the capture threshold b, and $\mathrm{E}[x|y]$ denotes the conditional expectation of x given y.

After the generic hth SIC iteration, we then have

$$\begin{aligned} n_h &= n - \sum_{j=0}^{h-1} \tilde{r}_j \; ; \quad I_h = b(n_h - 1)\,\mathrm{E}\left[P | P \leq I_{h-1}\right] \; ; \\ \tilde{r}_h &= n_h(1 - \Pr\left[P \leq I_h | P \leq I_{h-1}\right]) \; ; \end{aligned} \tag{9.9}$$

Finally, the approximate normalized throughput after K SIC iterations is given by

$$\tilde{S}_n^{(s)}(K) = \sum_{j=0}^{K} \tilde{r}_j \, . \tag{9.10}$$

9.2.2 Fixed point throughput expression with unlimited SIC

Starting from the recursive expression in (9.9), we here derive an approximate expression for the system throughput when the number of allowed SIC iterations is unlimited, i.e., $K = \infty$.[1] In other words, we suppose that the decoding process stops only when no further signal satisfies the capture condition.

We rewrite n_2 as follows

$$\begin{aligned} n_2 &= n_1 - \tilde{r}_1 \\ &= n_1 \Pr\left[P_j \leq I_1 | P_j \leq I_0\right] \\ &= n \Pr\left[P_j \leq I_0\right] \Pr\left[P_j \leq I_1 | P_j \leq I_0\right] \\ &= n \Pr\left[P_j \leq \min\{I_0, I_1\}\right] \\ &= n \Pr\left[P_j \leq I_1\right] \\ &= nF(I_1). \end{aligned} \tag{9.11}$$

where the second and third rows are obtained using (9.8) and (9.7), respectively, while the second-to-last row follows from the fact that I_k is always non-increasing in k. Repeating iteratively, we get that the average number of signals that remain to be decoded after K SIC cycles can be estimated using the following recursive expressions

$$n_K = nF(I_{K-1}), \quad I_K = (n_K - 1)b\,\mathrm{E}\left[P | P \leq I_{K-1}\right], \tag{9.12}$$

for $K = 1, 2, \ldots$, where

$$\mathrm{E}\left[P | P \leq I_{K-1}\right] = \frac{\int_0^{I_{K-1}} x f(x) \mathrm{d}x}{F(I_{K-1})}$$

[1] A preliminary formulation of this expression was presented in [77].

is the average power of any still undecoded signal, being $f(x)$ the (unconditional) probability density function of the signal received powers.

The system throughput (9.10) after K SIC iterations, hence, can be expressed as the difference between the number n of overlapping transmissions and the number of residual signals after K SIC iterations, i.e.,

$$\tilde{S}_n^{(s)}(K) = n - n_K \,. \tag{9.13}$$

Letting K grow to infinity, the maximum achievable throughput can thus be approximated as

$$S(n) = n - \lim_{K\to\infty} n_K = n(1 - F(I_\infty(n))) \tag{9.14}$$

where $I_\infty(n)$ is equal to the fixed-point of (9.12), i.e.,

$$I_\infty(n) = (nF(I_\infty(n)) - 1)\, b\, \mathrm{E}\left[P | P \leq I_\infty(n)\right] \,, \tag{9.15}$$

provided it exists, and $I_\infty(n) = 0$ otherwise.

9.2.3 Optimal number of simultaneous transmissions

Clearly, (9.14) linearly increases with n as long as (9.15) does not admit any other solution than $I_\infty(n) = 0$. In this respect, a simple functional analysis reveals that (9.15) always admits positive solutions when n exceeds a certain threshold. For values of n larger than such a threshold, the throughput given by (9.14) starts decreasing. As a proof of concept, we plot in solid lines in Fig. 9.1 the throughput estimate given by (9.13) for different values of K, as reported in the legend, and the asymptotic value given by (9.14) for $K = \infty$, when varying n. The marks in the figure, instead, correspond to the simulation results in the same conditions. These results have been obtained by considering the Rayleigh Fading (RF) scenario defined in [90], where the received signal powers are iid exponential random variables with unit mean. Furthermore, the capture threshold has been set to $b = 0.02$.

From the figure, we observe that the throughput approximation is excellent for relatively small values of K, while it tends to overestimate the actual performance when $K \to \infty$. More importantly, we note that the throughput equals the number of simultaneous transmissions n up to a critical value n^*, beyond which the performance decreases sharply. However, according to (9.14), $\tilde{S}_n^{(s)}(K) < n$

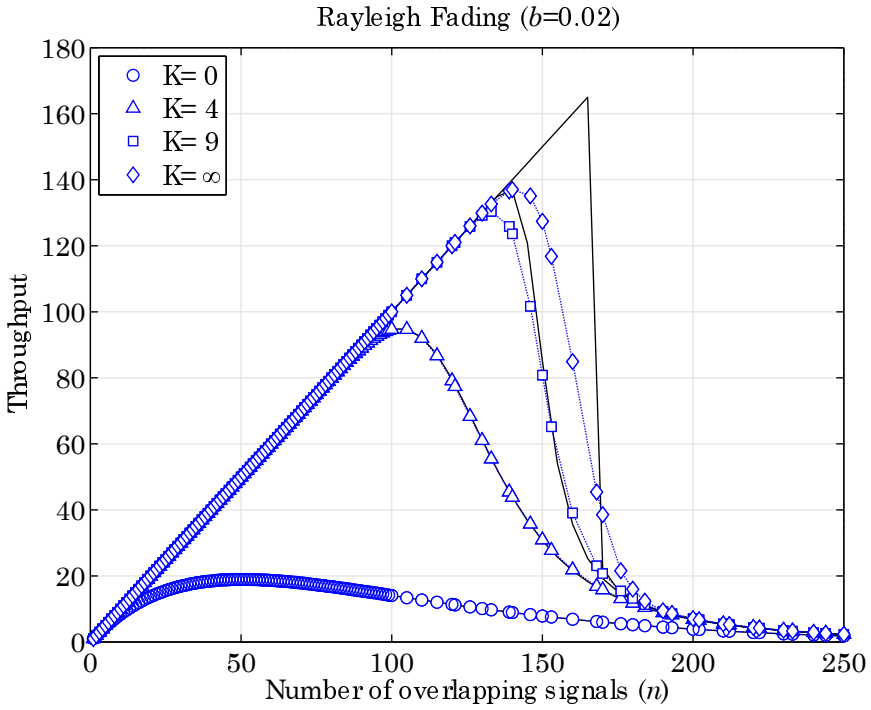

Figure 9.1: Approximate (solid lines) and simulated (dotted lines with markers) throughput when varying n, when increasing the number K of SIC cycles.

only if $F(I_\infty(n)) > 0$ and, hence, $I_\infty(n) > 0$. Therefore, the critical value n^* corresponds to the maximum n for which the fixed-point equation (9.12) does not admit any positive solution. To find such a value, we can express n as a function of the unknown $x = I_\infty(n)$, so that the fixed point equation (9.15) yields

$$n(x) = \left(\frac{x}{b\,\mathrm{E}\left[P|P \le x\right]} + 1 \right) \frac{1}{F(x)} \,. \tag{9.16}$$

Now, it is easy to realize that the right-hand side of (9.16) is continuous and positive, grows to infinity for $x \to 0$ and for $x \to \infty$, and therefore has a minimum for some positive x^*. As an example, in Fig. 9.2 we report the graph of $n(x)$ when varying x for the RF scenario, for which we get

$$n(x) = \left(\frac{x(1-e^{-x})}{b(1-e^{-x}(x+1))} + 1 \right) \frac{1}{1-e^{-x}} \,. \tag{9.17}$$

To find the global minimum, we set to zero the derivative in x of (9.16). After some algebra, we get

$$F(x)\,\mathrm{E}\left[P|P \le x\right] = f(x)\left(x^2 + b\,\mathrm{E}\left[P|P \le x\right]^2\right) \tag{9.18}$$

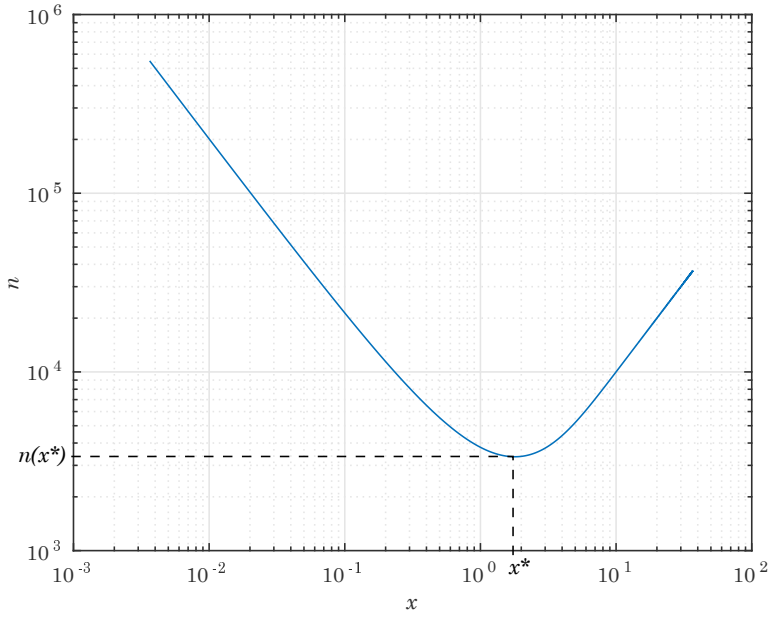

Figure 9.2: Values of n for which the fixed-point equation (9.15) admits positive solutions $I_\infty(n) = x > 0$, and critical threshold n^*.

whose solution(s) can be found using numerical methods.[2]

Replacing x^* into (9.16), and rounding down the result, we finally get the critical value n^* of n after which the approximate throughput starts decreasing. As a matter of fact, it is easy to prove that $S(n^*+1) < S(n^*)$. In fact, being n^* the maximum value of n for which (9.15) does not admit positive solutions, we have that the approximate throughput will equal n for any $n \leq n^*$, in particular $S(n^*) = n^*$.

Therefore, we need to prove that

$$S(n^*+1) < n^* \,. \tag{9.19}$$

Using (9.14) in (9.19), we get

$$(n^*+1)(1 - F(x(n^*+1)) < n^* \;\longrightarrow\; (n^*+1)F(x^*) > 1 \,, \tag{9.20}$$

where in the rightmost inequality we approximate $x(n^*+1)$ with x^*. Now, using

[2]In general, (9.18) may admit multiple solutions. In this case, x^* is the solution that minimizes $n(x^*)$ as given by (9.17)

(9.15), we get

$$((n^* + 1)F(x^*) - 1)\, b\, \mathrm{E}\left[P | P \leq x^*\right] = x^* > 0\,,$$

from which we get $(n^* + 1)F(x^*) > 1$, as required by (9.20).

Summing up, the approximate throughput (9.14) is maximized when the number of simultaneous transmissions equals the critical threshold n^*, which depends on the capture threshold b of the receiver, and on the CDF $F(x)$ of the received signal powers. Hence, given the statistical distribution of the signals, the maximum achievable throughput can be approximated as

$$S^*(b) = \max_n S(n^*(b)) \simeq n^*(b)\,, \tag{9.21}$$

where $n^*(b)$ is the critical value of n for a given b.

9.3 Results

In this section we exploit the results derived so far to gain some insight on the optimal performance of a random access system with a receiver capable of performing MPR of all signals with SNR above the threshold b, and SIC, in an iterative manner. More specifically, we are interested in investigating the asymptotic performance of the throughput as the capture threshold b decreases, thus admitting more transmitters with lower rate.

First of all, we report in the top part of Fig. 9.3 the optimal throughput when varying the capture threshold b in the RF scenario. The approximation given by (9.21) is shown in blue solid line with markers, while the red line represents simulation results. We can note that the optimal throughput is approximately equal to $S^*(b) = \alpha/b$, where the coefficient α depends on the statistical distribution of the received signal powers. Indeed, although not shown in the figure to reduce clutter, the results obtained for the other two scenarios defined in [90], i.e., pure path loss and shadowing channels, are essentially the same, except for a small difference in the coefficient α. Furthermore, we observe that the approximation is slightly optimistic, in particular for larger values of b. This mismatch is likely due to the progressive worsening of the approximation I_h of the residual interference as the number of SIC cycles increases. Indeed, it is easy to realize that, given k residual signals sorted in increasing order of received power, and if a is the power

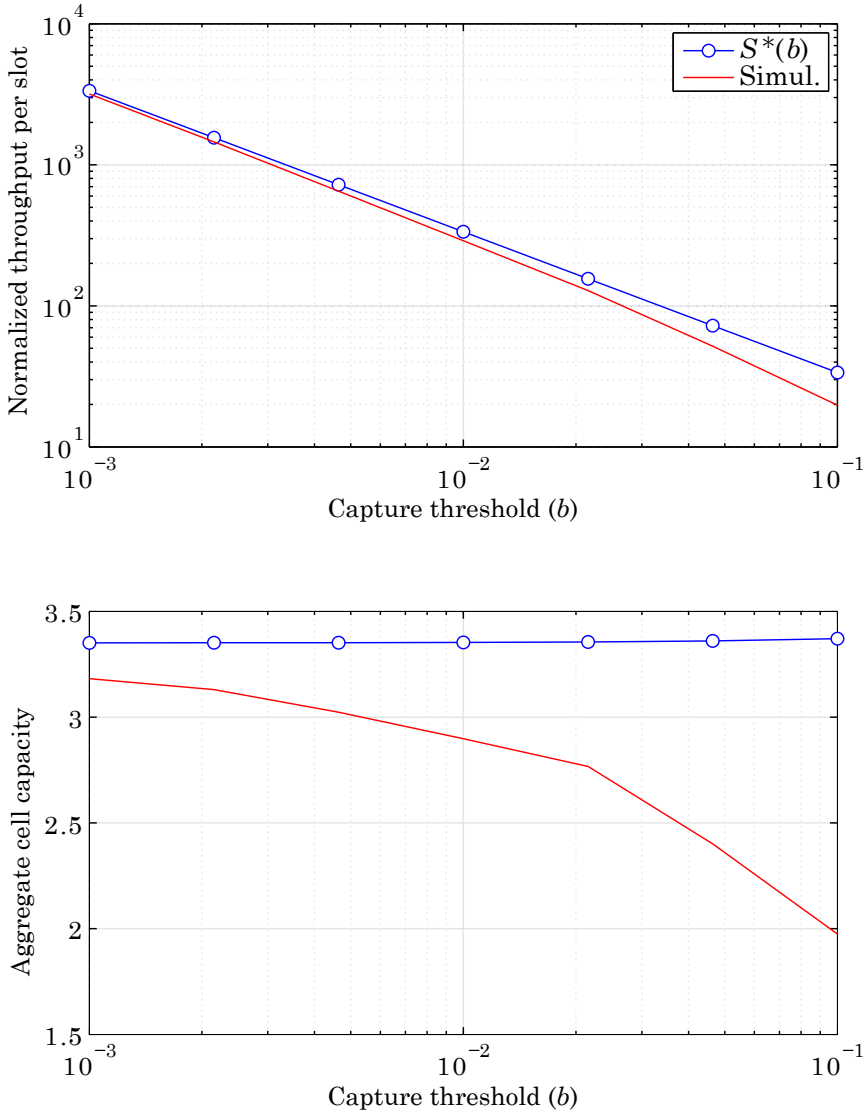

Figure 9.3: Optimal throughput when varying b for the approximate theoretical models and simulations.

of the strongest such signal, i.e., $P_k = a$, the iterative decoding process stops if and only if

$$\begin{aligned} &\Pr\left[a \leq b\sum_{j\neq k} P_j \Big| P_j \leq a,\, \forall j\right] \\ &= \Pr\left[\frac{\sum_{j\neq k} P_j}{k-1} > \frac{a}{b(k-1)} \Big| P_j \leq a,\, \forall j\right] \\ &\simeq Q\left(\frac{\dfrac{a}{b\sqrt{k-1}} - \sqrt{k-1}\,\mathrm{E}\left[P|P\leq a\right]}{\mathrm{STD}(P|P\leq a)}\right) \end{aligned} \tag{9.22}$$

where in the last step we resorted to the central limit theorem to approximate the mean of $k-1$ iid random variables as a normal random variable with mean $\mathrm{E}\left[P|P\leq a\right]$ and standard deviation $\mathrm{STD}(P|P\leq a)/\sqrt{k-1}$. Now, it is apparent that, for large values of k, the probability (9.22) grows to 1 with a step that depends on the conditional standard deviation $\mathrm{STD}(P|P\leq a)$: the smaller the range over which the signal powers are distributed, the higher the probability that the decoding process stops with k residual signals. Now, after each SIC cycle, the powers of the remaining signals are compacted in a smaller interval, so that $\mathrm{STD}(P|P\leq a)$ progressively decreases. Furthermore, the larger b the sooner (9.22) starts growing with k. This aspect is not captured by the recursive model (9.9) that, hence, yields an upper bound to the number of signals captured. Actually, the approximation can be improved by taking into account the model (9.22), though this is out of the scope of this work.

Although not very accurate when the number of SIC cycles is large and the capture threshold b is close to 1, yet the model is capable of capturing the linear dependence of $S^*(b)$ upon $1/b$, which is quite interesting. The lower graph of Fig. 9.3 reports the parameter α, given by the product of the optimal throughput $S^*(b)$ and the capture threshold b. Once again, the markers identify the theoretical results, while the red curve refers to simulation outcomes. In practice, when MPR is achieved by means of spread spectrum techniques, the capture threshold b can be interpreted as a scaling factor of the bit rate of each terminal. Therefore, the coefficient α represents the aggregate transmit rate that can be sustained by the system. From the figure, we observe that the gap between the theoretical and simulation results is more visible in this graph, due to the much smaller range of the values. Nonetheless, the model asymptotically approaches the value returned by simulations. Furthermore, we note that the aggregate system capacity

remains almost constant when varying b, which means that the random access scheme with MPR and SIC can accommodate a variable number of terminals, provided that the transmit rates are proportionally scaled.

9.4 Remarks

In this chapter, we proposed an approximate analysis of the asymptotic throughput of a wireless channel in the presence of massive access from low-rate terminals, with disparate signal powers. The mathematical model, though overoptimistic in its estimate of the system performance, is capable of capturing some fundamental properties of the system. Indeed, we showed that, with ideal SIC, the MPR capabilities of the receiver can be fully exploited even using a slotted random access mechanisms. However, achieving the optimal performance requires a quite accurate control of the total number of transmitters, since the throughput rapidly decreases if the critical threshold $n^*(b)$ is exceeded.

As future work, we plan to improve the accuracy of the mathematical model and to relax some simplifying assumptions, such as ideal SIC. Furthermore, we plan to include protocol aspects into the model such as, for instance, mechanisms to limit the number of simultaneous transmitters, and techniques to exploit transmissions in multiple slots. Finally, energy aspects, which are very sensitive in M2M scenarios as discussed in Ch. 8, will also be considered.

10 Conclusions

The implementation of M2M services has been identified as one of the most challenging objectives of 5G. While the general requirements of 5G systems are progressively taking shape [97, 98], the technological issues raised by the M2M paradigm are still partially unsolved. Among them, two critical aspects are energy-efficient communications and massive access support.

Indeed, while the fundamental limits for broadband systems are well understood in the literature and considered by the standardization initiatives, a similar level of understanding for MTC-oriented systems is still lacking. Finding such limits will serve as a basis to design efficient and flexible MTC systems. Motivated by this consideration, in this work we first investigated the theoretical bounds of energy-efficient MTCs and then addressed the problem of massive access in the M2M context adopting a clean-slate and standard-agnostic approach. The final intent was to provide insights on the fundamental aspects of MTC, thus contributing to the definition of radio protocols and architectural principles able to serve a large number of MTDs connections with minimal energy consumption.

A

Microfluidic Networking Appendices

A.1 Admissible parameters for the microfluidic bus network

From (4.8) it is easy to realize that $\rho_H(n)$ takes the values in the interval

$$\Delta_n = (R_n - R_{\mathrm{eq},n}, R_{n+1} - R_{\mathrm{eq},n+1}), \quad n = 1, \ldots, N. \tag{A.1}$$

Using (4.2) in (A.1) we obtain

$$\Delta_n = \frac{\alpha - 1}{\alpha}(R_n, R_{n+1}), \quad n = 1, \ldots, N. \tag{A.2}$$

The length of such an interval can then be expressed as

$$|\Delta_n| = \frac{\alpha - 1}{\alpha}(R_{n+1} - R_n) = RC_1(\alpha, n) \tag{A.3}$$

where the last step follows from (4.4), with

$$C_1(\alpha, n) = \frac{(\alpha - 1)\alpha^n}{(\alpha + 1)^n}. \tag{A.4}$$

The parameter $C_1(\alpha, n)$ is a measure of the design space of ρ_n: the smaller $C_1(\alpha, n)$, the stricter the interval of admissible values for ρ_n and, hence, the less robust the system to structural imperfections or process noise. For a given $\alpha > 1$, $C_1(\alpha, n)$ is monotonically decreasing in n and, for $n = N$, it reaches the minimum, $C_1(\alpha, N) = (\alpha - 1)[\alpha/(\alpha + 1)]^N$. On the one hand, $C_1(\alpha, N)$ should be as large as possible to increase the system robustness. On the other hand, increasing $C_1(\alpha, N)$ requires larger α and, in turn, longer channels and higher resistances. Therefore, there is clearly a tradeoff between system robustness and efficiency.

Another constraint on the design parameter α is obtained by considering that the header droplets must be fully contained in the segment of length L that separates two consecutive outlets; otherwise, the behavior at the junctions would not be longer predictable. As per (1.14), given the microfluidic channels geometry and the characteristics of the continuous and dispersed fluids, $\rho_H(n)$ is proportional to the length $\ell_H(n)$ of the header droplet dispersed in the channel. Since $\ell_H(n)$ grows with $n = 1, \ldots, N$, we shall hence guarantee

$$\ell_H(N) < L \tag{A.5}$$

which, using (1.12) and (1.14), can be expressed as

$$\rho_{H,n} < R(\lambda - 1) \tag{A.6}$$

where $\lambda = \frac{\mu_d}{\mu_c}$. Now, since $\rho_n \in \Delta_n$, from (A.2) and (4.4) we can set

$$\begin{aligned} \rho_{H,n} &= \frac{\alpha - 1}{\alpha} \left(\beta R_{n+1} + (1-\beta) R_n\right) , \\ &= R(\alpha^2 - 1) \left[1 - \left(\frac{\alpha}{1+\alpha}\right)^n \left(1 - \frac{\beta}{1+\alpha}\right)\right] . \end{aligned} \tag{A.7}$$

Condition (A.6) can finally be written as

$$C_2(\alpha, N) < 1 \tag{A.8}$$

where, for shortness of notation, we set

$$C_2(\alpha, N) = \frac{\alpha^2 - 1}{\lambda - 1} \left[1 - \left(\frac{\alpha}{1+\alpha}\right)^N \left(1 - \frac{\beta}{1+\alpha}\right)\right] . \tag{A.9}$$

Summing up, α should be as large as possible in order to guarantee certain margins to the manufacturing and managing processes, i.e., a value $C_1(\alpha, N) \gg 1$ is desired. On the other hand, given β, condition (A.8) sets an upper bound to the admissible range of values that can be assigned to the design parameter α, which also depends on N: the larger N, the lower the upper bound. We shall hence require that

$$C_1(\alpha, N) > \mathrm{thr}_1 , \quad C_2(\alpha, N) < \mathrm{thr}_2 , \tag{A.10}$$

where the thresholds $\mathrm{thr}_1 > 1$ and $\mathrm{thr}_2 < 1$ are two design parameters. Intersecting the admissible regions defined by (A.10), with $\beta = 0.5$, we get the areas

delimited by the curves in Fig. A.1. Note that the robustness of the network to design non-idealities increases as thr_1 grows larger than 1 and thr_2 reduces towards 0, thus progressively shrinking the admissible area for the choice of α. Furthermore, given the thresholds thr_1 and thr_2, the borders of the admissible region for α intersect in correspondence of a certain N, denoted by N^*, which represents the maximum number of MMs that can be connected into the bus network. Note that there exists a tradeoff between design robustness and network size: the larger the network size, the less robust it is to manufacturing or operational errors. In other words, increasing the number N^* of MMs that can be connected to the bus requires more and more precision in the manufacturing of the network elements, and extremely accurate control in the droplet generation process.

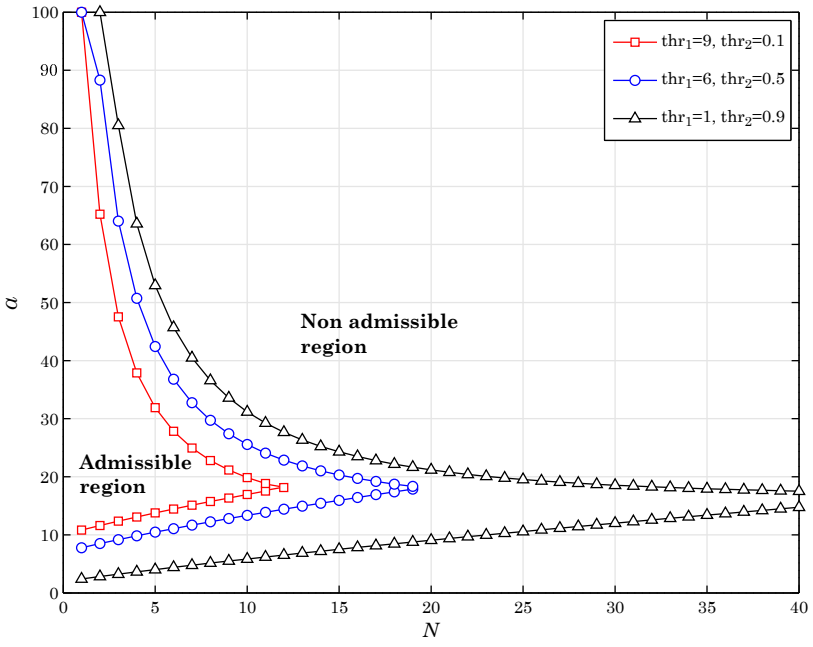

Figure A.1: Admissible range of α imposed by (A.10) as a function of N for various thresholds thr_1, thr_2, and $\beta = 0.5$.

A.2 OpenFOAM

OpenFOAM® (Open Source Field Operation and Manipulation) is a free, open source software package developed by *OpenCFD Ltd* at *ESI Group* and distributed by the *OpenFOAM Foundation*. Basically it works as a *C++* toolbox for the creation of customized numerical solvers, and pre-/post-processing utilities for the solution of continuum mechanics problems, including computational fluid dynamics (CFD).

In the present thesis, we presented a microfluidic study using OpenFOAM to simulate many of the processes described. In particular, the solver to which we have referred is called *interFoam*.

We have used the Volume of Fluid (VoF) method to model the flow of two immiscible fluid (dispersed and continuous phase). In VoF a single set of Navier-Stokes equations for both phases is combined with an advection equation for the fluid fraction α of one of the fluids. In the present work, it is important to underline that both phases are assumed incompressible and Newtonian and the flow is assumed laminar. Hence the general governing equations can be written as:

$$\begin{cases} \nabla U = 0 \\ \frac{\partial \rho U}{\partial t} + \nabla \cdot (\rho U U) = -\nabla p + \nabla \cdot \mu(\nabla U + \nabla U^T) + \rho F + F_S \\ \frac{\partial \alpha}{\partial t} + \nabla \cdot (\alpha U) - \nabla \cdot (\alpha(1-\alpha)U_r) = 0 \end{cases} \tag{A.11}$$

where U is the fluid velocity, p is the pressure, ρ the density, μ the viscosity, F a body force and α the volume fraction, which is one in the the bulk of fluid 1 (dispersed phase), zero in the bulk of fluid 2 (continuous phase), and has an intermediate value in near the interface between the two fluids. F_S, instead, is the surface tension force, modeled as a volumetric force active in the vicinity of the interface only, as described below. The bulk density ρ and viscosity μ in (A.11) are computed as weighted averages of two phase properties, based on the fluid fraction α.

The fluid interface is sharpened by introducing the artificial compression term $\nabla \cdot (\alpha(1-\alpha)U_r)$ in the last formula of (A.11), in which U_r describes the artificial compression velocity. This term acts to counteract interface diffusion and is active only on the fluid interface.

The interfacial tension force is approximated as a body force active in interfacial grid cells only, and is formulated as $F_S = \sigma\kappa(\nabla\alpha)$ where σ is the interfacial tension coefficient and $\kappa = \nabla \cdot (\nabla\alpha/|\nabla\alpha|)$ is the curvature of the interface.

The PIMPLE scheme is applied for pressure-velocity coupling. We used a first order Euler scheme for the transient terms, controlling the time step by setting the Courant maximum number to 0.9. Courant number reflects the portion of a cell that a solute will traverse by advection in one time step and is defined as:

$$Co = \frac{u\Delta t}{\Delta l} \tag{A.12}$$

where Δl is the dimension of the grid cell at each location, u is the average linear velocity at that location and Δt is the maximum time step size. When advection dominates dispersion, designing a model with $Co < 1$ will decrease oscillations, improve accuracy and decrease numerical dispersion. Therefore, we are interested in satisfying this condition.

A first Gauss linear scheme was used for the discretization of the gradient terms. The geometry of the three-dimensional channel used has fixed common parameters. The computational domains and meshes were generated with *blockMesh*, an internal mesh generator of OpenFOAM while the graphical results were viewed using *ParaView* (an open source mutiple-platform application for interactive, scientific visualization).

B

M2M Communications Appendices

B.1 Average number of resources for the case without power control

Using the total probability theorem, we can express $\bar{n}$ as

$$\bar{n} = \epsilon N + (1-\epsilon)\,\mathrm{E}\left[n_{\mathrm{res}}|X_N\right] \tag{B.1}$$

where n_{res} is the number of resources used. Now, the expectation of k conditioned on X_N, i.e. given that the L bits are successfully transmitted within N resources, can be expressed as

$$\begin{aligned}
\mathrm{E}\left[n_{\mathrm{res}}|X_N\right] &= \sum_{h=1}^{N} \Pr\left[n_{\mathrm{res}} \geq h|X_N\right] = \sum_{h=1}^{N} \Pr[Y_{h-1}|X_N] \\
&= \sum_{h=1}^{N} \left(1 - \Pr[X_{h-1}|X_N]\right) = N - \sum_{h=1}^{N} \Pr\left[X_{h-1}|X_N\right] \\
&= N - \sum_{h=1}^{N} \frac{\Pr\left[X_{h-1}, X_{N_k}\right]}{\Pr[X_N]} = N - \sum_{h=1}^{N} \frac{\Pr\left[X_{h-1}\right]}{1-\epsilon}\,.
\end{aligned} \tag{B.2}$$

Using (B.2) in (B.1) we obtain

$$\bar{n} = N - \sum_{h=1}^{N} \Pr[X_{h-1}; N]$$

where we have made explicit that the probability distribution of X_h depends on N through $P^{(tx)^*}$, as follows from (8.21). For $\bar{n}$ to be increasing with N, hence, we must have

$$N - \sum_{h=1}^{N} \Pr\left[X_{h-1}; N\right] \geq N - 1 - \sum_{h=1}^{N-1} \Pr\left[X_{h-1}; N-1\right],$$

which yields

$$\sum_{h=1}^{N-1} \Pr\left[X_{h-1}; N-1\right] + 1 \geq \sum_{h=1}^{N-1} \Pr\left[X_{h-1}; N\right] + \Pr\left[X_{N-1}; N\right].$$

Now, according to (8.19), $P^{(tx)^*}$ is non-increasing with N. Then, the probability of success within h resources (X_h), which is positively correlated with the energy used in each transmission, will be non increasing with N, i.e., $\Pr\left[X_{h-1}; N-1\right] \geq \Pr\left[X_{h-1}; N\right]$ for all $h \geq 1$, which, together with the trivial inequality $1 \geq \Pr\left[X_{N-1}; N\right]$, concludes the proof.

B.2 Optimal solution for the localCSI case

To derive the optimal solution for the localCSI case we model it by means of a constrained Markov Chain. We first define a space $\mathbf{\Omega}$ that includes all possible state vectors with form (ℓ, n), where $n \in \{0, 1, \ldots, N-1\}$ is the number of available slots before transmission ends and $\ell \in \{0, 1, \ldots, L\}$ are the pending bits. Note that the time information is part of the system state variables which makes it a non-stationary Markov Chain as the transition probabilities changes step by step. Accordingly, we have $N \cdot (L+1)$ possible states that the system can assume at each step. The specific value at step k will be indicated with the symbol ω_k. Then, let $p_k(\ell, n) = \Pr\left[\omega_k = (\ell, n)\right]$, $\ell = 0, 1, \ldots, L$, be the probability that exactly ℓ bits are still to be transmitted with n residual slots at the k-th step.

Furthermore, let $P(h; \ell, n)$ be the single-step probability of transmitting $h \leq \ell$ bits out of ℓ when n slots remain before the end of the transmission window, such that $\sum_{h=0}^{\ell} P(h; \ell, n) = 1$ for each state (ℓ, n). Thus, the single-step transition probability from state $\omega_k = (\ell, n)$ to state $\omega_{k+1} = (\ell - h, m)$ is

$$P(h; \ell, n) = \Pr\left[\text{tx } h \text{ bits} \,|\, \omega_k = (\ell, n)\right],$$

where $h \in \{0, 1, \ldots, \ell\}$, and it corresponds to the probability of sending h bits at step k, given that we start with ℓ pending bits and n resources available at the beginning of the slot. Exploiting Markov Chains properties, the probability of

being at state $\omega_k = (\ell, n)$ at step k is given by $p_k(\ell, n) = \left[\mathbf{p_1} \cdot \mathbf{P^{k-1}}\right]_{(\ell,n)}$ where $\mathbf{p_1}$ is the probability vector of the initial state and $\mathbf{P^{k-1}}$ is the $(k-1)$-step transition probability matrix.

For ease of notation we sort the two-dimensional arrays that belong to $\mathbf{\Omega}$ such that they decrease with n. In turn, for a fixed n, we arrange them in decreasing order with respect to ℓ. Accordingly, the ordered set of system states becomes

$$\begin{aligned}\mathbf{\Omega} =&\{(L, N-1); (L-1, N-1); \ldots; (L-h, N-1); \ldots; (0, N-1); (L, N-2); (L-1, N-2);\\ &\ldots; (L-h, N-2); \ldots; (0, N-2); \ldots; (L, 0); (L-1, 0); \ldots; (L-h, 0); \ldots; (0, 0)\}\end{aligned} \tag{B.3}$$

It is important to note that the single-step transition matrix is sparse. Indeed, the only terms that differ from zero are those from state $\omega_1 = (\ell, N-1)$ to state $\omega_2 = (h, N-2)$, with $h = 0, 1, \ldots, \ell$. All remaining values are null because, in a given slot, we cannot send more than the pending bits. More generally, we can deduct the following remarks:

Remark 1: the k-step transition probability matrix $\mathbf{P^k}$ will certainly lead the system from a generic state with time n to a state with time $n+k$. Mathematically, we have that $\left[\mathbf{P^k}\right]_{(\omega_n, \omega_m)} = 0, \forall m \neq n + k$.

Remark 2: if I start from a system state at time n with ℓ pending bits I cannot move to a successive state with a greater number of bits still to be transmitted. Mathematically, it means that $\left[\mathbf{P^k}\right]_{((\ell,n),(\rho,n+k))} = 0, \forall \rho > \ell$.

Remark 3: Putting together Remark 1 and Remark 2, we conclude that

$$\left[\mathbf{P^k}\right]_{((\ell,n),(\rho,m))} = 0, \text{ if } m \neq n + k \vee \rho > \ell.$$

Therefore, although the size of a generic transition matrix $\mathbf{P^k}$ is $(L+1) \cdot N \times (L+1) \cdot N = (L+1)^2 N^2$, it has a maximum of $\frac{(L+1)^2(N-k)}{2}$ values, which are the unknowns in our problem.

Note that, for the particular nature of our problem, the MC step-index and the available slots information are directly related so that we can remove one of them to make the notation less redundant. So, we will simply indicate $p_n(\ell, N-n)$ with $p_n(\ell)$, omitting the parameter $N-n$ which is implicit and $P_n(h; \ell) = P(h; \ell, N-n)$ will indicate the probability of transmitting h out of ℓ bits at the n-th slot.

Now, we assume that at slot 1 we always have L bits to transmit. Thus:

$$p_1(\ell) = \begin{cases} 1, & \text{if } \ell = L \\ 0, & \text{otherwise} \end{cases} \Rightarrow \mathbf{p_1} = (1, 0, \ldots, 0).$$

This rule, together with the law of total probability $\sum_{\ell=0}^{L} p_n(\ell) = 1, \forall n = 1, \ldots, N$ limits the possible values assumed by the state probability vector.

Moreover, we need to impose the outage condition for which the probability of ending the transmission window without sending all the bits must be lower than or equal to ϵ. Mathematically, this constraint can be expressed as follows:

$$\sum_{\ell=1}^{L} p_N(\ell) P_N(\ell;\ell) \geq 1 - \epsilon \tag{B.4}$$

The final aim is to find, step by step, the distribution of the transition probability matrix $\mathbf{P}$ that minimizes the overall energy consumption. To this end, starting from a generic system state $\omega_k = (\ell, n)$ at slot n, we divide the channel gain's domain in $\ell + 1$ adjacent intervals $\{I_n(0;\ell), \ldots, I_n(\ell;\ell)\}$, where $I_n(h;\ell) = [g_n(h;\ell), g_n(h+1;\ell))$, with $g_n(0;\ell) = 0$ and $g_n(\ell+1;\ell) = \infty$. If the channel coefficient experienced in the n-th slot belongs to the interval $I_n(h;\ell)$, the device is instructed to transmit h bits. Accordingly, solving the localCSI problem corresponds to finding the values of such thresholds that minimize the expectation of the overall energy cost. In fact, every transition is associated with a specific energy cost c. Suppose, for example, that we are in slot n with ℓ pending bits and experience a channel gain g, i.e., $\omega_n = (\ell, N-n) \overset{g \in I_n(\rho;\ell)}{\longrightarrow} c_n(\rho;\ell)$. The corresponding energy cost is given by:

$$c_n(\rho;\ell) = \begin{cases} \frac{2^{\frac{\rho}{WT}} - 1}{g} N_0 W T + \mathcal{E}^{(c)}, & \text{if } \rho > 0 \\ 0, & \text{if } \rho = 0 \end{cases}$$

Following this rationale, the expectation of the total energy cost can be evaluated as

$$\begin{aligned} \mathrm{E}\left[\mathcal{E}^{(tot)}\right] &= \mathrm{E}\left[\sum_{n=1}^{N} c(\omega_n, \omega_{n+1})\right] = \sum_{n=1}^{N} \mathrm{E}\left[c(\omega_n, \omega_{n+1})\right] \\ &= \sum_{n=1}^{N} \sum_{\ell=0}^{L} \Pr\left[\omega_n = (\ell, N-n)\right] \mathrm{E}\left[c(\omega_n, \omega_{n+1}) | \omega_n = (\ell, N-n)\right] \\ &= \sum_{n=1}^{N} \sum_{\ell=0}^{L} p_n(\ell) \, \mathrm{E}\left[c(\omega_n, \omega_{n+1}) | \omega_n = (\ell, N-n)\right] \\ &= \sum_{n=1}^{N} \sum_{\ell=0}^{L} p_n(\ell) \sum_{h=0}^{\ell} \Pr\left[g \in I_n(h;\ell) | \omega_n = (\ell, N-n)\right] c_n(h;\ell) \end{aligned} \tag{B.5}$$

B.2.1 Optimal transmission thresholds in the last slot

The derivation of the optimal policy that minimizes (B.5) starts by considering the sub-problem of energy minimization for the last available slot N. We remember that $P_N(h;\ell)$ depends on the channel gain interval $I_N(h;\ell) = [g_N(h;\ell), g_N(h+1;\ell))$ for which the chosen strategy consists in transmitting h bits out of ℓ.

The average cost incurred when transmitting $h > 0$ bits out of ℓ is given by

$$c_N(h;\ell) = \mathcal{E}^{(c)}\left(e^{-\frac{g_N(h;\ell)}{\bar{g}}} - e^{-\frac{g_N(h+1;\ell)}{\bar{g}}}\right) + \int_{g_N(h;\ell)}^{g_N(h+1;\ell)} \frac{e^{-\frac{g}{\bar{g}}}}{\bar{g}} \frac{2^{\frac{h}{WT}} - 1}{g} N_0 WT dg \quad \text{(B.6)}$$

where $\mathcal{E}^{(c)}$ is the circuit energy.

Given the vector $\mathbf{p_N} = \{p_N(0), \ldots, p_N(L)\}$, the problem is to find $\{P_N(h;\ell)\}$, $\forall h = 0, \ldots, \ell$ and $\ell = 0, \ldots, L$ such that the average total energy cost is minimized

$$\min \sum_{\ell=0}^{L} p_N(\ell) \sum_{h=0}^{\ell} P_N(h;\ell) c_N(h;\ell) \quad \text{(B.7)}$$

while satisfying the outage constraint

$$\sum_{\ell=1}^{L} p_N(\ell) P_N(\ell;\ell) \geq 1 - \epsilon \quad \text{(B.8)}$$

Remark 4: if $\ell = 0$, the only possible action is to not transmit any bit, i.e., $P_N(0;0) = 1$.

Remark 5: if $p_N(0) \geq 1 - \epsilon$, (B.8) is always satisfied, and the best strategy is to not transmit any bit, irrespective of the number of pending bits.

Remark 6: if $p_N(0) < 1 - \epsilon$, the best strategy in the last slot is to either transmit all the ℓ pending bits or to do not transmit, i.e., $P_N(\ell;\ell) = 1 - P_N(0;\ell)$.

Based on Remark 3, the unknowns of the sub-problem are the probabilities $P_N(\ell;\ell)$, $\ell = 1, 2, \ldots, L$. In turn, these probabilities are associated to the channel-gain thresholds $g_N(\ell;\ell)$ that, for ease of notation, will be hereafter denoted by x_ℓ by the expression $P_N(\ell;\ell) = e^{-\frac{x_\ell}{\bar{g}}}$.

Summing up, given $\mathbf{p_N}$ and under the assumption that $p_N(0) < 1 - \epsilon$, the solution to the last step sub-problem consists in finding the values of the L unknowns $\{x_\ell\}$ such that the last step average energy cost is minimized

$$\min_{x_1,\ldots,x_L} \sum_{\ell=1}^{L} p_N(\ell) \left[\mathcal{E}^{(c)} e^{-x_\ell/\bar{g}} + \int_{x_\ell}^{\infty} \frac{e^{-g/\bar{g}}}{\bar{g}} \frac{2^{\frac{\ell}{WT}} - 1}{g} N_0 WT dg\right] \quad \text{(B.9)}$$

and the outage condition

$$\sum_{\ell=1}^{L} p_N(\ell)(1 - e^{-x_\ell/\bar{g}}) \leq \epsilon \tag{B.10}$$

is met.

Therefore, we have a problem of constrained minimization of a multivariate non-linear convex function.

Suppose now that we know the distribution $\{p_N(\ell)\}$, $\ell = 0, \ldots, L$. In order to find the optimal x_ℓ we need to solve (B.9) with the constraint in (B.10). This can be done with the Lagrangian Multiplier method. We define the function

$$\mathcal{L} = \sum_{\ell=1}^{L} p_N(\ell) \left[\mathcal{E}^{(c)} e^{-x_\ell/\bar{g}} + \int_{x_\ell}^{\infty} \frac{e^{-g/\bar{g}}}{\bar{g}} \frac{2^{\frac{\ell}{WT}} - 1}{g} N_0 WT dg \right]$$
$$- \lambda \left[\sum_{\ell=1}^{L} p_N(\ell)(1 - e^{-x_\ell/\bar{g}}) - \epsilon \right]$$

We now take the derivative of $\mathcal{L}$ with respect to $x_1, x_2, \ldots, x_L$ and λ obtaining, after some math, the following system of equations

$$\begin{cases} p_N(\ell) e^{-\frac{x_\ell}{\bar{g}}} \left[-\frac{\mathcal{E}^{(c)} + \lambda}{\bar{g}} + \frac{\left(2^{\frac{\ell}{WT}} - 1\right) N_0 WT}{x_\ell} \right] = 0, \ 1 \leq \ell \leq L \\ \sum_{\ell=1}^{L} p_N(\ell)(1 - e^{-x_\ell/\bar{g}}) \leq \epsilon \end{cases} \tag{B.11}$$

whose solution gives us the desired thresholds x_ℓ. Indeed, from (2.4) we get

$$\begin{cases} \lambda = cost = \frac{\left(2^{\frac{\ell}{WT}} - 1\right) N_0 WT \bar{g}}{x_\ell} - \mathcal{E}^{(c)}, \ 1 \leq \ell \leq L \\ \sum_{\ell=1}^{L} p_N(\ell)(1 - e^{-x_\ell/\bar{g}}) \leq \epsilon \end{cases} \tag{B.12}$$

and, consequently,

$$\begin{cases} x_i = x_j \frac{2^{\frac{i}{WT}} - 1}{2^{\frac{j}{WT}} - 1} \\ \sum_{\ell=1}^{L} p_N(\ell)(1 - e^{-x_\ell/\bar{g}}) \leq \epsilon \end{cases} \tag{B.13}$$

The first equation in (B.13) shows the relationship between the different thresholds x_ℓ, $\ell = 1, \ldots, L$, which are increasing with ℓ. This means that, as expected, we have to assign a greater outage budget when we are arriving at the last slot with a greater number of pending bits. Interestingly, we note that this formula does not depend on the probabilities $p_N(\ell)$ which, instead, comes into play in the outage constraint. The solution of the above Lagrangian problem returns the

optimal thresholds $x_\ell(\mathbf{p_N})$ at the last slot and the corresponding expected energy cost $\mathrm{E}\left[c_N(\mathbf{p_N})\right] = \bar{c}_N(\mathbf{p_N})$ for any distribution $\mathbf{p_N}$.

This function can be used to determine the optimal strategy at the previous steps in a backwards induction fashion, as explained in the following.

B.2.2 Optimal transmission thresholds in the second-to-last slot

Let us focus now on the second-to-last slot $N-1$. Suppose that we know the distribution $\mathbf{p_{N-1}} = \{p_{N-1}(0), \ldots, p_{N-1}(L)\}$. Accordingly, the problem is to find $\left\{P_{N-1}(h;\ell) = e^{-\frac{g_{N-1}(h;\ell)}{\bar{g}}} - e^{-\frac{g_{N-1}(h+1;\ell)}{\bar{g}}}\right\}$, $\forall h = 0, \ldots, \ell$ and $\ell = 0, \ldots, L$ such that the two-step average energy cost $\mathrm{E}\left[c_{N-1\to N}(\mathbf{p_{N-1}})\right] = \bar{c}_{N-1\to N}(\mathbf{p_{N-1}})$ is minimized

$$\min_{g_{N-1}(h;\ell)} \sum_{\ell=0}^{L} p_{N-1}(\ell) \sum_{h=0}^{\ell} \left[\bar{c}_{N-1}(h;\ell) + P_{N-1}(h;\ell)\bar{c}_N(p_N(\ell-h))\right] \tag{B.14}$$

where

$$\bar{c}_{N-1}(h;\ell) = \mathcal{E}^{(c)}\left(e^{-\frac{g_{N-1}(h;\ell)}{\bar{g}}} - e^{-\frac{g_{N-1}(h+1;\ell)}{\bar{g}}}\right) + \int_{g_{N-1}(h;\ell)}^{g_{N-1}(h+1;\ell)} \frac{e^{-\frac{g}{\bar{g}}}}{\bar{g}} \frac{2^{\frac{h}{WT}} - 1}{g} N_0 W T dg \tag{B.15}$$

while satisfying the outage constraint

$$\sum_{\ell=1}^{L} p_{N-1}(\ell) \sum_{h=0}^{\ell-1} P_{N-1}(h;\ell)(1 - P_N(\ell-h;\ell-h)) \leq \epsilon \tag{B.16}$$

Rewriting $P_N(\ell-h;\ell-h) = e^{-\frac{x_\ell(p_N(\ell-h))}{\bar{g}}}$, where we explicit its dependence on $p_N(\ell-h)$, and noting that

$$p_N(k) = \sum_{\ell=1}^{L} p_{N-1}(\ell) P_{N-1}(\ell-k;\ell) \tag{B.17}$$

we can translate (B.14) and the constraint (B.16) in the following Lagrangian function

$$\mathcal{L} = \sum_{\ell=1}^{L} p_{N-1}(\ell) \sum_{h=0}^{\ell} \left[\bar{c}_{N-1}(h;\ell) + \left(e^{-\frac{g_{N-1}(h;\ell)}{\bar{g}}} - e^{-\frac{g_{N-1}(h+1;\ell)}{\bar{g}}}\right) \bar{c}_N(p_N(\ell-h))\right]$$
$$- \lambda \left[\sum_{\ell=1}^{L} p_{N-1}(\ell) \sum_{h=0}^{\ell-1} \left(e^{-\frac{g_{N-1}(h;\ell)}{\bar{g}}} - e^{-\frac{g_{N-1}(h+1;\ell)}{\bar{g}}}\right)\left(1 - e^{-\frac{x_\ell(p_N(\ell-h))}{\bar{g}}}\right) - \epsilon\right]$$

Taking the derivative of $\mathcal{L}$ with respect to $g_{N-1}(h;\ell),\ \forall \ell = 0,\dots,L;\ h = 0,\dots,\ell$ and λ we obtain the system of equations[1] that, once solved, leads to the optimal thresholds $g_{N-1}(h;\ell)$ and the corresponding expected two-step energy cost $\mathrm{E}\left[c_{N-1\to N}(\mathbf{p_{N-1}})\right] = \bar{c}_{N-1\to N}(\mathbf{p_{N-1}})$ for any distribution of $\mathbf{p_{N-1}}$.

Finally, similarly to the second-to-last step optimization procedure that we have just done, these results can be exploited to compute the optimal thresholds at the $N-2$th step $g_{N-1}(h;\ell),\ \forall \ell = 0,\dots,L;\ h = 0,\dots,\ell$ and find the corresponding expected two-step energy cost $\mathrm{E}\left[c_{N-2\to N}(\mathbf{p_{N-2}})\right] = \bar{c}_{N-2\to N}(\mathbf{p_{N-2}})$ for any distribution of $\mathbf{p_{N-2}}$ and so on until slot 1 for which we have $\mathbf{p_1} = (1,0,\dots,0)$ as per (B.3).

[1]Note that, since $\bar{c}_N(p_N(\ell-h))$ and $x_\ell(p_N(\ell-h))$ depend on $g_{N-1}(h;\ell)$ through (B.17) we need to apply a fixed point analysis to solve the linear system.

Bibliography

[1] **A. Biral** and A. Zanella, "Introducing purely hydrodynamic networking mechanisms in microfluidic systems," in *IEEE International Workshop on Molecular and Nanoscale Communication (ICC MoNaCom)*, June 2013, pp. 798–803.

[2] ——, "Introducing purely hydrodynamic networking functionalities into microfluidic systems," *Nano Communication Networks*, vol. 4, no. 4, pp. 205–215, 2013.

[3] A. Zanella and **A. Biral**, "Design and analysis of a microfluidic bus network with bypass channels," in *IEEE International Conference on Communications (ICC)*, June 2014, pp. 3993–3998.

[4] **A. Biral**, D. Zordan, and A. Zanella, "Modeling, simulation and experimentation of droplet-based microfluidic networks," *IEEE Transactions on Molecular, Biological and Multi-Scale Communications*, vol. 1, no. 2, pp. 122–134, June 2015.

[5] ——, "Simulating "Macroscopic" Behavior of Droplet-Based Microfluidic Systems," in *IEEE Global Communications Conference (Globecom) 2015*, December 2015, pp. 1–7.

[6] ——, "Transmitting information with microfluidic systems," in *IEEE International Conference on Communications (ICC)*, June 2015, pp. 1103–1108.

[7] **A. Biral**, M. Centenaro, A. Zanella, L. Vangelista, and M. Zorzi, "The challenges of M2M massive access in wireless cellular networks," *Digital Communications and Networks*, vol. 1, no. 1, pp. 1–19, 2015.

[8] **A. Biral**, H. Huang, A. Zanella, and M. Zorzi, "Uplink resource allocation in cellular systems: An energy-efficiency perspective," in *IEEE Global Communications Conference (Globecom) 2015*, December 2015, pp. 1–7.

[9] ——, "On the Impact of Transmitter Channel Knowledge in Energy-Efficient Machine-Type Communication," in *IEEE Globecom Workshop on Energy Efficiency in the IoT*, December 2016.

[10] A. Zanella, **A. Biral**, and M. Zorzi, "Asymptotic Throughput Analysis of Massive M2M Access," in *Information Theory and Applications Workshop (ITA) 2015*, February 2015, pp. 64–69.

[11] S. Y. Teh, R. Lin, L. H. Hung, and P. L. Abraham, "Droplet microfluidics," *Lab Chip*, vol. 8, no. 2, pp. 198–220, 2008.

[12] P. Tabeling, *Introduction to Microfluidics*. Oxford University Press, 2005.

[13] H. B. Thu and T. C. Duc, "Microfluidic injector simulation with saw sensor for 3d integration," in *IEEE Sensors Applications Symposium (SAS) 2014*, February 2014, pp. 213–218.

[14] L. K. Chin, A. Q. Liu, J. B. Zhang, C. S. Lim, and Y. C. Soh, "An on-chip liquid tunable grating using multiphase droplet microfluidics," *Applied Physics Letters*, vol. 93, no. 16, 2008.

[15] P. S. Dittrich and A. Manz, "Lab-on-a-chip: microfluidics in drug discovery," *Nature Reviews Drug Discovery*, vol. 5, pp. 210–218, March 2006.

[16] A. Huebner, S. Sharma, M. Srisa-Art, F. Hollfelder, J. B. Edel, and A. J. Demello, "Microdroplets: a sea of applications?" *Lab on a Chip*, vol. 8, pp. 1244–1254, August 2008.

[17] V. Ananthanarayanan and W. Thies, "Towards a high-level programming language for standardizing and automating biology protocols," in *1st International Workshop on Biodesign Automation*, 2009.

[18] C. G. Yang, Z. R. Xu, and J. H. Wang, "Manipulation of droplets in microfluidic systems," *Trends in Analytical Chemistry*, vol. 29, no. 2, pp. 141–157, 2010.

[19] H. Wu, T. W. Odom, D. T. Chiu, and G. M. Whitesides, "Fabrication of complex three-dimensional microchannel systems in pdms," *Journal of the American Chemical Society*, vol. 125, no. 2, pp. 554–559, 2003.

[20] P. Abgrall and A. Gue, "Lab-on-chip technologies: making a microfluidic network and coupling it into a complete microsystem – a review," *Journal of Micromechanics and Microengineering*, vol. 17, no. 5, p. R15, April 2007.

[21] ThinXXS Microtechnology, Date Accessed: 15 November 2016. [Online]. Available: http://www.thinxxs.com/main/thinxxs/mailing-california.html

[22] D. R. Link, E. Grasland-Mongrain, A. Duri, F. Sarrazin, Z. Cheng, G. Cristobal, M. Marquez, and D. A. Weitz, "Electric control of droplets in microfluidic devices," *Angewandte Chemie Int. Ed.*, vol. 45, no. 16, pp. 2556–2560, 2006.

[23] P. H. Yuh, C. L. Yang, and Y. W. Chang, "Bioroute: A network-flow-based routing algorithm for the synthesis of digital microfluidic biochips," *IEEE Transactions on Computer-Aided Design of Integrated Circuits and Systems*, vol. 27, no. 11, pp. 1928–1941, November 2008.

[24] A. Wixforth, "Acoustically driven planar microfluidics," *Superlattices and Microstructures*, vol. 33, no. 5-6, pp. 389–396, 2003.

[25] D. Mark, S. Haeberle, G. Roth, F. von Stetten, and R. Zengerle, "Microfluidic lab-on-a-chip platforms: requirements, characteristics and applications," *Chem. Soc. Rev.*, vol. 39, pp. 1153–1182, 2010.

[26] C. N. Baroud, F. Gallaire, and R. Dangla, "Dynamics of microfluidic droplets," *Lab Chip*, vol. 10, pp. 2032–2045, 2010.

[27] T. Thorsen, R. Roberts, F. H. Arnold, and S. R. Quake, "Dynamic pattern formation in a vesicle-generating microfluidic device," *Physical Review Letters*, vol. 86, no. 18, pp. 4163–4166, April 2001.

[28] P. Garstecki, M. J. Fuerstman, H. A. Stone, and G. M. Whitesides, "Formation of droplets and bubbles in a microfluidic T-junction-scaling and mechanism of break-up," *Lab Chip*, vol. 6, pp. 437–446, 2006.

[29] M. de Menech, P. Garstecki, F. Jousse, and H. A. Stone, "Transition from squeezing to dripping in a microfluidic T-shaped junction," *Journal of Fluid Mechanics*, vol. 595, pp. 141–161, 2008.

[30] A. Gupta and R. Kumar, "Flow regime transition at high capillary numbers in a microfluidic T-junction: Viscosity contrast and geometry effect," *Physics of Fluids*, vol. 22, no. 12, 2010.

[31] M. J. Fuerstman, P. Garstecki, and G. M. Whitesides, "Coding/Decoding and Reversibility of Droplet Trains in Microfluidic Networks," *Science*, vol. 315, no. 5813, pp. 828–832, 2007.

[32] M. J. Fuerstman, A. Lai, M. E. Thurlow, S. S. Shevkoplyas, H. A. Stone, and G. M. Whitesides, "The pressure drop along rectangular microchannels containing bubbles," *Lab Chip*, vol. 7, pp. 1479–1489, 2007.

[33] A. A. Carlson, M. Do-Quang, and G. Amberg, "Droplet dynamics in a bifurcating channel," *International Journal of Multiphase Flow*, vol. 36, no. 5, pp. 397–405, 2010.

[34] D. R. Link, S. L. Anna, D. A. Weitz, and H. A. Stone, "Geometrically mediated breakup of drops in microfluidic devices," *Physical Review Letters*, vol. 92, p. 054503, February 2004.

[35] A. M. Leshansky and L. M. Pismen, "Breakup of drops in a microfluidic T junction," *Physics of Fluids*, vol. 21, no. 2, p. 023303, 2009.

[36] W. O. Kwang, K. Lee, B. Ahn, and E. P. Furlani, "Design of pressure-driven microfluidic networks using electric circuit analogy," *Lab Chip*, vol. 12, pp. 515–545, 2012.

[37] A. Ajdari, "Steady flows in networks of microfluidic channels: building on the analogy with electrical circuits," *Comptes Rendus Physique*, vol. 5, no. 5, pp. 539–546, 2004.

[38] G. F. Christopher, J. Bergstein, N. B. End, M. Poon, C. Nguyen, and S. L. Anna, "Coalescence and splitting of confined droplets at microfluidic junctions," *Lab on a Chip*, vol. 9, no. 8, pp. 1102–1109, 2009.

[39] M. C. Jullien, M. J. Tsang Mui Ching, C. Cohen, L. Menetrier, and P. Tabeling, "Droplet breakup in microfluidic T-junctions at small capillary numbers," *Physics of Fluids*, vol. 21, no. 7, p. 072001, 2009.

[40] D. A. Sessoms, M. Belloul, W. Engl, M. Roche, L. Courbin, and P. Panizza, "Droplet motion in microfluidic networks: Hydrodynamic interactions and pressure-drop measurements," *Physical Review E*, vol. 80, p. 016317, July 2009.

[41] E. De Leo, L. Galluccio, A. Lombardo, and G. Morabito, "On the feasibility of using microfluidic technologies for communications in Labs-on-a-Chip," in *IEEE International Conference on Communications (ICC)*, June 2012, pp. 2526–2530.

[42] G. Cristobal, J.-P. Benoit, M. Joanicot, and A. Ajdari, "Microfluidic bypass for efficient passive regulation of droplet traffic at a junction," *Applied Physics Letters*, vol. 89, no. 3, p. 034104, 2006.

[43] M. Prakash and N. Gershenfeld, "Microfluidic Bubble Logic," *Science*, vol. 315, no. 5813, pp. 832–835, 2007.

[44] L. Donvito, L. Galluccio, A. Lombardo, and G. Morabito, "Microfluidic networks: Design and simulation of pure hydrodynamic switching and medium access control," *Nano Communication Networks*, vol. 4, no. 4, pp. 164–171, 2013.

[45] E. De Leo, L. Galluccio, A. Lombardo, and G. Morabito, "Networked Labs-on-a-Chip (NLoC): Introducing networking technologies in microfluidic systems," *Nano Communication Networks*, vol. 3, no. 4, pp. 217–228, 2012.

[46] A. Zanella, N. Bui, A. Castellani, L. Vangelista, and M. Zorzi, "Internet of Things for Smart Cities," *IEEE Internet of Things Journal*, vol. 1, no. 1, pp. 22–32, February 2014.

[47] L. Atzori, A. Iera, and G. Morabito, "The Internet of Things: A survey," *Computer Networks*, vol. 54, no. 15, pp. 2787–2805, October 2010.

[48] P. Bellavista, G. Cardone, A. Corradi, and L. Foschini, "Convergence of MANET and WSN in IoT urban scenarios," *IEEE Sensors Journal*, vol. 13, no. 10, pp. 3558–3567, October 2013.

[49] J. Zheng and M. J. Lee, "A comprehensive performance study of IEEE 802.15.4," in *Sensor Network Operations*. IEEE Press Book, Wiley Interscience, 2006, ch. 4, pp. 218–237.

[50] G. Montenegro, N. Kushalnagar, J. Hui, and D. Culler, "Transmission of IPv6 packets over IEEE 802.15.4 networks," Tech. Rep. IETF Request for Comments 4944, September 2007. [Online]. Available: http://tools.ietf.org/pdf/rfc4944.pdf

[51] P. Kinney *et al.*, "Zigbee technology: Wireless control that simply works," in *Communications design conference*, October 2003.

[52] H. Merz, J. Backer, V. Moser, T. Hansemann, L. Greefe, and C. Hübner, *Building Automation: Communication Systems with EIB/KNX, LON and BACnet*. Springer, June 2009.

[53] 3GPP, "Feasibility study for Proximity Services (ProSe)," Tech. Rep. TR 22.803 V12.2.0, June 2013.

[54] H. Schaffers, N. Komninos, M. Pallot, B. Trousse, M. Nilsson, and A. Oliveira, "Smart Cities and the Future Internet: Towards Cooperation Frameworks for Open Innovation," in *The Future Internet*. Springer, 2011, vol. 6656, pp. 431–446.

[55] A. Laya, L. Alonso, and J. Alonso-Zarate, "Is the Random Access Channel of LTE and LTE-A Suitable for M2M Communications? A Survey of Alternatives," *IEEE Communications Surveys Tutorials*, vol. 16, no. 1, pp. 4–16, January 2014.

[56] 3GPP, "Study on RAN Improvements for Machine-type Communications," Tech. Rep. TR 37.868 V11.0.0, September 2011.

[57] A. Lo, Y. Law, M. Jacobsson, and M. Kucharzak, "Enhanced LTE-Advanced Random-Access Mechanism for Massive Machine-to-Machine (M2M) Communications." 27th World Wireless Research Forum Meeting, October 2011.

[58] K. S. Ko, M. J. Kim, K. Y. Bae, D. K. Sung, J. H. Kim, and J. Y. Ahn, "A Novel Random Access for Fixed-Location Machine-to-Machine Communications in OFDMA Based Systems," *IEEE Communications Letters*, vol. 16, no. 9, pp. 1428–1431, September 2012.

[59] T. Taleb and A. Kunz, "Machine type communications in 3GPP networks: potential, challenges, and solutions," *IEEE Communications Magazine*, vol. 50, no. 3, pp. 178–184, March 2012.

[60] L. M. Bello, P. Mitchell, and D. Grace, "Application of Q-Learning for RACH Access to Support M2M Traffic over a Cellular Network," in *European Wireless Conference*, May 2014, pp. 1–6.

[61] Y.-C. Pang, S.-L. Chao, G.-Y. Lin, and H.-Y. Wei, "Network access for M2M/H2H hybrid systems: a game theoretic approach," *IEEE Communications Letters*, vol. 18, no. 5, pp. 845–848, June 2014.

[62] C.-Y. Tu, C.-Y. Ho, and C.-Y. Huang, "Energy-Efficient Algorithms and Evaluations for Massive Access Management in Cellular Based Machine to Machine Communications," in *IEEE Vehicular Technology Conference (VTC Fall) 2011*, September 2011, pp. 1–5.

[63] C. Y. Ho and C.-Y. Huang, "Energy-Saving Massive Access Control and Resource Allocation Schemes for M2M Communications in OFDMA Cellular Networks," *IEEE Wireless Communications Letters*, vol. 1, no. 3, pp. 209–212, June 2012.

[64] S.-Y. Lien, K.-C. Chen, and Y. Lin, "Toward ubiquitous massive accesses in 3GPP machine-to-machine communications," *IEEE Communications Magazine*, vol. 49, no. 4, pp. 66–74, April 2011.

[65] S.-Y. Lien and K.-C. Chen, "Massive Access Management for QoS Guarantees in 3GPP Machine-to-Machine Communications," *IEEE Communications Letters*, vol. 15, no. 3, pp. 311–313, March 2011.

[66] P. Si, J. Yang, S. Chen, and H. Xi, "Adaptive Massive Access Management for QoS Guarantees in M2M Communications," *IEEE Transactions on Vehicular Technology*, pp. 3152–3166, July 2015.

[67] S. Zhenqi, Y. Haifeng, C. Xuefen, and L. Hongxia, "Research on uplink scheduling algorithm of massive M2M and H2H services in LTE," in *IET International Conference on Information and Communications Technologies (IETICT)*, April 2013, pp. 365–369.

[68] S. Bayat, Y. Li, Z. Han, M. Dohler, and B. Vucetic, "Distributed massive wireless access for cellular machine-to-machine communication," in *IEEE International Conference on Communications (ICC) 2014*, June 2014, pp. 2767–2772.

[69] M. Hasan, E. Hossain, and D. Niyato, "Random access for machine-to-machine communication in LTE-advanced networks: issues and approaches," *IEEE Communications Magazine*, vol. 51, no. 6, pp. 86–93, June 2013.

[70] Y. Qi, A. Ijaz, A. Quddus, M. Imran, P. Navaratnam, Y. Ma, R. Tafazolli, M. Webb, and Y. Morioka, "On the Physical Layer Design for Low Cost Machine Type Communication in 3GPP LTE," in *IEEE Vehicular Technology Conference (VTC Fall)*, September 2014, pp. 1–5.

[71] 3GPP, "LTE coverage enhancements," Tech. Rep. TR 36.824 V11.0.0, June 2012.

[72] General Dynamics Broadband UK, "Coverage extension for MTC UEs," Tech. Rep. TSG RAN1#71 R1-125204, November 2012.

[73] Y. Chan, J. Yang, and P. Zong, "Machine-to-machine communications over fixed wireless networks," April 2013, US Patent 8,416,741. [Online]. Available: http://www.google.com/patents/US8416741

[74] G. Cocco, C. Ibars, and N. Alagha, "Cooperative coverage extension in heterogeneous machine-to-machine networks," in *IEEE Globecom Workshops*, December 2012, pp. 1693–1699.

[75] C. Stefanovic and P. Popovski, "ALOHA Random Access that Operates as a Rateless Code," *IEEE Transactions on Communications*, vol. 61, no. 11, pp. 4653–4662, November 2013.

[76] C. Stefanovic, M. Momoda, and P. Popovski, "Exploiting capture effect in frameless ALOHA for massive wireless random access," in *IEEE Wireless Communications and Networking Conference (WCNC)*, April 2014, pp. 1762–1767.

[77] A. Zanella, M. Zorzi, A. dos Santos, P. Popovski, N. Pratas, C. Stefanovic, A. Dekorsy, C. Bockelmann, B. Busropan, and T. Norp, "M2M massive wireless access: Challenges, research issues, and ways forward," in *IEEE Globecom Workshops*, December 2013, pp. 151–156.

[78] F. Boccardi, R. Heath, A. Lozano, T. Marzetta, and P. Popovski, "Five disruptive technology directions for 5G," *IEEE Communications Magazine*, vol. 52, no. 2, pp. 74–80, February 2014.

[79] R. Min and A. Chandrakasan, "Top Five Myths about the Energy Consumption of Wireless Communication," *ACM Sigmobile Mobile Communication and Communications Review*, vol. 6, pp. 65–67, 2002.

[80] H. S. Dhillon, H. C. Huang, H. Viswanathan, and R. A. Valenzuela, "Power-Efficient System Design for Cellular-Based Machine-to-Machine Communications," *IEEE Transactions on Wireless Communications*, vol. 12, no. 11, pp. 5740–5753, November 2013.

[81] A. Marques, X. Wang, and G. Giannakis, "Optimizing Energy Efficiency of TDMA with Finite Rate Feedback," in *IEEE International Conference on Acoustics, Speech and Signal Processing, 2007*, vol. 3, April 2007, pp. III–117–III–120.

[82] X. Zhang, L. L. Xie, and X. Shen, "An Energy-Efficient Bit Allocation Scheme in Wireless Sensor Networks," in *IEEE Global Communications Conference (Globecom) 2010*, December 2010, pp. 1–5.

[83] A. El Gamal, C. Nair, B. Prabhakar, E. Uysal-Biyikoglu, and S. Zahedi, "Energy-efficient scheduling of packet transmissions over wireless networks," in *IEEE INFOCOM 2002*, vol. 3, June 2002, pp. 1773–1782.

[84] W. Yu and J. M. Cioffi, "On constant power water-filling," in *IEEE International Conference on Communications (ICC) 2001*, vol. 6, 2001, pp. 1665–1669.

[85] D. Bertsekas, *Dynamic Programming and Optimal Control*. 3rd ed. Athena Scientific, 2007.

[86] D. Tse and P. Viswanath, *Fundamentals of Wireless Communication*. Cambridge University Press, 2005.

[87] S. Ahmed, L.-L. Yang, and L. Hanzo, "Probability Distributions of Products of Rayleigh and Nakagami-m Variables Using Mellin Transform," in *IEEE International Conference on Communications (ICC) 2011*, June 2011.

[88] Q. Wang, M. Hempstead, and W. Yang, "A Realistic Power Consumption Model for Wireless Sensor Network Devices," in *IEEE Communications Society on Sensor and Ad Hoc Communications and Networks (SECON) 2006*, vol. 1, September 2006, pp. 286–295.

[89] J. J. Garcia-Luna-Aceves, H. R. Sadjadpour, and Z. Wang, "Challenges: Towards Truly Scalable Ad Hoc Networks," in *MobiCom '07: Proceedings of the 13th annual ACM international conference on Mobile Computing and networking*, 2007, pp. 207–214.

[90] A. Zanella and M. Zorzi, "Theoretical Analysis of the Capture Probability in Wireless Systems with Multiple Packet Reception Capabilities," *IEEE Transactions on Communications*, vol. 60, no. 4, pp. 1058–1071, April 2012.

[91] S. Ghez, S. Verdu, and S. Schwartz, "Stability properties of slotted Aloha with multipacket reception capability," *IEEE Transactions on Automatic Control*, vol. 33, no. 7, pp. 640–649, July 1988.

[92] P. Minero and M. Franceschetti, "Throughput of Slotted ALOHA with Encoding Rate Optimization and Multipacket Reception," in *INFOCOM'09*, 2009, pp. 2971–2975.

[93] L. G. Roberts, "ALOHA Packet System With and Without Slots and Capture," *Communications Reviews*, pp. 28–42, April 1975.

[94] M. Zorzi and R. Rao, "Capture and retransmission control in mobile radio," *IEEE Journal on Selected Areas in Communications*, vol. 12, no. 8, pp. 1289–1298, October 1994.

[95] V. Naware, G. Mergen, and L. Tong, "Stability and delay of finite-user slotted ALOHA with multipacket reception," *IEEE Transactions on Information Theory*, vol. 51, no. 7, pp. 2636–2656, July 2005.

[96] N. Michelusi, P. Popovski, O. Simeone, M. Levorato, and M. Zorzi, "Cognitive Access Policies under a Primary ARQ Process via Forward-Backward Interference Cancellation," *IEEE Journal on Selected Areas in Communications*, vol. 31, no. 11, pp. 2374–2386, November 2013.

[97] NetWorld2020 ETP, "5G: Challenges, Research Priorities, and Recommendations," Tech. Rep., August 2014.

[98] A. Osseiran, F. Boccardi, V. Braun, K. Kusume, P. Marsch, M. Maternia, O. Queseth, M. Schellmann, H. Schotten, H. Taoka *et al.*, "Scenarios for 5G mobile and wireless communications: the vision of the METIS project," *IEEE Communications Magazine*, vol. 52, no. 5, pp. 26–35, May 2014.